UC Berkeley
UC Berkeley Electronic Theses and Dissertations

Title
Study of EUV Photoresist via Modeling and Novel Metrology

Permalink
https://escholarship.org/uc/item/0zs6619j

Author
Long, Luke Travis

Publication Date
2022

Peer reviewed|Thesis/dissertation

eScholarship.org Powered by the California Digital Library
University of California

Study of EUV Photoresist via Modeling and Novel Metrology

by

Luke Long

A dissertation submitted in partial satisfaction of the

requirements for the degree of

Doctor of Philosophy

in

Physics

in the

Graduate Division

of the

University of California, Berkeley

Committee in charge:

Professor Naomi Ginsberg, Co-chair
Dr. Patrick Naulleau, Co-chair
Professor Andrew Neureuther
Professor Ramamoorthy Ramesh

Fall 2022

Study of EUV Photoresist via Modeling and Novel Metrology

Copyright 2022
by
Luke Long

Abstract

Study of EUV Photoresist via Modeling and Novel Metrology

by

Luke Long

Doctor of Philosophy in Physics

University of California, Berkeley

Professor Naomi Ginsberg, Co-chair

Dr. Patrick Naulleau, Co-chair

After decades of research, extreme ultraviolet lithography (EUVL) is being used in high volume manufacturing of semiconductor chips. However, extension of EUVL beyond the current manufacturing nodes requires advancement in nearly every step of the lithographic process, from the source used to generate EUV photons, to the etch used to create a physical structure on the silicon wafer. This thesis focuses on understanding the major bottleneck to further scaling of EUVL, the photoresist material responsible for capturing the light. These incredible materials capture incoming ionizing radiation, use the resulting photoelectrons to excite target chemical processes, drive that chemistry to induce a differential solubility between exposed and unexposed material, and ultimately are developed to leave behind the desired pattern on the wafer for further processing. The interplay between all of these processes needs to be nearly perfect for the process to achieve acceptable yield for high volume manufacturing, let alone for achieving the desired performance of the integrated circuit product. However, many intrinsic, random processes, including photon absorption, photoelectron generation and propagation, and the chemical distribution of the photoresist material itself, conspire to degrade the fidelity between the design and realization of the pattern on the wafer. In this thesis, these effects are studied through a combination of stochastic modeling and experimental techniques, with the goal of providing insight into the workings of photoresist materials and to shine light on how they may be improved for future lithographic nodes.

After an introductory first chapter, the second chapter is focused on the results of a stochastic resist model used to study in the influence of various resist parameters on material performance. A key metric used in the semiconductor industry to quantify resist quality is the roughness at the line edge of line/space patterns. Known as line edge roughness (LER) for a single edge or line width roughness (LWR) for roughness in width, this parameter must be

kept to a minimum, both to enable accurate overlay of subsequent lithographic layers, and for device performance purposes. To study the impact of chemical additives to the host photoresist polymer on the resulting roughness of resist materials, the stochastic Multivariate Poisson Propagation Model (MPPM) was used, in which the initial distribution of photons and additives are treated as a random, Poisson variables and propagated through the exposure and bake steps to produce the final lithographic structure. The modeling study showed the critical tradeoff between chemical noise and chemical image slope that results from the exposure and subsequent post-exposure bake (PEB) in the workhorse material of the industry, chemically amplified resist (CAR). CAR materials are comprised of a host polymer and photoacitve additives. The modeling study showed that by changing the photoactivity of the additives, one can improve LWR by improving the chemical gradient that separates exposed and unexposed regions of resist, at the cost of additional noise coming form the photon and chemical shot noise in the material. This fundamental tradeoff underpins current resist development efforts, with some resist suppliers moving to single-component photoresist materials to minimize chemical shot noise contributions, while other seeking to increase the nonlinearity in CAR-like materials to improve the exposure-induced chemical gradient.

A second modeling study expanded the 2D resist model to a full 3D model, with a focus on another stochastic failure modality, closed contact holes. This study showed that small "roadblocks" of material with too little dose or the wrong combination of photoactive compounds can lead to a failure of the contact to develop. This process is sensitive to the precise nature of the development process; in particular, developer that is able to remove small road blocks has the ability to lower missing contact rates, at the cost of shifting the contact to a larger size at equivalent dose. Furthermore, the study was used to examine the possible benefits of specialized materials or processing that alter the diffusion of photoactive compounds during the post-exposure bake. In particular, the model verified what had been predicted previously by simplified algebraic models; increasing diffusion perpendicular to the wafer leads to a lower rate of closed contacts without the negative impact on the chemical slope.

The next two chapters focus on experimental means to measure input parameters to the MPPM. The first technique explored was atomic force microscopy (AFM), a technique in which a sharp probe is scanned across a sample, producing, among a few different possibilities, a height map of the sample surface. This technique was applied to measure the latent chemistry present in photoresist exposed to radiation but not yet developed. The exposure and bake process in resist materials often leads to outgassing of the chemically altered material, leaving behind a topgraphic structure. The experiment showed that roughness measured in the post-develop structure via scanning electron microscopy is present also at the latent stage, and that the line width and LWR prior to dissolution can be characterized via AFM. Furthermore, the results suggested that the topographic transition from the exposed to the unexposed regions of the latent image seemed to agree with an increase in chemical slope predicted by modeling.

AFM was also used to perform high-speed, in-situ measurements of the dissolution process.

This was achieved using a specially designed flow cell to control the injection of the developer, a critical component of the experiment, as the development occurs on a sub-second time scale. These experiments were able to show that the exposed regions of resist swell prior to removal, a result seen previously with diluted developer, but not thought to occur when in the full-strength process. Additionally the results show that the development process itself serves as a sort of low-pass filter on the roughness; the material removed most quickly leaves behind a number of bumps on the line edge that are removed by further exposure to developer. Finally, using spiral scan trajectories instead of traditional raster scans, the technique was able to image capture a 250 µm by 250 µm image at a 10 Hz frame rate, enabling measurement of the dissolution dynamics of the resist material. Together, these results provide new insight into the development process that will inform future dissolution modeling efforts as well as guide dissolution process improvements.

The final chapter is devoted to resist characterization using resonant soft X-ray scattering (RSoXS), a technique that combines near edge fine structure spectroscopy with X-ray scattering. This technique shows promise for measuring both the chemical noise within the photoresist and the measurement of latent images in the material. This thesis discusses the work performed to date using RSoXS. In measuring polymer-based samples that are either exposed, or exposed to a uniform radiation pattern, RSoXS showed subtle differences in scattering signature near the carbon edge as a function of exposure and incident X-ray energy, suggesting sensitivity to the acid-driven deprotection reaction in the film. On the same set of samples, RSoXS was unable to measure aggregation of photoacid generator molecules, suggesting that any aggregation that may occur does so on a length scale smaller than the 10 nm resolution of the experiments that were conducted. In a different, metal-oxide based material, scattering experiments near the tin L edge revealed cluster size changes as a function of exposure and metrology wavelength, which suggest clusters approximately 1 nm in size on average in the unexposed film, with a broadening in the distribution upon exposure. These early results highlight the potential utility for RSoXS to measure chemical homogeneity in resist films, a critical characteristic for materials that must pattern reliably in the sub-10 nm regime.

RSoXS was also explored for profilometry of the latent exposure pattern in the material. A combination of experimental results and rigorous electromagnetic simulation highlight the challenges that must be overcome in interpreting the collected data. Notably, proper fitting of the underlying latent structure must separate the scattering signal into contributions from exposure-induced shrinkage, chemical modification of the underlying film, and thin-film interference effects, particularly for conducting experiments in a grazing-incidence configuration. This picture is further complicated by modeling and experimental results that suggest that the Born approximation, a commonly used model used to interpret X-ray scattering results, may not sufficiently capture all the physics of the scattering in the X-ray regime, as highlighted by a discrepancy between the Born approximation and rigorous modeling for transmission based samples. Nevertheless, the modeled and experimental results do show

that the technique is sensitive to both physical and chemical structures in latent photoresist; further development my yield a useful technique for latent photoresist metrology.

Together, these studies contribute to the foundational understanding and measurement techniques required to design materials that can pattern trillions of features without error. It is my hope the findings and techniques presented in this thesis will serve as a guide for future researchers as the community works towards extending EUVL, ultimately pushing the limits of technological achievement.

In loving memory of my dad
James A Long
1956-2021

Contents

Contents ii

List of Figures iv

List of Tables viii

1 Introduction 1
- 1.1 Photolithography Basics . . . 1
- 1.2 Extreme Ultraviolet Lithography . . . 3
- 1.3 Photoresist . . . 5
- 1.4 Thesis Structure . . . 8

2 Stochastic Photoresist Modeling 9
- 2.1 Multivariate Poisson Propagation Model . . . 9
- 2.2 Study - Photodecomposable Quencher and the noise-slope tradeoff . . . 13
- 2.3 Results . . . 18
- 2.4 Modeling in 3D . . . 26
- 2.5 Study - Modeling Anisotropic Blur and Missing contacts . . . 27

3 AFM Metrology 41
- 3.1 AFM Basics . . . 41
- 3.2 Study - Influence of PEB time on latent image . . . 44
- 3.3 In-situ dissolution monitoring . . . 54

4 RSoXS Metrology 70
- 4.1 RSoXS Basics . . . 70
- 4.2 Clear Field Samples . . . 75
- 4.3 RSoXS for latent image profilometry . . . 83
- 4.4 Beam Damage . . . 94

5 Conclusion 97
- 5.1 Summary of Results . . . 97
- 5.2 Future Directions . . . 98

Bibliography **99**

List of Figures

1.1 Schematic of the photolithography process. . . . 2
1.2 Herschel telescope 4
1.3 ASML Scanner and Multilayer Mirror-lens 4

2.1 Illustration of shot noise vs dose 10
2.2 Illustration of noise propagation in MPPM 11
2.3 Illustration of PSD propagation in MPPM 12
2.4 PSCAR 2.0 Process. 15
2.5 Quantum efficiency vs photodecomposable quencher loading 16
2.6 Measured LER vs Noise/Slope model. 17
2.7 LWR vs Dose for conventional quencher, photdecomposable quencher, and PSCAR platforms 19
2.8 Total Noise vs. Dose 20
2.9 Breakout of different noise contributions 21
2.10 PSCAR 2.0 Slope vs Dose. 21
2.11 NPDB Acid Profiles. Concentrations normalized by PAG loading. 22
2.12 NPDB Acid and Deprotection Slopes. 22
2.13 PDB Acid Profiles. 23
2.14 PDB Slope vs Dose. 24
2.15 Z factor ($R^3 * (LWR)^2 * S$). 25
2.16 Aerial image comprised of a 15×15 array of 16 nm contacts. Pixels are 0.4 nm per side. 26
2.17 Schematics of the analysis methods. (a) The volume averaging method. Note that volume above and below the blockage is counted. (b) Minimum area method. The blockage sets the CD to zero. 29
2.18 Develop speed vs deprotection corresponding to the Mack model with parameters given in Table 2.3. 30
2.19 Acid PSF and corresponding contact contours. Rows correspond to the x-z plane of the blur function, a side profile, and an aerial view of the resulting contact, respectively. Columns correspond to z blur values of 6, 12, and 24 nm, respectively, with x-y blur held constant at 12. As z blur increases, contact edges become smoother, and the path to from top to bottom becomes clearer. 32

2.20 CD histograms produced by the (a) volume average and (b) z-projected minimum CD methods. . . . 33
2.21 Contour of 6 nm z blur contact after develop. This is directly comparable to the threshold develop method used to generate the profiles in the middle column of Figure 2.19. . . . 34
2.22 Contact CD distribution using the Mack development model. . . . 35
2.23 (a) CD vs dose response and (b) corresponding dose to size for the different z blur resist models. . . . 36
2.24 Contact CD distribution using develop model after adjusting dose such that all contacts print to the same average size. . . . 36
2.25 Comparison of (a) CD distribution and (b) dose response of the isotropic $(12, 12, 12)$nm, anisotropic $(12, 12, 24)$nm, and isotropic $(15, 15, 15)$nm blurs. . . . 37
2.26 Example of the impact of different etch thresholds on the resulting contact shape. The more resist etched, the larger the contact. . . . 37
2.27 Histograms assuming different etch models. (a) Baseline, assuming perfect etch selectivity. (b) Etch 1 nm of resist. (c) Etch 2 nm of resist. (d) Etch 5 nm of resist. 38
2.28 Re-biased CD histograms with 5 nm etch assumption. While the increased z blur resist has a wider CD distribution, it also displays 0 missing contacts, unlike the isotropic (2 missing) and 2 nm (4 missing) z blur simulations. . . . 39
2.29 Profile of a failed contact. (a) Cutline of initial acid distribution. Two unconnected regions of high acid concentration are separated by the blockage-causing region. (b) Resulting post-develop profile. Bottom 8 nm of undeveloped resist is not clear-able by a 5 nm etch. . . . 40

3.1 Schematic of AFM experiment 42
3.2 The amplitude (blue) and phase (red) of the forced-damped harmonic oscillator near resonance. This is a good model of the motion of the AFM cantilever tip. . . 43
3.3 The amplitude (blue) and phase (red) of the forced-damped harmonic oscillator near resonance, both for the free cantilever (solid lines), and for the tip in the presence of a repulsive force (dashed). . . . 43
3.4 Schematic of latent image AFM experiment 46
3.5 AFM scan of unexposed photoresist 47
3.6 Autocovariance of AFM scan of unexposed photoresist. . . . 47
3.7 AFM measurements of latent line/space patterns at different post-exposure bake times. . . . 48
3.8 Histograms of line/space latent image measurements. . . . 49
3.9 Latent image CD vs bake time. . . . 49
3.10 Latent image LWR vs bake time. . . . 50
3.11 Example of LWR PSD measured from the AFM scan. . . . 50
3.12 Latent image line/space profile. . . . 51
3.13 Latent LWR correlation length vs bake time. . . . 51
3.14 Latent image “chemical” slope. . . . 52

3.16 Metal oxide latent image histograms. . . . 54
3.17 Schematic of the flow cell created by the perfusion cantilever holder and the substrate 56
3.18 Previous experiment showing occlusion of the cantilever probe by the mixing of water and TMAH. . . . 57
3.19 Schematic of the newly-designed flow cell for dissolution experiments 58
3.20 Images of the flow cell. . . . 59
3.21 Frequency response of the AFM z-piezo 60
3.22 Image of the current, lower-mass flow cell. . . . 60
3.23 SEM micrographs of high speed AFM probes. . . . 61
3.24 Schematic of the optical disturbance caused by the water-TMAH index of refraction mismatch. . . . 62
3.25 Plot of scan patterns used for AFM experiments. . . . 63
3.26 Early AFM dissolution experiment corresponding to low concentration developer flow condition. . . . 64
3.27 Early AFM dissolution experiment with nearly full strength developer. . . . 64
3.28 First high-speed, full strength developer experiment with stable tip tracking. . . 65
3.29 Dissolution experiment at 3.9 Hz 66
3.30 LER vs dissolution time from 3.9 Hz data. . . . 67
3.31 10 Hz dissolution data capturing using spiral scan geometry. . . . 68

4.1 Schematic of the RSoXS technique, which combines (a) NEXAFS with (b) X-ray scattering. . . . 71
4.2 Schematic of RSoXS experimental configurations 74
4.3 NEXAFS of a commercial resist. . . . 76
4.4 Modeled scattering vs bake time using experimental index of refraction shown in Figure 4.3. . . . 77
4.5 Chemical makeup of model photoresist material. . . . 77
4.6 NEXAFS spectra of model material with varying PAG loading. . . . 78
4.7 Resonant scattering of model material at the carbon K edge. . . . 80
4.8 Fluorine edge NEXAFS spectra of model material with varying PAG loading. . 81
4.9 Resonant scattering of model material at the fluorine K edge. . . . 82
4.10 NEXAFS and resonant scattering of metal-oxide resist at the Sn L edge. . . . 83
4.11 Simulated RSoXS experiment showing the impact of chemical slope on diffracted X-ray distribution. . . . 85
4.12 Simulation of roughness PSD extraction from scattered X-rays. . . . 85
4.13 Example of experimental grazing incidence CD-RSoXS data, as it appears on the CCD. . . . 86
4.14 Scattered intensity at 283.5 eV vs q_z for the different PDB loadings studied. . . 87
4.15 Comparison of Brag rod oscillations at 250 eV and 283.5 eV. . . . 87
4.16 RCWA simulations of reflection CD-RSoXS experiment. . . . 90
4.17 RCWA simulations of transmission CD-RSoXS experiment. . . . 91

4.18 Experimental resonant CD-SAXS data, showing the first (blue), second (red), and third (yellow) order scattering intensity vs q_z. 93
4.19 Comparison of NEXAFS spectra collected in succession in the same sample location. 94
4.20 Measurement of resist absorption at 288.4 eV as a function of X-ray exposure time. 95

List of Tables

2.1 Input Parameters 14
2.2 Resist model parameters 28
2.3 Develop model parameters 30

3.1 Comparison of AFM probe parameters. f_0 is the frequency of the first harmonic in air, k is the probe stiffness, L is probe length and $< W >$ is the average probe width. Note the substantial drop in stiffness for the USC f1.2 k0.15 probe relative to the UHF Arrow, and the corresponding drop in probe dimensions. 61

4.1 δ and β values for exposed and unexposed photoresist at energies used for rigorous electromagnetic modeling. 88
4.2 Fit parameters for X-ray beam damage study. 96

Acknowledgments

This thesis would not have been possible without the help of many wonderful individuals. Many thanks to my research advisors, Andrew Neureuther and Patrick Naulleau for all their tutelage over the years, and for fostering a fantastic environment to learn and explore during my PhD. My gratitude also goes out to Professor Naomi Ginsberg for taking on extra responsibility as my Physics Department liaison, and for providing very thoughtful feedback on the manuscript. Thank you to Professor Ramamoorthy Ramesh for serving on my thesis and qualifying exam committees, and Professor Jeff Neaton for asking great questions at my qualifying exam. I would also like to acknowledge and thank the many scientists and engineers who helped enable my PhD and make my research an enjoyable experience: Paul Ashby for his invaluable help on AFM experiments and the occasional mid-afternoon espresso; Cheng Wang for his continued support on RSoXS experiments, always finding some beamtime for me in the otherwise very packed schedule, and always a good joke or two; the entire CXRO staff for creating an excellent, welcoming place to be a graduate student, and to Weilun Chao, Warren Holcomb, Martin Izquierdo, and Chanin King in particular for their help preparing, patterning, and measuring many samples over the years; the Marvell Nanofabrication Laboratory staff for maintaining a great facility, and in particular to Allison Dove for her support and training on electron beam lithography. I thank the many financial sponsors of my research for making this all possible, including the Center for Design Enabled Nanofabrication, Intel through its CINEMA and EUREKA programs, the US Department of Energy through the SCGSR Fellowship, and SPIE through the Nick Cobb Memorial Scholarship. I thank my mom for her undying love, for checking in on me, and for always encouraging me to follow my dreams, and I thank my stepdad, Greg, for fostering in me a curiousness and love of science at a young age. And finally, I thank my fiance, Kelley King, for her unwavering support of my academic goals, and for still loving me after lockdown in our tiny apartment with my loud, clackity, keyboard. This wouldn't have been possible without you.

Chapter 1

Introduction

1.1 Photolithography Basics

Photolithography is a light-utilizing printing technique that enables the manufacture of semiconductor chips, and is the unsung hero of modern computational technology. Today's semiconductor chips contain an astounding 100,000,000 transistors per square millimeter, each working in concert to perform the computations necessary for everything from casual Instagram scrolling to serious defense applications. These modern chips are the result of more than 50 years of steady, exponential improvement in integrated circuit technology, known as Moore's law after Intel CEO Gordon Moore. While Moore's law is fundamentally a statement about economics, it nevertheless has been driven by, or has itself driven, technological improvements in the ability to manufacture integrated circuits. Among a plethora of fabrication challenges, the most important step in microchip production is to define *where* the various circuit components belong, and furthermore, how to place them there repeatably and reliably. This is the role that photolithography plays in the process.

Figure 1.1 shows a basic schematic of how projection-print photolithography is used to define the location of circuit components on the wafer, a silicon substrate that mechanically supports the integrated circuit. First, light of a specific frequency is used to illuminate a photomask, which serves as a stencil for circuit design. As the light passes through the mask, the electric field is spatially modulated by the photomask either via absorption, phase delay, or both, causing the incoming radiation to diffract. Part of the diffraction pattern is captured by a lens, which ultimately results in the formation of an aerial image, the 2D map of electromagnetic intensity, at the wafer. Coated upon the wafer is photoresist, a material that is responsible for converting the light information transferred from the photomask to a physical structure that can be used for future steps in the fabrication process, for example etch of the underlying material, or deposition of a new material.

Each step in the above process has an impact on the maximum density of features that can be placed by a photolithographic process. Equation 1.1 is commonly used to define the resolution of the optical system by specifying the minimum pitch grating a system is capable

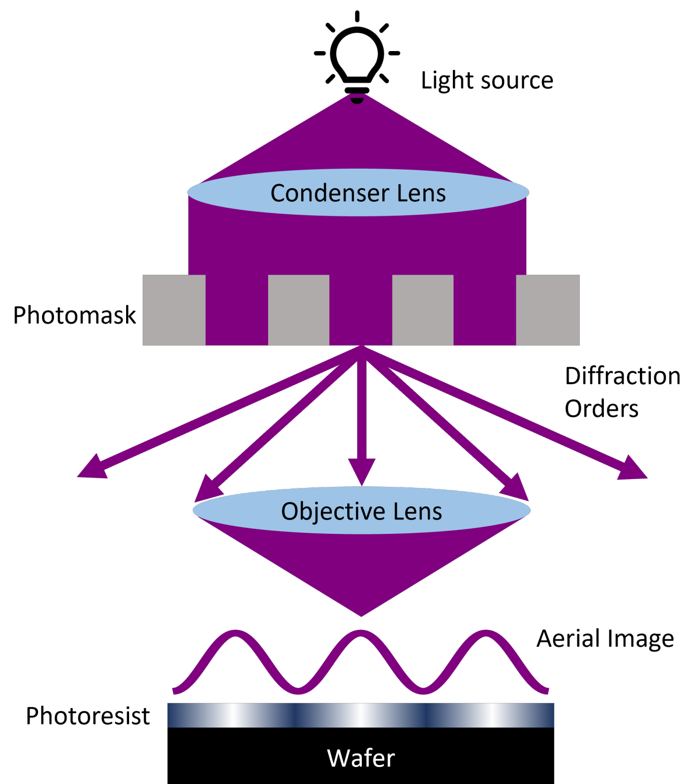

Figure 1.1: Schematic of the photolithography process.

of producing,

$$resolution = k_1 \frac{\lambda}{NA}. \tag{1.1}$$

In this equation, λ is the wavelength of light, NA is the sine of the half angle that defines the cone of acceptance of the lens and thus the maximum diffraction angle the lens will collect, and k_1 is a factor that accounts for various optical tricks, for example using off-axis light to illuminate the mask.

Moore's law has been driven by the industry's constant, historically successful push to reduce the resolution predicted by Equation 1.1. In particular, once a source wavelength has been settle upon, the NA and k_1 of the imaging system, as well as the resist and other associated down stream processes, are optimized until it is deemed that reducing the wavelength is a better economic choice than further extensions of the existing technology. The next section is dedicated to the most recent such wavelength reduction, the shift to extreme ultraviolet (EUV) sources, that was adopted for high volume manufacturing in 2019.

1.2 Extreme Ultraviolet Lithography

As show in Equation 1.1, one way to improve the resolution of the optical system is to reduce the wavelength of light that illuminates the photomask. To that end, the integrated circuit industry adopted the use of extreme ultraviolet (EUV) light in 2019 for usage in lithography[39]. At a wavelength of 13.5 nm, EUV represents a 14.3x reduction in wavelength as compared to the previous wavelength of 193 nm, known as deep ultraviolet (DUV). This is particularly dramatic when considering that the previous reduction, from 248 nm to 193 nm was only a 1.3x wavelength reduction. Such a dramatic reduction in wavelength is not without costs - EUV radiation poses a number of challenges that were not present in early lithography systems. At its core, this is because, at 92 eV of energy per photon, EUV radiation has enough energy to ionize every atom on the periodic table. Overcoming these challenges required nearly 40 years of scientific advancement to re-engineer nearly every part of the optical system.

Take for example, the lens, a crucial part of any imaging system. While lithographic scanners have traditionally relied upon complex systems of glass lenses to form aerial images, such lenses are opaque to EUV radiation. Instead, EUV lenses combine old tricks from astronomy, before the days of reliable lens crafting, with modern manufacturing techniques to create curved multilayer mirrors that steer and focus light in the scanner. For a comparison of old and new, consider Figure 1.2, which shows the 40 ft telescope and its 4 ft mirror-lens that William Hershel and his sister, Catherine, used to discover Uranus in 1781. In that era, refractive lenses of sufficient quality for the Herschels' studies could not be manufactured, so a large curved mirror was instead used to form an image up on the platform near the end of the telescope, where the observer (Catherine) made many astronomical discoveries. Compare this to Figure 1.3, showing the 0.33NA ASML scanner with its ten reflective mirrors and the massive 1 m, 0.55NA objective lens, which, though significantly more complex, relies on similar principles to the 1780's technology. One key difference is that, due to the EUV absorptivity of metals used in mirrors at optical wavelengths, the mirrors inside an EUV scanner must instead be made of a stack of 40 bi-layers of amorphous molybdenum and silicon that form a sort of one-dimensional synthetic crystal. The index of refraction difference between the molybdenum and silicon results in a weak reflection from each bi-layer. These weak reflections interfere constructively to achieve the optimal reflectivity for the multilayer design. Due to the small absorption ever present in these materials, some loss is incurred upon each reflection. The reflectivity of an EUV mirror peaks at about 70 %.

The ionizing nature of EUV radiation also has an impact on the achievable numerical aperture of the optical system. In the most advance DUV scanners, an immersion fluid is placed between the scanner and the wafer, enabling the optical system to achieve a NA of 1.35. However, as these fluids would absorb an appreciable amount of 92 eV light, this too is ruled out. Instead, the NA of the system is effectively set by the size of the mirror, which, as indicated by Figure 1.3, is about one meter in the 0.55NA tool ASML is currently producing, approaching the size of the Herschels' telescope lens.

Producing EUV light is itself a challenge that long threatened the viability of EUV

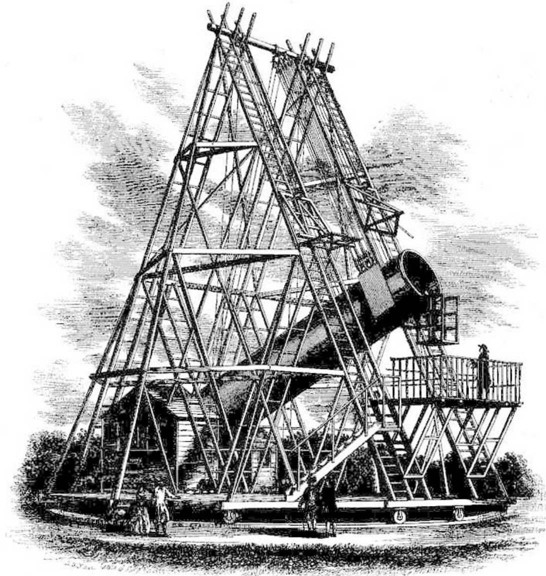

(a) Herschel 40 ft telescope

(b) Herschel 4 ft mirror-lens

Figure 1.2: Herschel telescope

(a) Inside of ASML's 0.33NA EUV Scanner

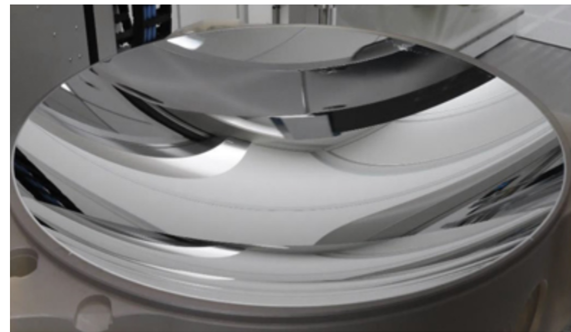

(b) ASML 1 m 0.55NA lens

Figure 1.3: ASML Scanner and Multilayer Mirror-lens

lithography. As discussed above, the EUV scanner contains 10 mirrors, plus a photomask, which itself is a mirror, for a total of 11 reflections between the source and the wafer. With a peak reflectivity of 70 %, the result is that only about 2 % of the EUV radiation from the source actually reaches the wafer. Insofar as the mirrors cannot be further optimized, this places a large burden on the bookends of the optical system; the source needs to produce as much light as possible, and the resist must make do with the limited amount of light it receives. Fortunately, years of engineering have resulted in a source with adequate power for industrial EUV lithography. The industrial source generates EUV by bombarding a stream of molten tin droplets with two pulses of infrared light - one to shape the droplet into a pancake-like structure, and a second, more intense pulse to produce a plasma that in turn produces the desired EUV light. As one might imagine, the amount of EUV light produced by this process is a function of a large parameter space that is constantly being explored to increase EUV source power.

As hinted at above, a final major change resulting from the shift from DUV to EUV is with regards to the photoresist. While the scanner may be able to produce a pattern with a size specified by Equation 1.1, all this is for naught if the photoresist is unable to record the pattern with sufficient fidelity. Indeed, in modern semiconductor manufacturing, it is believed that it is the photoresist which represents the most daunting challenge for further transistor count scaling. It is this challenge that has motivated the work presented in this thesis, and as such, is discussed separately in the next section.

1.3 Photoresist

With all the carefully produced, shaped, and aimed light finally reaching the wafer, the photoresist must use the light to enable further processing of the substrate. This is achieved by a light-induced chemical change that enables selective removal of the photoresist material to form a physical structure resembling that of the photomask design, though at a 4x reduction in spatial dimension. The resulting physical structure is then itself used as a mask, typically one that "resists" an incoming etchant. This process motivates some properties that a good photoresist should have:

1. Appreciable absorption of the incoming radiation
2. Ability to undergo a photo-activated chemical change that enables selective removal of unwanted photoresist material
3. Ability to *faithfully* resolve the features being patterned, i.e. containment of the photo-activated chemistry to the desired region
4. Resistance to the etchant(s) used to process the underlying material(s)

The first step of these processes is a requisite for the rest, and takes even more importance in the case of EUV photoresist. In order for the light to drive any chemistry in the

material, it must first be sufficiently absorbed. As discovered by Einstein, this absorption process is not continuous, but rather in discrete energy packets owing to the fact that light is discretized as photons. As a result, in spite of the light given to the resist being specified in energy per area, the actual absorption of the light occurs in a countable number of photons, a number that fluctuates randomly according to Poisson statistics[12]. Herein begins a fundamental challenge for EUV photoresist as opposed to it's DUV predecessors: Not only is EUV radiation more penetrating than DUV, resulting in a lower fraction of the incoming radiation being absorbed by the resist material, but every EUV photon absorbed contains 14.3 times as much energy a 193 nm DUV photon. Thus, for a particular volume of resist material absorbing a set amount of energy, there are 14.3 times fewer photons if that energy was delivered via EUV photons as opposed DUV photons. The net effect of this change, especially when coupled with EUV source limitations and industrial throughput requirements, is that the absorption profile of EUV suffers from "shot noise" effects, in which the absorbed pattern of light consists of random, scattershot-like points of EUV absorption, rather than the smooth light intensity distribution of the aerial image. When propagated through the material processes that convert the incoming radiation into a physical resist structure, this pattern randomness manifests as imperfections in the pattern features.

A natural solution to this problem would be to increase the number of EUV photons used to expose the resist. However, the economics of the semiconductor industry always benefits from increasing the number of chips made per unit time. As increasing the number of EUV photons requires slowing down the exposure (or increasing the source power, itself a challenge), the best solution from the industry's perspective is to absorb as many of the incoming photons as possible. (There are limits to this absorption, as the resist material is 3D, but they turn out not to be relevant given the thickness of modern resist and the EUV cross section of current materials).

The next issue that arises with the absorption of EUV photons is that, at 92 eV, the absorption process is inherently ionizing, rather than resonant, as is the case for photoresist absorption of UV radiation. As a result, it is the photoelectrons that are ionized from the absorbing material, as well as a subsequent "cascade" of lower energy electrons that result from the interaction between the primary photoelectron and the surrounding resist, that are primarily responsible for initiating the "photochemistry" inside these materials[24]. This process is a double edge sword for EUV photoresist. On the one hand, the cascade of electrons has an amplifying effect in which each absorbed photon can affect multiple sites in the resist. This helps to increase the effectiveness of each absorbed photon, mitigating some of the shot noise characteristics mentioned above[32]. However, because the electrons migrate from the initial absorption site, the cascade process effectively "blurs" the absorbed energy distribution. For some classes of materials, this electron blur, usually on the order of a few nanometers, may ultimately limit the resolution of what can be patterned.

The absorption of EUV photons and the electron cascade must ultimately drive a chemical change in the photoresist that enables unwanted material to be selectively removed. There are several different classes of photoresist material which operate on different underlying principles. In the subsequent discussion, and for much of this thesis, I will focus on a

stalwart of the semiconductor industry, the chemically amplified resist (CAR). In this system the photoresist is comprised of a polymer, initially containing a non-polar ”protecting” group that causes the material to be insoluble in aqueous base. Added to the polymer is a photo-acid generator (PAG), a compound that becomes a strong acid upon photon (or electron) activation. Following exposure, the photoresist undergoes a post-exposure bake (PEB), which enables diffusion of the generated acid as well as reaction of the the acid with the protecting groups. This “deprotection” reaction leaves behind a polar group, which dissolves in aqueous base. The differential solubility of the deprotected polymer is what enables the selective dissolution of the resist.

The name “chemically amplified” resist comes from the fact that each acid can deprotect multiple sites on the polymer. However, just as the electron cascade provides both amplification and blurring of the photon image, acid diffusion during the bake causes an additional blur in the resist. Ultimately, it is the combination of the electron and acid blurs that limit the resolution of CAR, as these processes spread out the exposure information into the nominally dark areas of the aerial image. As will be discussed in greater detail later in this thesis, there are chemical tricks that aim to remedy these fundamental problems, notably the inclusion of chemically basic “quencher” molecules that render the photo-generated acid inert to the polymer. However, these tricks come at their own cost. Just as the absorbed photon counts are random in nature, so too are the chemical counts of the photoacid generator and quencher molecules loaded into the polymer host material. In fact, even the number of protecting groups are randomly distributed between polymer molecules. Each of these random effects conspires to limit the faithfulness with which the resist can reproduce the aerial image.

A succinct description of these challenges is given by the “Resolution, Line Edge Roughness, Sensitivity,” or RLS, tradeoff. This describes the fundamental difficulty that comes with producing a resist that can simultaneously resolve small lines, do so with good fidelity (low roughness along line edges), all while doing so at as low a dose as possible such that the process is profitable. As the name suggests, these terms can be traded off for one another. For example a resist may be patternable at a very low exposure dose, but the resulting shot noise effects will result in large line edge roughness. An acid with large blur could be designed to smooth out the randomness from the photon shot noise, but ultimately this will limit the resolution. Conversely, a resist could be designed that is capable of resolving very small features. To do so, the blur effects must be kept to a minimum. As a result, un-smoothed photon shot noise will result in unfaithful reproductions of the aerial image. To counter these effects, the resist must be designed such that a large number of photons are required for patterning, which lowers process throughput, increasing cost.

Finally, the material must be compatible with the rest of the process, as a resist that meets the above criteria but cannot be used as part of the greater process is of no use at all. This has implications in particular for film thickness, as no etch process is perfectly selective to the material under the photoresist. On the other hand, at small feature sizes, this may require patterning the resist to be substantially thicker than the features are wide, which poses mechanical challenges, particularly during the develop of the material. While

not the focus of this thesis, it is nonetheless important to keep the end-use of the resist in mind when thinking about optimization of other resist parameters.

1.4 Thesis Structure

The research presented in this thesis is centered around understanding the photoresist, in particular the associated stochastic effects, as a system, beginning with the introduction of photons via the aerial image and ending with a final developed structure. In between are the critical steps of the electron cascade, post exposure bake, and finally resist development, each of which must work in harmony if a material is to be a viable part of the manufacturing process. To that end, the first chapter of this thesis addresses this topic from a theoretical standpoint using a stochastic resist simulator. This model treats the photoresist a system, beginning with the randomly-distributed ingredients of patterned photoresist - absorbed photons, PAG, and quencher additives - and combining them with various blur and reaction effects that serve to mix these ingredients together to form a final resist structure. The inherently 3D nature of resist materials is also discussed, with some insights into how this dimension could be used to improve resist performance. The next two chapters focus on means to measure the modeled effects, with particular emphasis on understanding PEB and dissolution. These issues are addressed using atomic force microscopy and X-ray scattering, experimental techniques with the potential to make measurements at the single-digit nanometer scale. Finally, I conclude with some summary remarks about the research presented in the body chapters of this thesis, with a few notes about the future directions the work presented here may take given new government funding into patterning materials research and development.

Chapter 2

Stochastic Photoresist Modeling

This chapter outlines stochastic modeling of EUV photoresist. This modeling forms the basis for understanding, on a conceptual level, the various resist processes and how they contribute to the RLS tradeoff. The model is further used to address several techniques for improving resist performance, both through chemical means that are currently being employed, as well as evaluating hypothetical solutions and what kind of effect researchers may expect should these means be realized.

2.1 Multivariate Poisson Propagation Model

The Multivariate Poisson Propagation Model (MPPM) is a stochastic resist model developed to connect physically-measureable parameters with observed resist behavior[33][31][32]. At its core, the model seeks to account for the random distribution of photons and resist components that result from the fundamental quantization of light and matter and to propagate these random distributions through the PEB in a deterministic way to produce physically reasonable results.

The first key step in the model is to account for the absorbed photon distribution inside of the model. This is done first by computing the mean number of photons in each model cell by combining resist absorption of 92 eV light, aerial image intensity, model cell dimensions, and then applying Beer's law. This mean value can then be randomized by noting that physically realized photon counts are distributed according to a Poisson distribution[12],

$$P(X = k) = \frac{\lambda^k e^{-\lambda}}{k!}, \tag{2.1}$$

where X is the random variable, k is a possible value for X, and λ is the mean value of the distribution. The Poisson distribution has the interesting property that the variance of the distribution is also λ; as a result, the signal to noise ratio of a Poisson process increases with the mean value as $\sqrt{\lambda}$. This describes the fundamentals of the shot noise problem, as to double the signal to noise, four times as much dose is required, which corresponds to 1/4 the

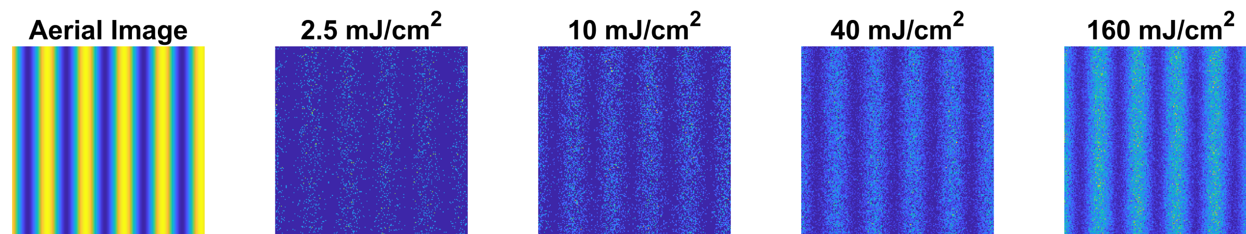

Figure 2.1: An illustration of absorbed photon distribution as aerial image intensity is increased

throughput of the patterning process. Figure 2.1 illustrates the improved absorbed photon image as the dose applied to the resist is increased. Clearly, the higher dose results in a pattern that more closely resembles the initial aerial image.

The next step in the model is to populate the model with counts of photoresist additives and protecting groups. To do so, the Poisson distribution is again used, but in this case using the nominal component loading as the mean. Just as increased dose improves the fidelity between the aerial image and the absorbed photon distribution, increased component loading results in a more uniform map of resist components. However, here the resist is constrained by the two factors. The first is that, at high loading, PAGs, which are often onium salts, tend to aggregate in the non-polar polymer resist host, countering the homogeneity benefits of the large concentration. Secondly, at large enough loading, the dissolution properties of the resist cease to be controlled by the polymer and associated deprotection chemistry, and more by the dissolution properties of the PAG. The quencher is similarly constrained by these effects, with the additional constraint that, for a conventional quencher, if the quencher and PAG counts are equal, the quencher will cancel out the acid before it has a chance to deprotect the polymer.

To convert the PAGs into acids, the electron cascade that results from each absorbed photon must be accounted for. In the MPPM, this is done using yet another random variable to capture the efficiency of each photon with respect to generating acid, as well as blur kernel to account for the electron spread from the photon absorption site. Experimentally, it has been measusured via titration techniques that, on average, between 2 and 4 acids are generated for each photon, depending on PAG concentration[6]. To account for variation in this process, the photon count in each model cell is multiplied by a random number, again picked from a Poisson distribution, with a mean centered on the expected number of acids per photon. This amplified image, which represents the "effective" electrons, or those actually participating in chemical modification of the film, is then convolved with a Gaussian point spread function. The width of this function is set around 2 nm in accordance with an abundance of literature measuring this to be the inelastic mean free path of photoelectrons in resist material[3][23]. Finally, this effective electron image is combined with the PAG image assuming exponential decay of PAG (and exponential production of acid) with the number of effective electrons in the vicinity of each PAG.

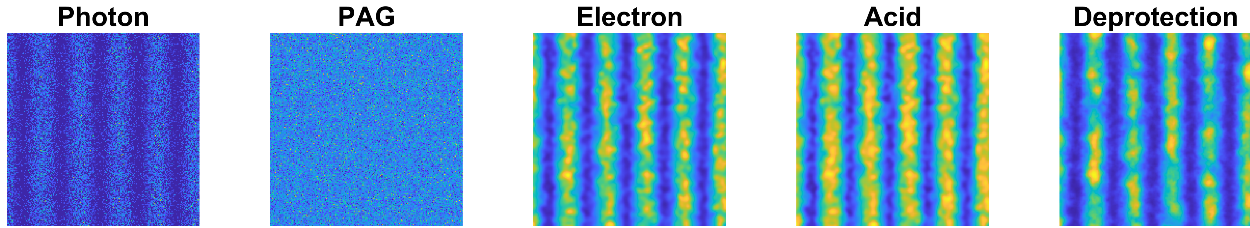

Figure 2.2: An illustration of the noise propagation from absorbed photon to final deprotection image.

At this point in the model, three random variables, the photons, PAG counts, and effective electrons, have been combined to give a new, derived random variable, the acid image. In the next step of the model, this random image is again propagated forward in a reaction-diffusion simulation of the PEB process to produce the random deprotection image. This process is simulated by assuming the acid and quencher diffuse according to Fick's law, and that the reactions between acid, quencher, and protecting groups can be written as follows:

$$\rho_a = D_a \nabla \rho_a - k_q \rho_a \rho_q \tag{2.2a}$$

$$\rho_q = D_q \nabla \rho_q - k_q \rho_a \rho_q \tag{2.2b}$$

$$\rho_d = k_d (1 - \rho_d) \rho_a \tag{2.2c}$$

where a, q, and d are acid, quencher, and deprotection, respectively, Ds refer to diffusivities, and ks refer to reaction rates.

An example of the noise propagation process is given in Figure 2.2. The deprotection image at the far right can then be thresholded to extract line edges and the statistics describing the edge randomness. Of particular interest are the critical dimension (CD), or average line width, the line edge roughness (LER), which refers to the 3-σ deviation from the average edge, and line width roughness (LWR), the 3-σ deviation of line width from the CD.

Additionally of interest is not just the roughness values, but their spectral content, given by the power spectral density (PSD). The PSD of the random process illustrated in Figure 2.2, as measured at the nominal line edge, is plotted at several of the model stages in Figure 2.3. In this figure, the low frequency component of the process noise is normalized to one to highlight the shape of the PSD. In some sense, the PSD tells the clearest story of the resist as an information processing system. Light impinges upon the resist, and is randomly absorbed. The spectral content of this random absorption pattern is white, or equal power, at all spatial frequencies. Next, the electron cascade serves to amplify and blur this photon image in converting PAGs to acid inducing correlations between adjacent locations in the acid image. Finally, the acid image induces even more correlation via the reaction-diffusion process in the deprotection image. The result is that the initially-white noise of the photon absorption process is convolved with a non-linear low-pass filter that is described by the electron cascade and subsequent reaction-diffusion process. While not accessible experimentally, the model

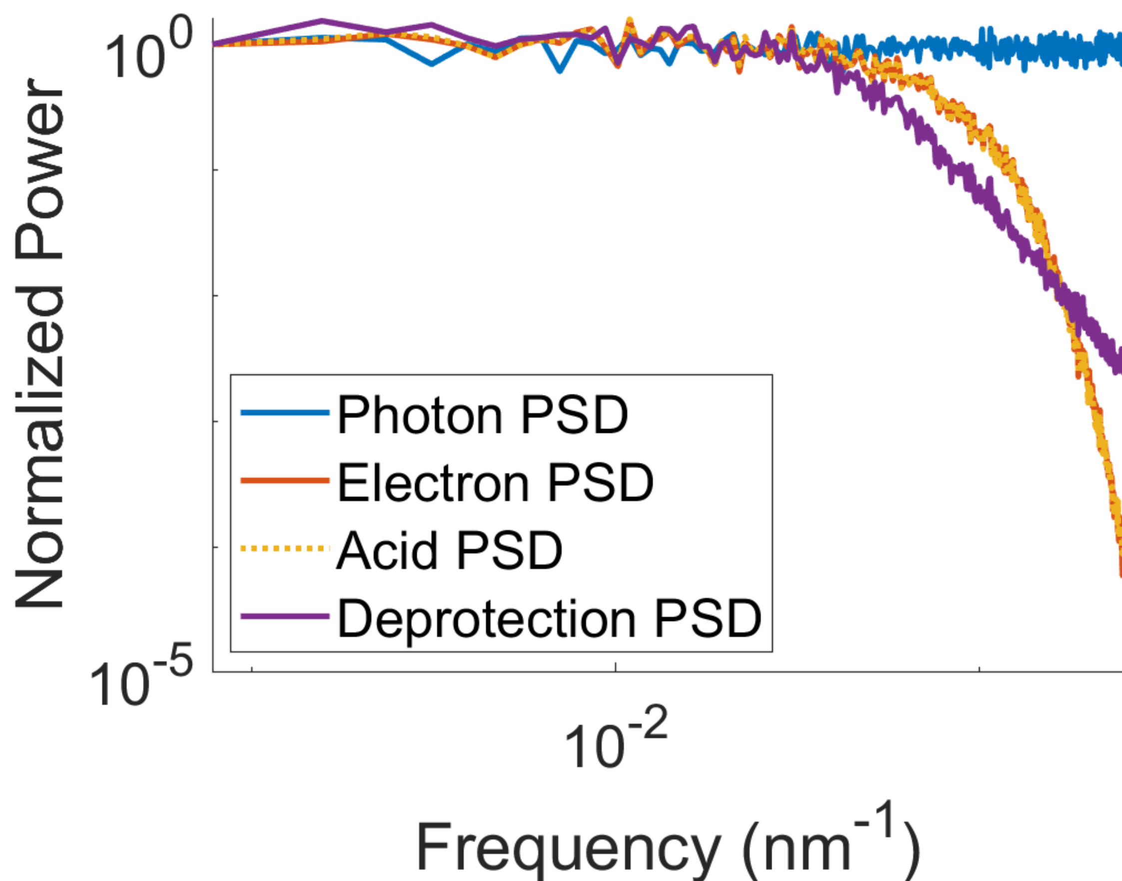

Figure 2.3: PSD of process components at the line edge

allows all this history to be probed incrementally throughout the patterning process, as illustrated in Figure 2.3. The ultimate success of the model is rooted not just in predicting CD and LWR as a function of dose, but also the ability to predict LER/LWR PSDs and connect them to real physical processes.

A final benefit of the model is that it enables ability to treat any set of random variables deterministically, which allows the impact and interaction of the random variables to be studied[32]. For example, by turning off the photon stochastics, one can probe the role of the material itself in propagating LER/LWR. This has implications for the ultimate limit of the material: even if industry could stand a significant throughput hit (or generate more photons to compensate), what is the best performance one can expect from a resist?

2.2 Study - Photodecomposable Quencher and the noise-slope tradeoff

In this study, the MPPM is used to evaluate the costs and benefits of several types of quencher used in CAR resist. As previously mentioned, quencher is often added to the resist formulation to limit the impact of acid diffusion to unexposed regions of resist. While this has proven an effective way to limit the acid blur, previous work has shown that it comes at a cost in terms of resist stochastics [32][15]. In order to mitigate the negative stochastic effects of quencher and to increase the photospeed of the resist, top-performing CAR resists are engineered with photodecomposable base (PDB), a photoactive base that self-quenches when activated by EUV light. Previous modeling work suggests that in printing 25 nm line/space patterns, this system has the potential to reduce the LER at a given dose relative to a conventional quencher [4]. In this paper, the LWR/Dose trade-offs of conventional CAR (NPDB) and PDB in printing 16 nm line/space patterns are re-examined. The model is then extended to the analysis to PSCAR 2.0[30], a relatively new member of the CAR lineage that utilizes the initial EUV patterning step to activate a photosensitizer which can in turn be used to produce more acid during an UV exposure step.

2.2.1 Modeling Approach

2.2.1.1 Input parameters

The input aerial image was the simulated output of a 16 nm 1:1 line/space pattern from a 0.3 NA exposure tool. The approach of this study was to analyze the impact of quencher loading in the three systems under study by adjusting the dose as necessary to maintain a 16 nm post-development CD. All other parameters are held constant as the base loading is changed, except the total quantum yield of PDB and PSCAR, as discussed in Section 2.2.1.4. In this way, the effect of base loading is simulated using an approach comparable to one a resist chemist might employ to optimize base loading via experiment. Table 2.1 shows the input parameters to the model. f(Base) indicates the base loading dependence of the quantum efficiency in PDB resist.

2.2.1.2 Modeling of PDB

A prototypical PDB consists of a photoactive group attached to a basic quenching ion such as hydroxide[11]. Upon photodecomposition, the base group associates with a proton produced via the decomposition of the photoactive group. The base is thus used to quench its own photogenerated acid, lowering the quencher concentration in the exposed regions of the resist. In this model, it is assumed that the proximity of the base group and the acid produced by photodecomposition leads to an instantaneous quenching reaction. Furthermore, it is assumed that this reaction is irreversible. Thus, any additional acid produced by the

Table 2.1: Input Parameters

Parameter	**Value**
PAG	$0.2\,\mathrm{nm}^{-3}$
$Base$	Variable
$blur_{Acid}$	12 nm
$blur_{Base}$	6 nm
$blur_{electron}$	2 nm
k_{ab}	$10\,\mathrm{nm}^3/\mathrm{s}$
$k_{deprotection}$	$3\,\mathrm{nm}^3/\mathrm{s}$
QE_{NPDB}	2.08
QE_{PDB}	f(Base)
$absorptivity\ (\alpha)$	$4.3\,\mu\mathrm{m}^{-1}$

decomposition of base contributes only to reducing the local quencher concentration, not to deprotection of the polymer.

2.2.1.3 PSCAR 2.0 Modeling

While a more detailed picture of PSCAR 2.0 can be found in [30], a summary is provided here. PSCAR is an extension of the CAR lineage, differing from its more conventional counterparts by the addition of a spatially-controlled UV sensitizer step. A schematic of the process produced by the model can be found in Figure 2.4, which compares qualitatively to those presented in [30]. In PSCAR 2.0, the initial EUV exposure step is used to produce acids as well as decompose base. This initial chemical distribution then activates a photosensitizer from its precursor molecule during a room temperature reaction step (RTB for room temperature "bake" in Figure 2.4). In the process, acid and base from the initial exposure react, increasing the chemical gradient. Upon exposure to UV light, the sensitizers can further activate PAG and decompose base. Finally, the post exposure bake induces the reaction diffusion process as in conventional CAR.

2.2.1.4 Quantum Efficiency Modeling

As the number of electrons per EUV photon is finite, introduction of PDB will induce a competition for photoelectrons between PAG and PDB. A model is thus required to partition the efficiency of each photon between the PAG and PDB. The efficiency of each photon is parameterized by a quantum efficiency (QE) variable, which represents the average number of photosensitive molecules activated per photon. Consistent with previous modeling on PDB with the MPPM [4], the total QE was modeled according to a saturation equation as illustrated experimentally in reference [6]. The maximum achievable QE was set to 4.5 based

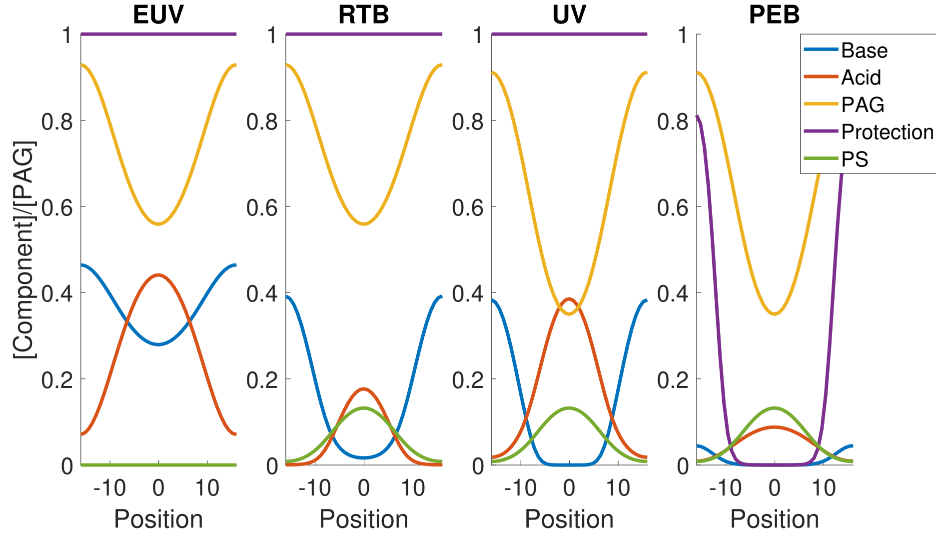

Figure 2.4: PSCAR 2.0 Process.

on the experimental data, and the exponential coefficient set such that the PAG loading alone gives a QE of 2.08. Then a new total QE was calculated according to the total amount of photo-active compound ($PAC = PAG + PDB$), which was then split between the PAG and PDB according to their fraction of total PAC. The QE equations are shown in Equation 2.3,

$$QE_{tot}(PAC) = QE_{sat}e^{-\alpha PAC}, \tag{2.3a}$$

$$QE_{PAG}(PAC) = \frac{PAG}{PAC}QE_{tot}(PAG), \tag{2.3b}$$

$$QE_{Base}(PAC) = \frac{Base}{PAC}QE_{tot}(PAG). \tag{2.3c}$$

As seen in Figure 2.5, the effect adding PDB thus increases the total QE, but decreases the efficiency of each photon with respect to PAG activation. While in this study it is assumed that the cross section of the electron-PAG and electron-PDB interactions are equivalent, the model could be modified if experimental evidence for a preferential reaction pathway is discovered.

2.2.1.5 Modeling of UV Sensitization in PSCAR

In order to model additional acid generation in PSCAR via UV exposure, a random variable for the quantum efficiency of the photosensitizers was used. As the UV dose used during this step is on the order of J/cm^2[30], the UV photons are not expected to be significant contributors to the overall resist stochastics. However, there is still certain to be some fluctuation in the number of activation events stemming from each photosensitizer (PS)

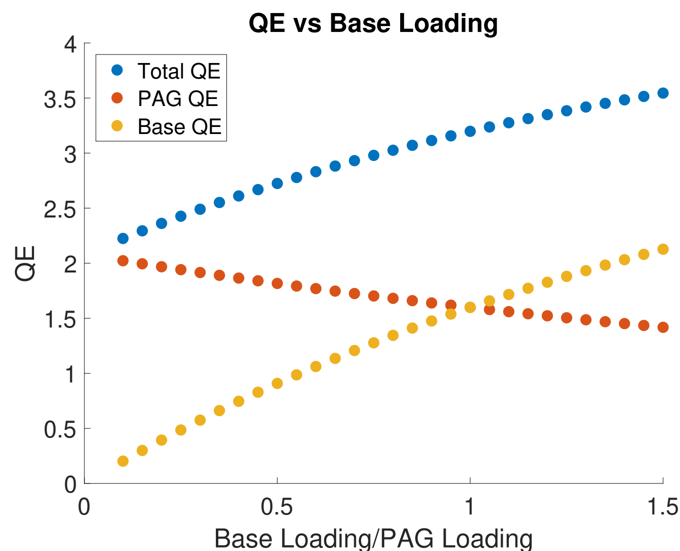

Figure 2.5: Quantum efficiencies as a function of base loading for PDB resist. As base loading increases, the overall QE increases, but acid generation efficiency decreases due increased photoelectron competition.

due to randomness in the sensitization process. The quantum yield variable is intended to account for this randomness.

Of additional concern in the PSCAR 2.0 system is that the photosensitizers are capable of decomposing base as well as activating PAG. A simple model predicts that the relative probabilities of PAG activation and base decomposition are given by the relative concentrations of each component. As in the discussion above, the result would be a decrease in the acid yield per sensitizer as the concentration of PDB is increased. However, because UV photons are essentially free in comparison to their EUV counterparts, it was assumed that the UV dose can be increased in the presence of PDB in order to keep the PAG yield constant. These additional photons apply themselves to the decomposition of PDB. In sum, the net efficiency of the sensitizers was modeled as a linearly increasing function of PDB concentration, owing itself to an underlying increase in UV dose.

2.2.2 Simplified Models

While the MPPM provides numerical simulation results, the trends can be challenging to interpret. In this section, several simplified models are put forth which are useful in understanding the simulation results.

2.2.2.1 Noise/Slope

It has been established that LER originates from a combination of deprotection noise and deprotection slope[12][5]. In essence, this captures the fact that LER is a function of how much the deprotection at the nominal line edge is deviating from the developable threshold, and when it does, how far that deviation shifts the realized line edge. This idea is represented mathematically in Equation 2.4. As validation that the MPPM adheres to this relationship, Figure 2.6 compares the LER as measured using the lithography analysis package SuMMIT[36] and that computed via the noise/slope model. The good agreement suggests that fluctuations in the line edge position can be analyzed in terms of two terms: the numerator of Equation 2.4, which encompasses the various stochastic components as they propagate to the deprotection image, and the denominator, which accounts for the deterministic conversion of aerial image to deprotection profile.

$$LER = \frac{3\ \sigma_D}{\frac{dD}{dx}} \tag{2.4}$$

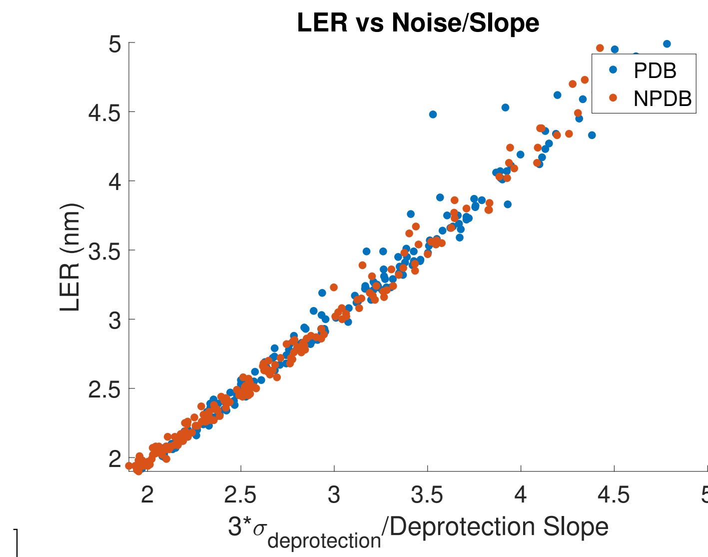

]

Figure 2.6: Measured LER vs Noise/Slope model.

2.2.2.2 Relative Noise

A previously published model[32] of relative noise is useful in understanding stochastics in the deprotection image. In summary, this simplified model treats the net acid (A) as the sum over the number of absorbed photons (P) of the yield (Y) of each photon, minus the amount of base quencher (Q). Each of P,Y, and Q are independent random variables. Using the tools of probability, the expectation value and variance of net acid can be calculated.

As deprotection is ultimately a relative quantity, and as it stems directly from the acid-deprotection reaction, this model provides a simplified picture of the origins of deprotection noise. This model for net acid, as well as its expectation value and variance are shown in Equation 2.5.

$$A = \sum_{i}^{P} Y_i - Q \tag{2.5a}$$

$$E[A] = E[P]E[Y] - E[Q] \tag{2.5b}$$

$$Var[A] = E[P]Var[Y] + Var[P]E[Y]^2 + Var[Q] \tag{2.5c}$$

This model can be extended for use in the case of a photodecomposable base. Here, an extra term needs to be added to account for the additional yield from each photon dedicated to decomposing base. The modified simple noise model is shown in Equation 2.6. These equations will be examined in further detail in the results section.

$$A = \sum_{i}^{P} YA_i - Q + \sum_{i}^{P} YQ_i \tag{2.6a}$$

$$E[A] = E[P]E[YA] - E[Q] + E[P]E[YQ] \tag{2.6b}$$

$$Var[A] = E[P](Var[YA] + Var[YQ]) + Var[P](E[YA] + E[YQ])^2 + Var[Q] \tag{2.6c}$$

2.3 Results

2.3.1 LWR

Figure 2.7 contains the MPPM LWR and dose vs base loading results for the three resist platforms studied. The discussion will begin with the conventional base resist data (blue). Consistent with previous modeling [32][15], as well as experiment [29], an increase in base loading initially leads to a reduction in LWR, bottoming out at a value of about 3.6 nm at 55 % base loading for the parameter set used in this study. After this point, increasing the base loading leads to an increase in LWR. In addition, Figure 2.7 shows that, as expected, the dose required to achieve a 16 nm CD (hereafter known as the “dose to size”) increases rapidly as a function of base loading. In comparison, for both PDB and PSCAR 2.0, LWR strictly decreases as a function of the base loadings simulated. More importantly, the LWR for PDB and PSCAR is less than that of NPDB at the same dose, with the PSCAR and PDB LWR curves nearly overlapping. For the more complicated resist types, the dose to size is a linear function of base loading. Additionally, as would be expected based on an increase in total quantum efficiency, the required dose at a given base loading is less when the base is photodecomposable. Because quencher is destroyed during exposure, base loading can be higher than PAG loading in PDB and PSCAR. The moderate increase in dose at each base

loading for PSCAR in comparison to PDB is due to some of the initial acid produced during the EUV step being spent during the room temperature reaction process and not recovered by sensitization. In the following sections, these results are analyzed, with an emphasis on whether the noise, slope, or both is responsible for the improvement in LWR at a given dose for PDB and PSCAR 2.0.

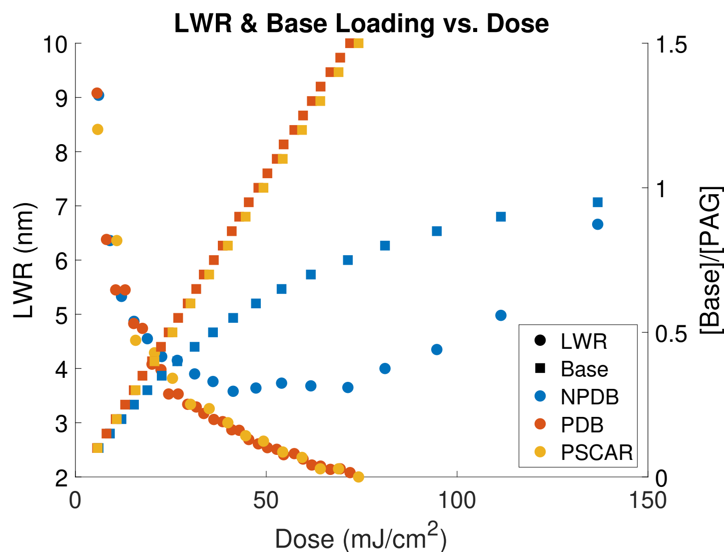

Figure 2.7: LWR vs Dose for all three resist platforms. The different colors refer to the photoresist type, while circles correspond to LWR (left) and squares refer to base loading (right).

2.3.2 Noise

Deprotection noise at line edge as a function of dose can be found in Figure 2.8. Comparison with Figure 2.7 shows that improvements in deprotection noise are not responsible for the lower LWR at a given dose in PDB and PSCAR 2.0, as PDB is noisier than NPDB, and PSCAR is the noisiest of the three. Additionally, the LWR trend in NPDB does not match the noise trend. Nevertheless, Equations 2.5 and 2.6 can be used to compare the noise values for each of the resist types. The comparison suggests that the variance of the net acid increases at a given dose when the base becomes photodecomposable due to the increase in the total quantum efficiency of the material. In essence, because each photon plays a bigger role in the net acid produced, the overall importance of the photon shot noise is enhanced. In PSCAR, because the initial acid is responsible for activating the sensitizers, which in turn produce more acid, there is even more emphasis on these initial photons.

In Figure 2.9, the deprotection noise at line edge is plotted as a function of dose when each of the various noise terms is treated separately from the others. For NPDB, it is seen

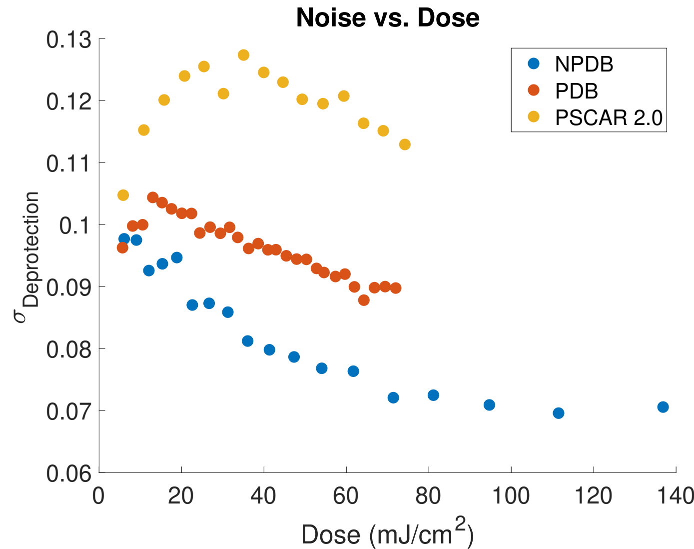

Figure 2.8: Total Noise vs. Dose

that at all but the lowest doses, the base is the dominant contributor to deprotection noise. As suggested by Poisson statistics, the relative importance of the photon shot noise decreases as the dose increases, as does the quantum yield. The noise due to base, however, remains more or less constant as the base loading (and thus dose) increases. This imposes a material limit on the noise performance of the resist given a set of blurs and reaction rates that cannot be improved upon even in the limit of zero photon shot noise. This material limit is discussed in [32]. In PDB, the absolute noise from base alone is similar to that in NPDB. However, as heuristically argued above, the photon noise is greater. As the quencher loading is increased, the increased workload of each photon effectively amplifies the photon shot noise relative to NPDB. In other words, while the actual distribution of photons at a given dose is the same for the three resist platforms, the effect of that noise on the deprotection image is magnified. PSCAR 2.0, also containing PDB, shows similar noise trends, with additional emphasis on the initial photons as previously argued. The base contribution also increases as it helps to shape the sensitizer image and thus the acid image responsible for deprotection during PEB.

2.3.3 Slope

The noise/slope model suggests that if PDB and PSCAR produce noisier deprotection images, then they must also produce images with better slopes in order to to achieve improved LWR. As seen by comparing Figures 2.7 and 2.10, the general shape of the LWR vs dose curve matches that of the slope vs dose curve. This highlights the importance of the deprotection slope in determining the final LWR of the resist as reported in [29] and [4]. It is thus worth trying to understand the origin of the slope trends.

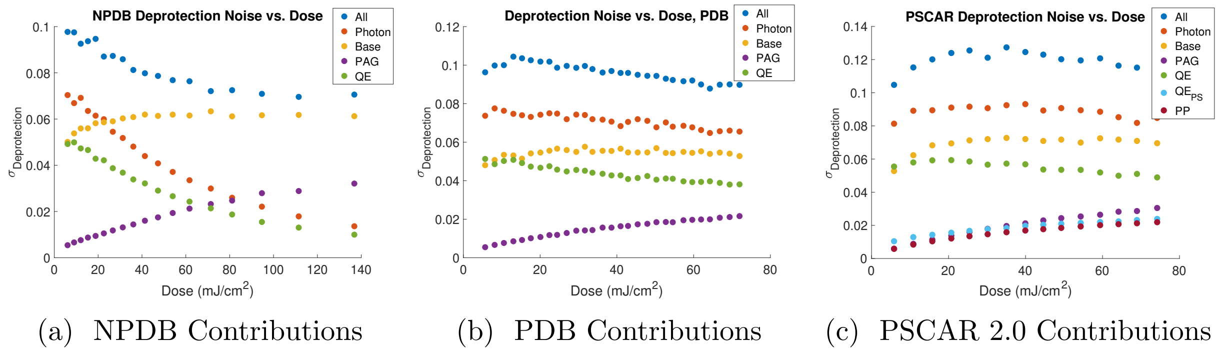

(a) NPDB Contributions (b) PDB Contributions (c) PSCAR 2.0 Contributions

Figure 2.9: Breakout of different noise contributions

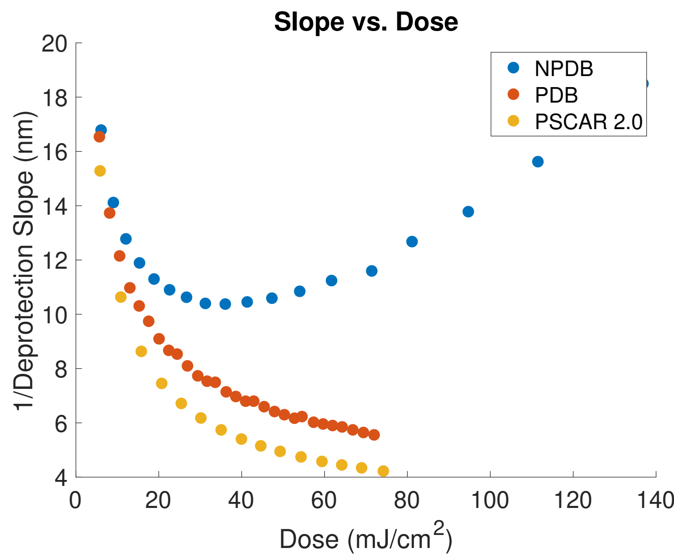

Figure 2.10: PSCAR 2.0 Slope vs Dose.

The beginning of the post exposure bake process is when the chemical gradients and concentrations are their highest. Thus, the most rapid reaction and diffusion happens during this period. A logical place to look for the root of the deprotection slope trends is thus the initial chemical concentrations before PEB. Figure 2.11 shows the initial acid and base profiles for three different base loadings in NPDB. Two things stand out from these profiles. The first is that, as the base loading increases, so does the absolute acid slope and amount of acid at the line edge, as expected. The second is that, at 80% base loading, the top of the acid peak is starting to become flatter than in the lower base loading profiles. This is due to the limited amount of PAG in the resist. As the resist becomes more and more saturated, extra dose pushes the saturated part of the acid profile out away from the center of the line

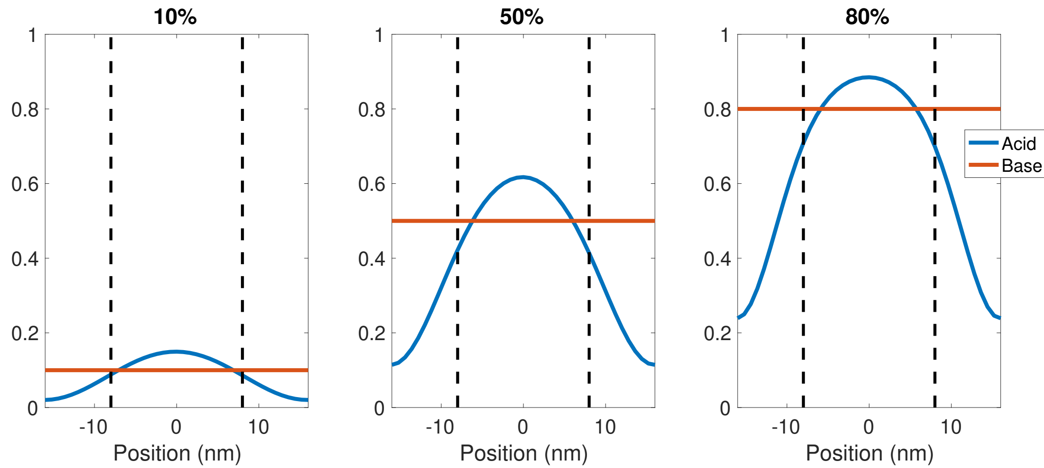

Figure 2.11: NPDB Acid Profiles. Concentrations normalized by PAG loading.

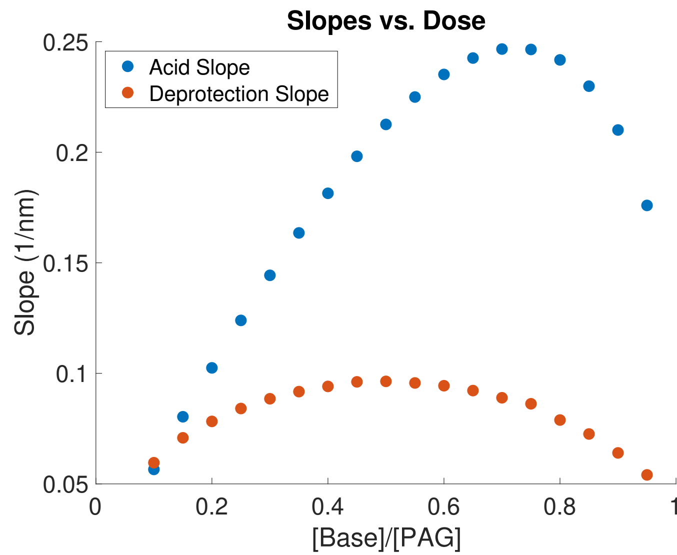

Figure 2.12: NPDB Acid and Deprotection Slopes.

toward the line edge, reducing the slope. This turn around in acid slope is evident in Figure 2.12, though it happens at a higher base loading than the degradation of the deprotection slope. This discrepancy can be ascribed to the cost of having extra acid at the line edge. Using the deprotection reaction rate equation, an equation can be produced for how the

deprotection slope is changing in time:

$$\frac{\partial}{\partial x}[\frac{\partial \rho_D}{\partial t}] = \frac{\partial}{\partial x}[k_D \rho_{acid}(1 - \rho_D)] \tag{2.7a}$$

$$\frac{\partial}{\partial t}[\frac{\partial \rho_D}{\partial x}] = k_D(\frac{\partial \rho_{acid}}{\partial x}(1 - \rho_D) - \rho_{acid}\frac{\partial \rho_D}{\partial x}],. \tag{2.7b}$$

The first term on the right hand side of Equation 2.7b shows that the deprotection slope benefits from a large acid slope early in the reaction diffusion process. The second term, however, indicates that extra acid at the line edge degrades the slope as the deprotection gradient is built. Intuitively, this is due to saturation of deprotection: the deprotection rate in the highly exposed region of the resist slows as the number of protecting groups is reduced. If the amount of acid at the line edge is high, the result is that the deprotection in the ideally unexposed region of the resist will begin to catch up to that in the highly exposed region. This in turn reduces the deprotection slope at the line edge. In the NPDB resist, the rate of acid slope increase is reduced as the PAG saturates, and the negative impact of extra acid at the line edge takes over, ultimately reducing the deprotection slope.

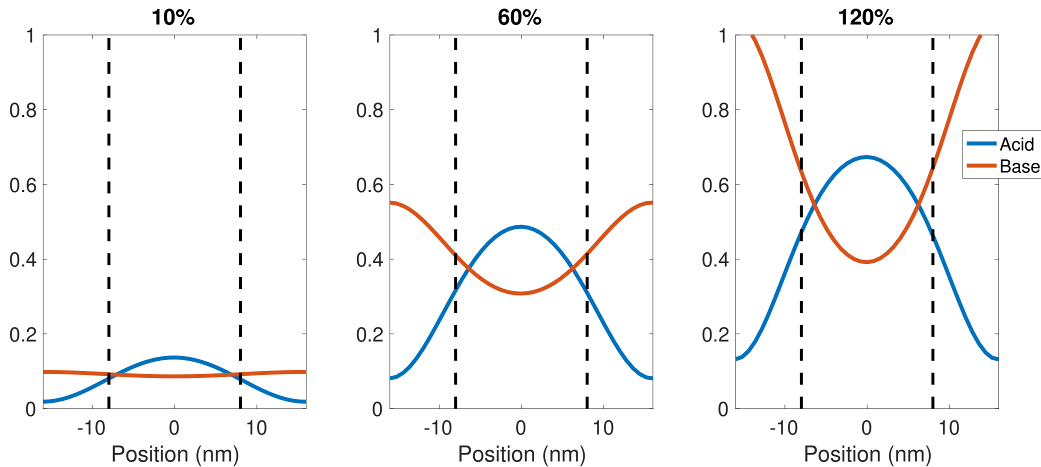

Figure 2.13: PDB Acid Profiles.

In contrast, the slope for PDB and PSCAR improves as more base is added to the resist. Figure 2.13 shows the acid profile at three different base loadings of PDB. These profiles suggest two advantages for PDB over NPDB. The first is that, because the dose at a particular base loading is less in PDB than NPDB, the PAG stays far from saturation. The second is that both the base and acid profiles are sloped. With the simplified assumption that the net acid is simply acid minus base, this represents an increase in chemical slope as indicated in Figure 2.14. These improvements in the initial chemical image propagate through the bake to yield an improvement in deprotection slope. Finally, as compared to PDB, PSCAR 2.0 shows the best deprotection slopes of the three. In essence, this is due to

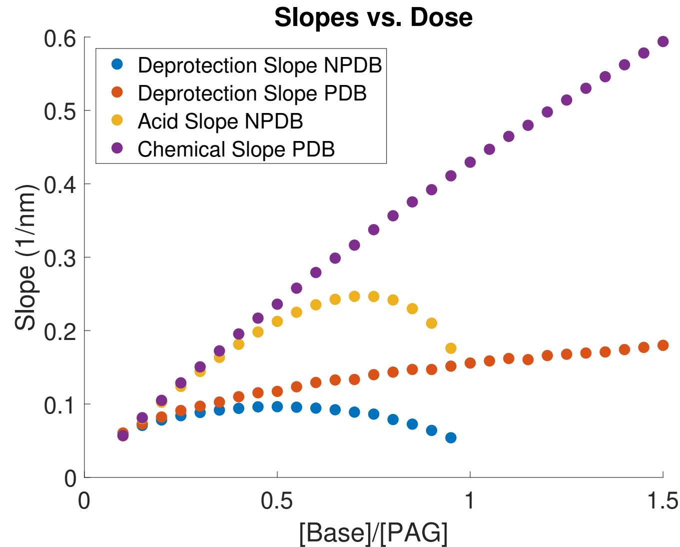

Figure 2.14: PDB Slope vs Dose.

the acid-base annihilation reaction that takes place at room temperature coupled with the ability to generate more acid and decompose more base during the UV sensitization step as described in Section 2.2.1.3. This combination of events produces a ravine in which the acid can diffuse and deprotect the polymer during PEB as illustrated in the third panel of Figure 2.4. This improvement in slope is dramatic enough to almost exactly cancel the impact of additional deprotection noise as compared to the PDB resist.

2.3.4 RLS Tradeoff

What do these results mean for the RLS tradeoff? While the sensitivity and LWR are straightforward to characterize, resist resolution is a somewhat more subjective metric of resist performance. Typical metrics such as correlation length do not capture the anisotropy of the deprotection process introduced by having both acid and quencher gradients. However, the deprotection slope captures the distance over which the resist is switched from developable to undevelopable and vice versa. The shorter this distance, the greater the number of lines and spaces can be packed per unit length. Thus, 1/slope can be used as a metric for the resolution of the resist. With this definition, Z factors defined by $Resolution^3 * LWR^2 * Sensitivity$ were calculated and plotted as a function of base loading in Figure 2.15. While PSCAR 2.0 shows no improvement over PDB in terms of LWR at a given dose, the improvement in deprotection slope suggests that the resolution of PSCAR 2.0 may exceed that of more conventional resist systems. Moreover, the RLS trade-off suggests that this “extra” resolution may be traded in to yield better sensitivity or LWR. However, this is dependent on how the chemical blurs used in this simulation compare to the optimal

blur for each resist formulation[41].

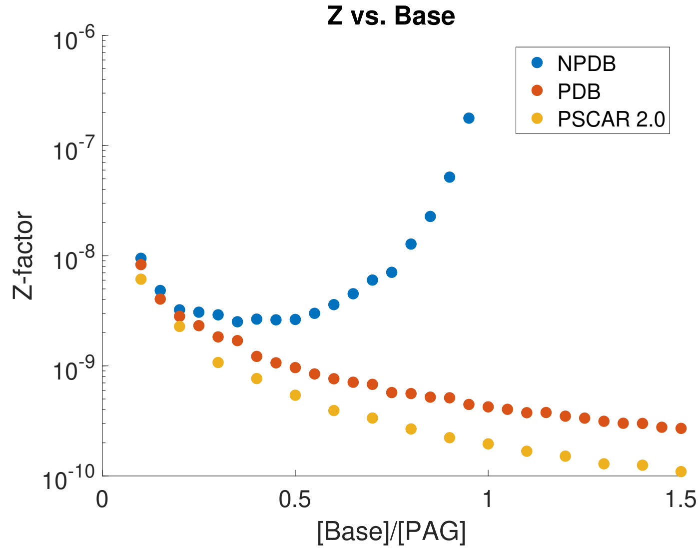

Figure 2.15: Z factor ($R^3 * (LWR)^2 * S$).

2.3.5 Conclusion

The LWR/sensitivity trade-off for three resist systems as a function of base loading is analyzed using the MPPM. The trends are analyzed in terms of the effect of base on the deprotection noise and slope, having shown that the quotient of these parameters yields the simulated LER. For PDB systems it can be shown that the system suffers from increased noise due to additional emphasis being placed on the initial photon distribution. However, an improvement in deprotection slope leads to an overall improvement in LWR for PDB as compared to conventional base. PSCAR 2.0 continues this trend, placing even more emphasis on the initial photons but further improving the slope. The simulations indicate that PSCAR 2.0 shows similar LWR performance at a given dose to PDB, with both representing $\approx$ 20% improvement in LWR at 40 mJ/cm^2. That being said, with deprotection slope as the metric for resolution, this work suggests PSCAR 2.0 to be the best performing of the three resists studied in terms the RLS trade-off, with best-case Z factors improved by a factor of three relative to PDB. Ultimately, this work demonstrates the importance of the non-stochastic deprotection slope in mitigating the effect of chemical and photon shot noise, and suggests deprotection slope optimization as a strategy to beat the RLS trade-off.

2.4 Modeling in 3D

In the previous study, a 2D version of the MPPM was used. However, as the resist is of course fundamentally a 3D object, some phenomena may not be captured by collapsing away the "z" dimension of the resist. In order to better understand the role that the third dimension may be playing, the MPPM was expanded from 2D to 3D. This expansion represents a challenging computational hurdle, in particular because of the need to simulate large numbers of lithographic features in order to get statistics on rare stochastic events. As as example, the aerial image shown in Figure 2.16 represents an array of contact hole features, which are used to pattern metal pillars that electrically connect different layers of an integrated circuit. This aerial image is comprised of 1280×1280 pixels, 0.4 nm per side, to build a 15×15 array of 16 nm contacts. If the model is used to track three species- acid, quencher, and deprotection - then $1280 \times 1280 \times 3 \approx 4.9 \times 10^6$ floating point numbers must be tracked during the simulation, for a total of 20 MB of data at single precision.

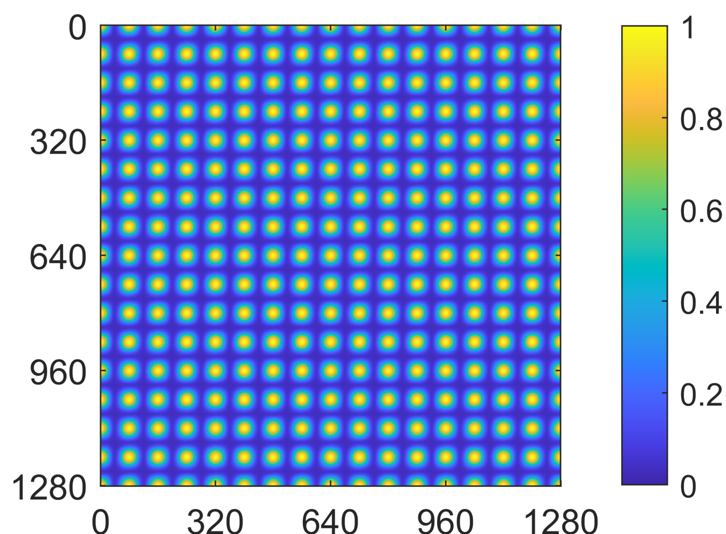

Figure 2.16: Aerial image comprised of a 15×15 array of 16 nm contacts. Pixels are 0.4 nm per side.

In the 3D model, on the other hand, if the resist is 35 nm thick, then an additional factor of 88 voxels at a side length of 0.4 nm are needed to represent the same domain, bringing the totals to $1280 \times 1280 \times 88 \times 3 \approx 430 \times 10^6$ floating point numbers and 1.7 GB worth of data. This doesn't count the memory required to store temporary arrays during the reaction-diffusion simulation. This large increase in data coincides with a large increase in the number of computations required on the 3D grid, and thus an increase in model runtime.

The most computationally expensive part of the model is the reaction-diffusion simulation, in which the right hand side of Equation 2.2 must be evaluated for each voxel and species every time step. Fortunately, the nature of these equations lends itself to parallel

computation, as, for a given time step, the time derivative of each voxel can be evaluated independently. To take advantage of this situation, the 3D MPPM is written as a C program. Added to the code is a series of OpenAcc "pragmas." These lines of code are effectively comments which, at compile time, can instruct the compiler on how to build the code. In particular, OpenACC pragmas allow for normal C code to compiled to run on GPU accelerators. The result is code that is able to perform the reaction diffusion simulation more than order of magnitude faster than a corresponding serial code, enabling full 3D modeling studies to be conducted at scales where stochastic effects can be studied. Several examples of how the 3D model can be employed are discussed below.

2.5 Study - Modeling Anisotropic Blur and Missing contacts

As a test case for the 3D, the impact of acid z blur, or acid diffusion perpendicular to the wafer, on contact uniformity is studied. Previous work using analytic models suggests that increased z blur should yield a resist performance improvement[13]. While the present study represents a thought experiment, it's plausibility is rooted in previous photoresist studies. For example, Cheng et al. were able to show that pattern profiles could be improved by application of low frequency AC electric fields during PEB,[8] while Yuan found that numerical resist models best matched experimental data when the deprotection chemistry locally altered acid and quencher diffusion constants.[46] While these effects have origins physically distinct than those studied here (namely, they represent an additional advection term in what is otherwise a reaction-diffusion process), the observation of these effects lends credence to the possible presence of anisotropies in the patterning process that could be exploited in future resist materials. One such chemistry is the use of polymer brush-like materials, where the polymer structure itself contains anisotropies that may induce directional acid diffusion. It is further worth noting that advection can be explicitly included in the model, and that directionally-dependent diffusion merely represents a starting place for 3D investigations.

2.5.1 Model Parameters

For the simulation, the resist model specified in Table 2.2 is used. For the baseline study, the x-y blur is held constant at 12 nm, while varying the z blur across a range of values. For each z blur, a minimum of 10^5 contacts was simulated. A graphical understanding of the impact of the differing z blur conditions can be gained from the first row of Figure 2.19, which illustrates the acid PSF in the absence of quenching effects.

At the x and y boundaries of the model periodic conditions are assumed, while no flux boundary conditions are used in the z dimension. With these conditions, acid and quencher counts in the model domain would be conserved if not for the quenching reaction. To avoid nonphysical correlations between exposure events at the x-y extremes of the model domain, the half-contacts that comprise the boundary of the aerial image shown in Figure 2.16 are

discarded and not used in the final analysis. This was performed out of an abundance of caution due to the rarity of the failed contact phenomena being studied; correlations would be minimal regardless due to the x-y acid blur being about 1/3 of the pattern pitch.

Parameter	Value
CD / pitch	16 / 32 nm
resist thickness	35 nm
voxel size	$0.4 \times 0.4 \times 0.4\text{nm}^3$
dose (peak at wafer)	30 mJ/cm^2
absorptivity	4 µm^{-1}
PAG concentration	0.2 nm^{-3}
Base concentration	0.085 nm^{-3}
QE	3
acid blur (x, y, z)	$(12, 12, [2, 6, 12, 24])$nm
base blur (x, y, z)	$(5, 5, 5)$nm
deprotection rate	1 nm^3/s
quenching rate	10 nm^3/s

Table 2.2: Resist model parameters

To extract a CD distribution from the 3D model, two methods were evaluated. In the first, referred to as "volume-averaging," the total volume of cleared voxels in the domain of the contact is summed using a threshold deprotection model. The threshold was set to a deprotection fraction of 0.27. Then, assuming the contact is a cylinder, this volume is converted to a CD using the formula $CD = 2\sqrt{V/(\pi h)}$. This method is in essence performing a sort of z-averaging of the contact CD. In the second method, the minimum area open from top to bottom of a contact is instead considered. This analysis consists of summing the area of "cleared" pixels, where a pixel is clear if the contact is deprotected in a straight line in z from the top of the resist down to the substrate. Then an effective CD is computed using $CD = 2\sqrt{A/\pi}$. Simple cartoons of the two cases can be found in Figure 2.17.

While both analysis methods have some merit, method 2 was deemed to be closer to what actually matters for lithographic processes, as only this method can account for so called road blocks preventing a contact from opening. However, it provides an overly pessimistic view of contact size and uniformity. In particular, a real developer is capable of punching through small regions of undeveloped resist, as there is always some dark loss associated with the development process. To describe this phenomena, a dissolution model is developed to accompany the MPPM.

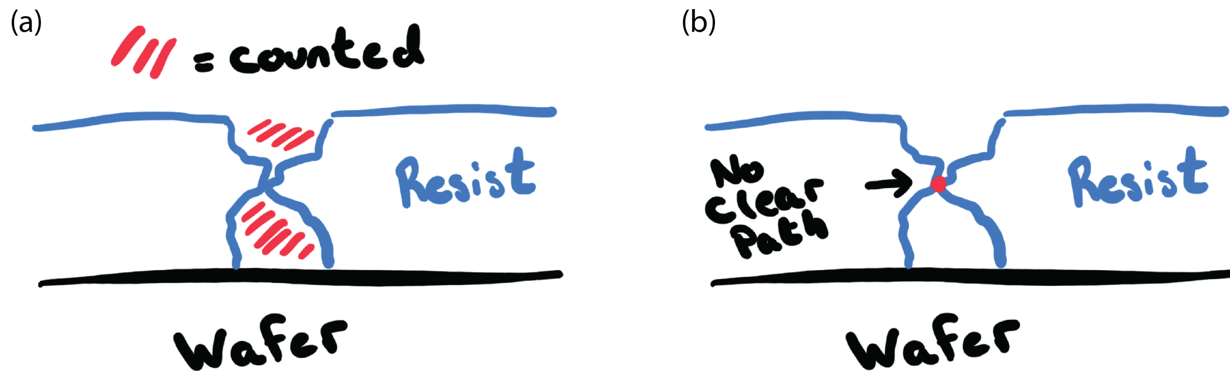

Figure 2.17: Schematics of the analysis methods. (a) The volume averaging method. Note that volume above and below the blockage is counted. (b) Minimum area method. The blockage sets the CD to zero.

2.5.1.1 Dissolution Model

As illustrated by the discrepancy between the analysis methods illustrated above, the investigation forced engagement with the subtleties of interpreting the 3D model results. Part of the solution was to look at the impact of a realistic vs threshold dissolution model on the critical dimension analysis. To that end, a dissolution model was developed based upon the fast marching level set algorithm[35]. This model propagates the dissolution front through the photoresist material using a a development front speed map. The speed map can be determined by combining experimentally measured parameters with the original Mack development model[27]. The model was implemented in C++, and runs fast enough that it does not add significantly to the overall run time of the MPPM model.

In modeling the develop, the maximum and minimum develop rates were chosen in accordance with experimental results [42], and the threshold in the Mack model chosen such that the develop rate at a deprotection fraction of 0.27 was 35 nm/30 s. Develop parameters can be found in Table 2.3 and the corresponding dissolution rate curve in Figure 2.18. At this develop speed an entire stack of voxels at the 0.27 threshold is cleared during the develop time. With this construct, the region below the red dashed line and to the left of the black dashed line represents the voxels that could change from blocked in the threshold model to cleared after applying the realistic develop model. Following the develop simulation, analysis method 2 above was performed to get a new value for the contact CD.

2.5.1.2 Etch/Metrology

As a final step, the impact of etch or SEM metrology on the conclusions about z acid diffusion was considered. In particular, small regions of resist material may be effectively invisible to the etch or the electron beam used to measure these materials. To simulate this effect, a

Parameter	Value
r_{max}	200 nm/s
r_{min}	0.02 nm/s
n	10

Table 2.3: Develop model parameters

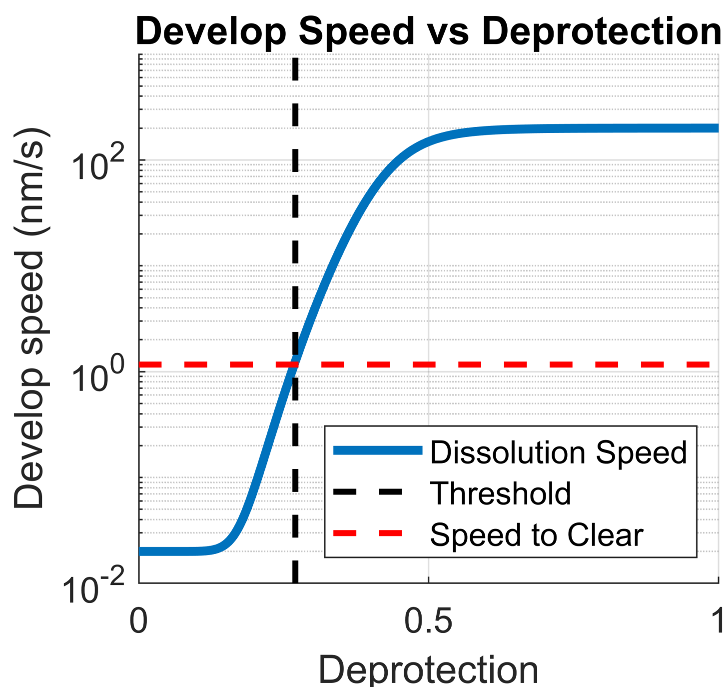

Figure 2.18: Develop speed vs deprotection corresponding to the Mack model with parameters given in Table 2.3.

simple thresholding of the developed resist images was conducted by first creating a 2D x-y map in which each pixel represents the number of undeveloped voxels in the z stack. The chosen threshold then corresponds to thickness of resist removed by the etch or invisible to the SEM electron beam. This thresholding implicitly assumes the etchant or electrons are coming from a single direction, and that thus these are perfectly anisotropic processes in the z dimension. Note that a threshold of 0 corresponds infinite etch selectivity or total electron beam opacity, and is equivalent to analysis method 2.

2.5.2 Results

2.5.2.1 Threshold Develop

Figure 2.19 shows the qualitative results for the same seed (same initial conditions) under three different acid blur conditions. The opaque surface illustrates the contour of the contact at a deprotection threshold of 0.27. As is apparent from these illustrations, the increased z blur yields a contact that is smoother in z, and perhaps somewhat narrower in x and y. When viewed from the top, the difference is even more stark, as only the contact with the increased z blur has a sizeable clear path from the top to the bottom of the contact.

The entire set of contacts was analyzed via the two methods laid out in Section 2.5.1. Figure 2.20a shows the results obtained via the volume-average method, and Figure 2.20b shows the results when analyzed via the minimum CD. It is clear these two methods yield very different results. When the volume average method is utilized, it is seen that, if anything, the contacts are smaller with a wider distribution as the z-blur is increased, contrary to the intuition that increased z blur should yield a more uniform distribution. In contrast, the minimum clear CD method yields quite the opposite result, where the larger z blur yields a larger mean CD as well as a narrower distribution. The schematic shown in Figure 2.17 is helpful for understanding the difference; in essence, the volume average-method is ambivalent to the presence of closed regions of the contact. The lost volume from a few closed z slices can be made up for using volume from wider deprotected slices elsewhere in the feature. In contrast, the minimum CD method assumes that a z slice below threshold, or a few slices that are open but misaligned in z, result in a closed contact. Since it is believed that so called "road blocks" do stop the develop process, the minimum-CD analysis is probably closer to reality than the volume-averaged method. That being said, this method provides an overly pessimistic view of missing contact counts; the develop is not a perfect switch that changes at a given threshold, but has some minimum develop rate that eats at resist material even below the deprotection threshold. In the next section, the impact of one set of develop parameters on the analysis of the role of z blur is examined.

2.5.2.2 Develop Model

The develop process was modeled using the method described in Section 2.5.1.1. For the sake of comparison, the resulting contact contour for the 6 nm blur case is shown in Figure 2.21 which can be directly compared to the middle column of Figure 2.19. The develop has served to expand the contact in the x-y plane relative to the threshold develop model, and, from the aerial view, it can be seen that it has punched through small blockages at the bottom and on the sides of the contact. The impact of these changes can be found in Figure 2.22, which shows that the develop has served to increase the mean CD of all the z blur cases examined, as well as to narrow the distributions. While somewhat less dramatic than the threshold develop case, the conclusion still holds that increased z blur increases the CD and results in a narrower distribution of CD.

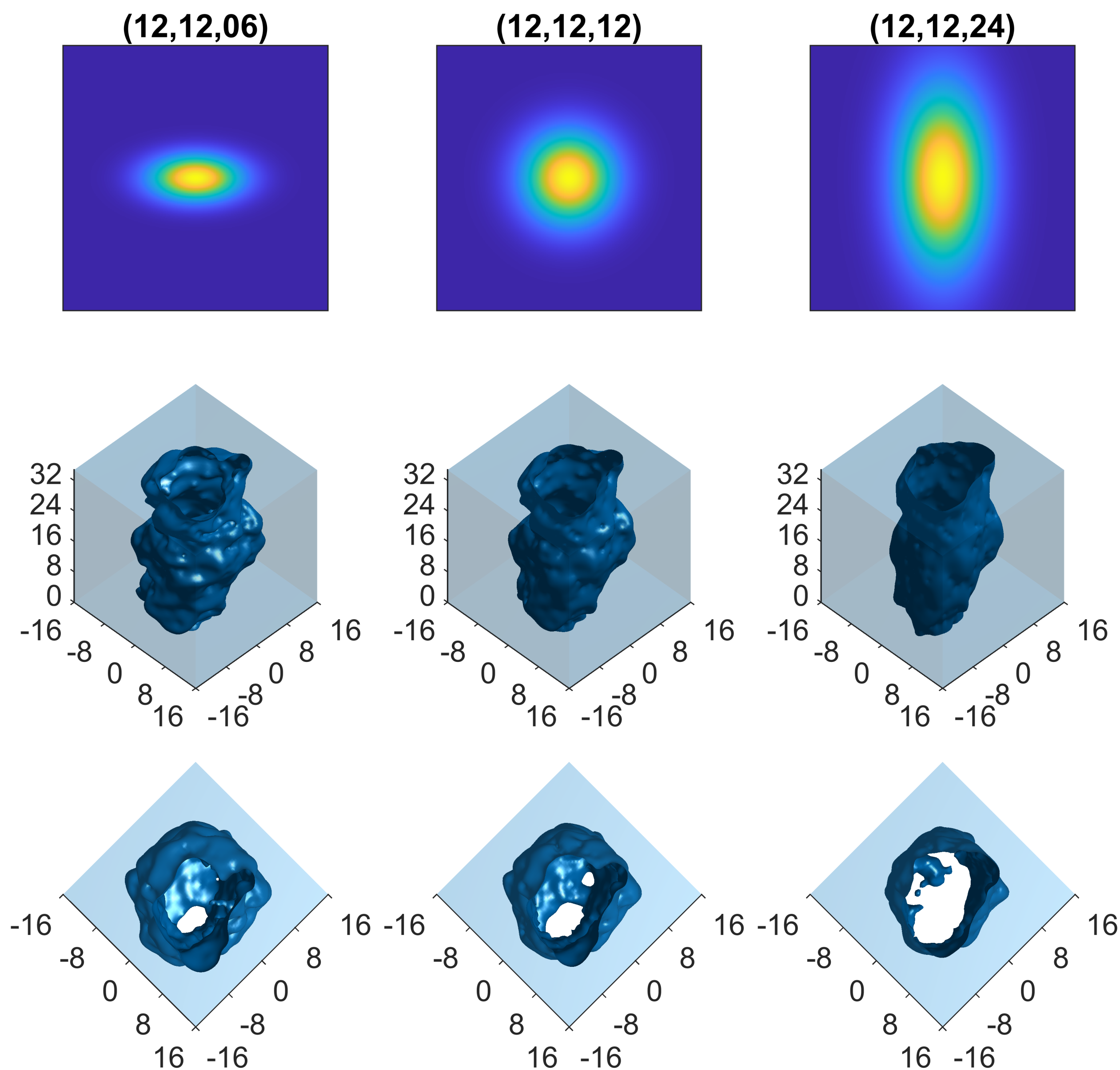

Figure 2.19: Acid PSF and corresponding contact contours. Rows correspond to the x-z plane of the blur function, a side profile, and an aerial view of the resulting contact, respectively. Columns correspond to z blur values of 6, 12, and 24 nm, respectively, with x-y blur held constant at 12. As z blur increases, contact edges become smoother, and the path to from top to bottom becomes clearer.

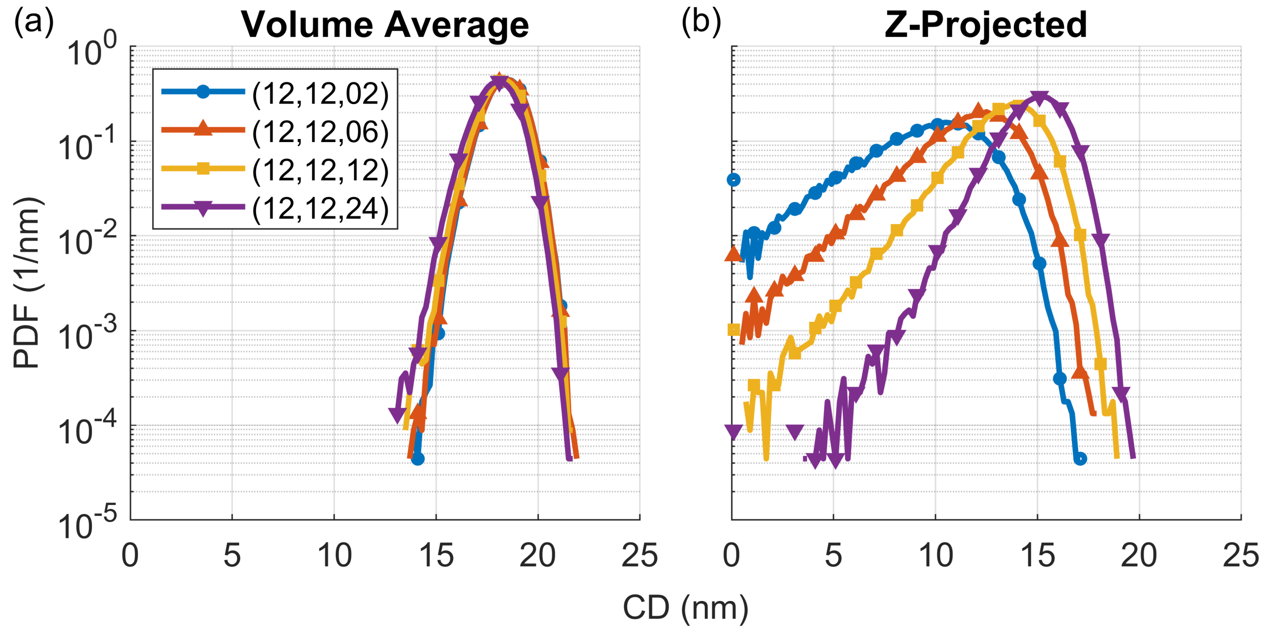

Figure 2.20: CD histograms produced by the (a) volume average and (b) z-projected minimum CD methods.

2.5.2.3 Exposure Latitude and CD Biasing

Figure 2.22 shows that changing z blur has the effect of biasing the mean contact CD. To use the line of thinking presented by Naulleau[31], one may wonder whether the improvement in CD distribution arises from an increase in acid amplification due to increased z diffusion. This increased amplification could bias the mean CD away from the non-linear dose response of the resist, which would in turn mitigate the skew of the CD distribution. To test this theory, the exposure latitude of the resist was simulated by running 225 contacts at a range of doses and then employing the develop model and analysis to extract the CD. It is important to note that, using this analysis, the stochastics play a key role in determining the average CD, as the interaction between individual z slices is non-linear. The resulting dose vs CD plot is shown in Figure 2.23(a). As expected based on the histograms, the exposure latitude curves reveal an increase in the mean contact CD at a given dose due to increased z blur, and that the mean CD has been biased somewhat relative to the non-linear response of the resist.

To test whether this bias is at the root of the improved contact uniformity with increased z blur, an additional 10^5 contacts were simulated at the smallest and largest z blurs, re-biasing the mean contact CD to equal the isotropic case by adjusting the dose according to Figure 2.23(b). The resulting histograms can be found in Figure 2.24. It is clear that, despite requiring about 6% less dose, 24 nm of z blur still yields a more uniform contact distribution than the isotropic case, and the opposite is true of the 2 nm z blur case. Thus,

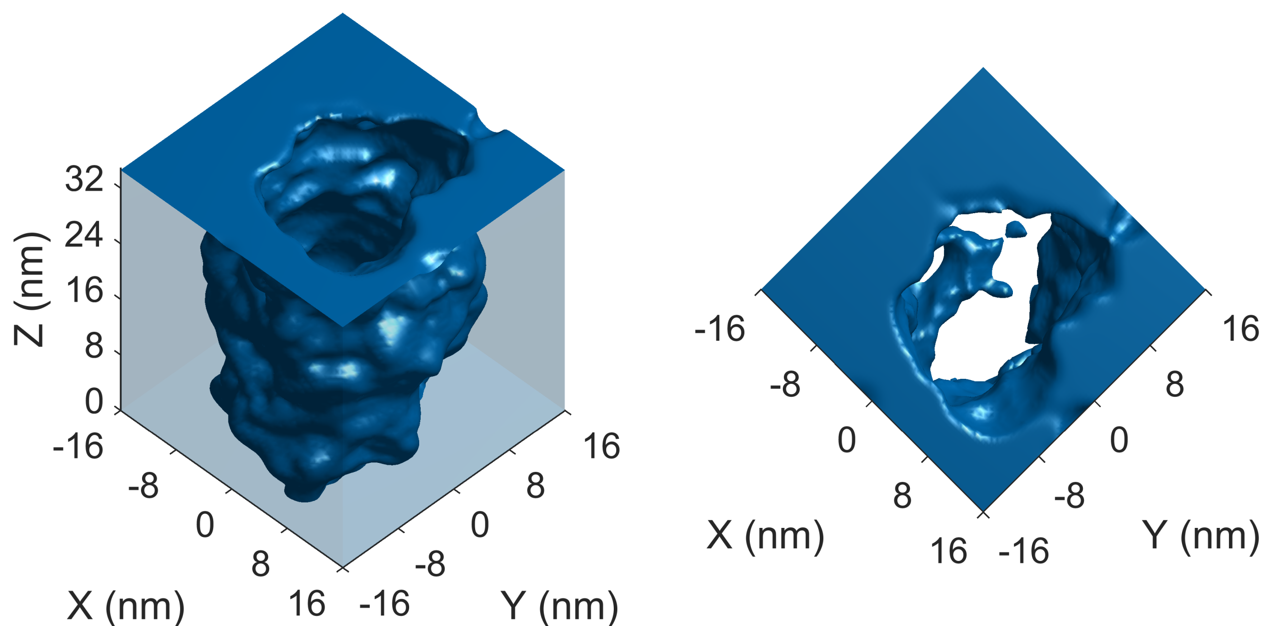

Figure 2.21: Contour of 6 nm z blur contact after develop. This is directly comparable to the threshold develop method used to generate the profiles in the middle column of Figure 2.19.

the improvement in contact uniformity is not simply a result of additional acid amplification and resulting CD bias, but that there is in an additional smoothing effect as well.

2.5.2.4 Larger isotropic blur

As a control, the benefit of increasing z blur was checked against an equal-volume isotropic blur. The larger isotropic blur was generated using the fact that $12 \times 12 \times 24 \approx 15.1^3$. Figure 2.25(a) shows the CD distribution of 10^5 contacts simulated under these new conditions. It is apparent from this plot that a larger isotropic blur has an overall detrimental effect on the resulting patterns, with the average CD subtly reduced, and the CD distribution dramatically broadened relative to the anistropic case. A quick look at the resulting exposure latitude in Figure 2.25(b) shows why: relative to the smaller isotropic blur and increased z blur conditions, the dose response of the larger isotropic blur has a higher-dose corner and overall steeper slope than the previous conditions, as might be expected based on the additional x-y diffusion. Thus, the effective dose noise for the larger isotropic blur case results in a wider and more skewed spread of CDs. It is worth noting that this actually suggests that the larger isotropic blur performs worse in all of the R, L, and S of the RLS trade off as compared to the original blur conditions.

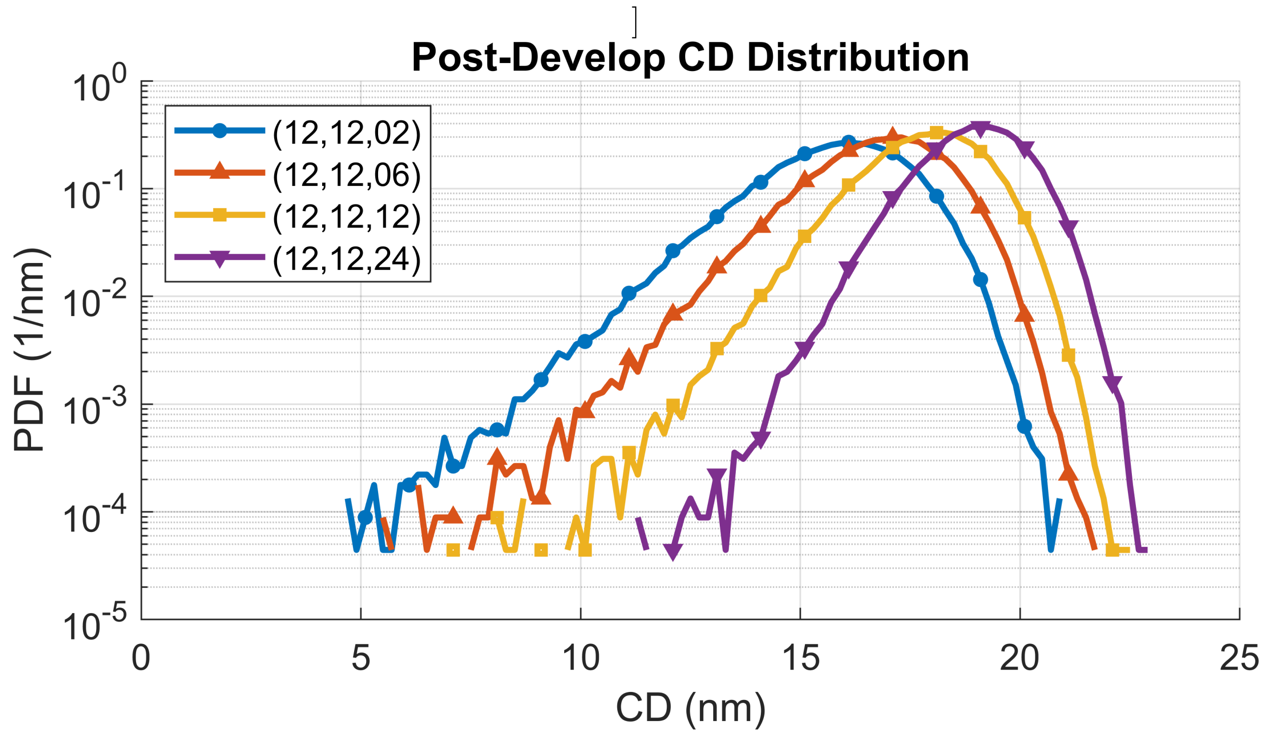

Figure 2.22: Contact CD distribution using the Mack development model.

2.5.2.5 Etch/Metrology Analysis

As a final area of interest, the impact of etch or metrology on the conclusions about z acid blur was investigated. Figure 2.26 shows the qualitative impact of the thresholding process on the 6 nm z blur contact shown elsewhere in this paper while Figure 2.27 shows the resulting histograms assuming the etch/metrology can "see" through various resist thicknesses. Figure 2.27 shows that an increase in the etch/metrology threshold results in an increase in mean CD as well as narrowing of the CD distribution as the amount of invisible resist increases. In addition, the histograms suggest the effect of acid z blur decreases as the tolerance increases; in essence, the more resist the etch or metrology can see through, the more these processes play the z-averaging role. The narrowing of the CD distribution post etch has been reported previously[28], suggesting that the etch can indeed play this averaging role. Furthermore, since pre-etch CD distributions are obtained via SEM metrology, this suggests that etch is more tolerant of small resist blockages than the resist metrology.

To further investigate whether increased z blur still provides benefit when a 5 nm etch is assumed, a new batch of stochastic simulations were performed. First, to counteract the increased average size of the contacts due to the increased etch assumption, the dose was reduced by about 10% to reduce the mean contact size to 18 nm. Second, 3×10^5 additional simulations at each of 2, 12, and 24 nm z blurs were conducted. The resulting histogram can

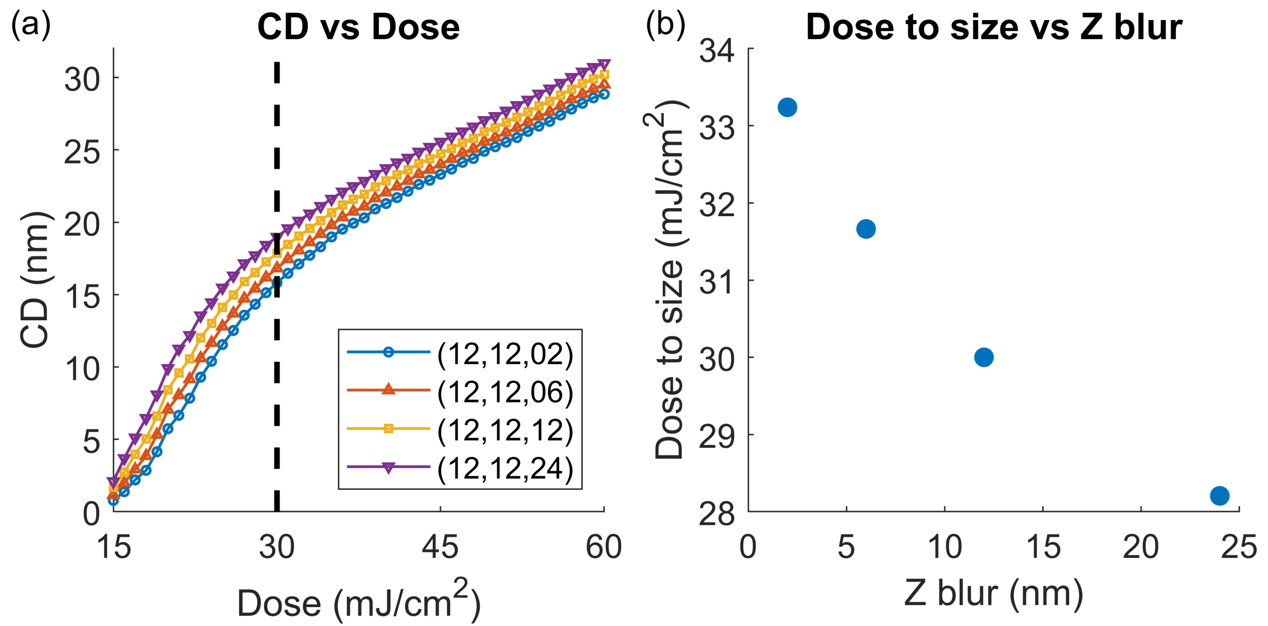

Figure 2.23: (a) CD vs dose response and (b) corresponding dose to size for the different z blur resist models.

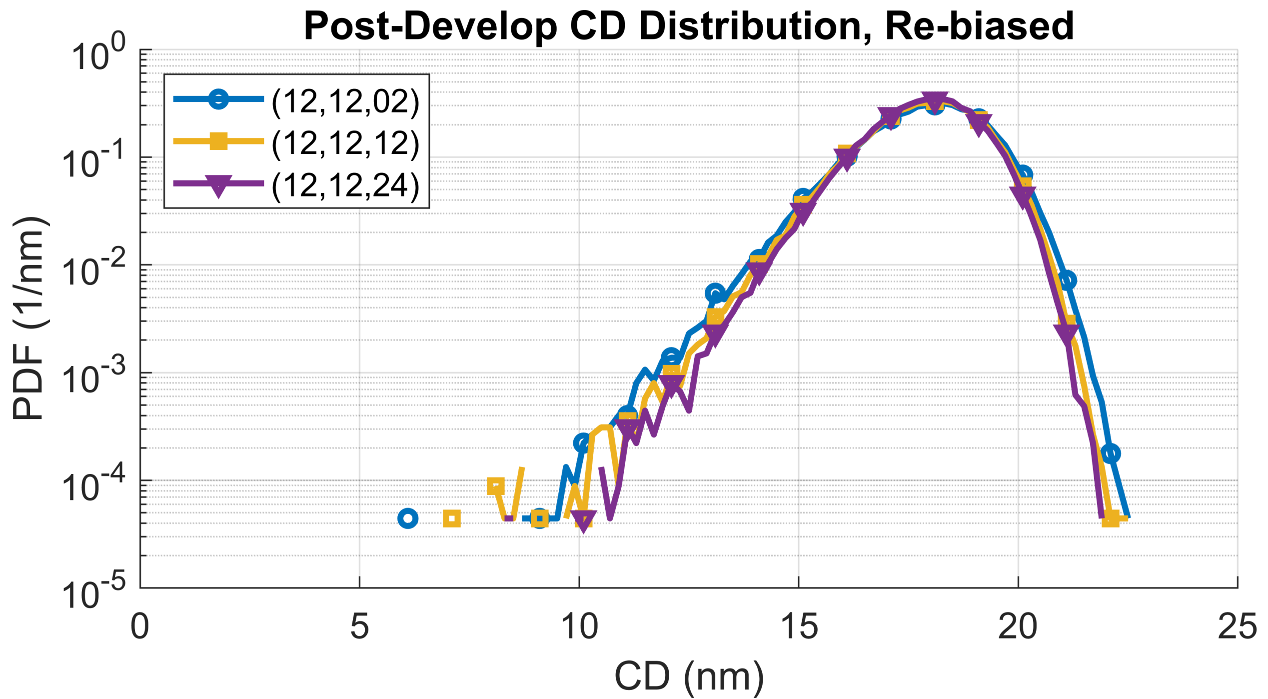

Figure 2.24: Contact CD distribution using develop model after adjusting dose such that all contacts print to the same average size.

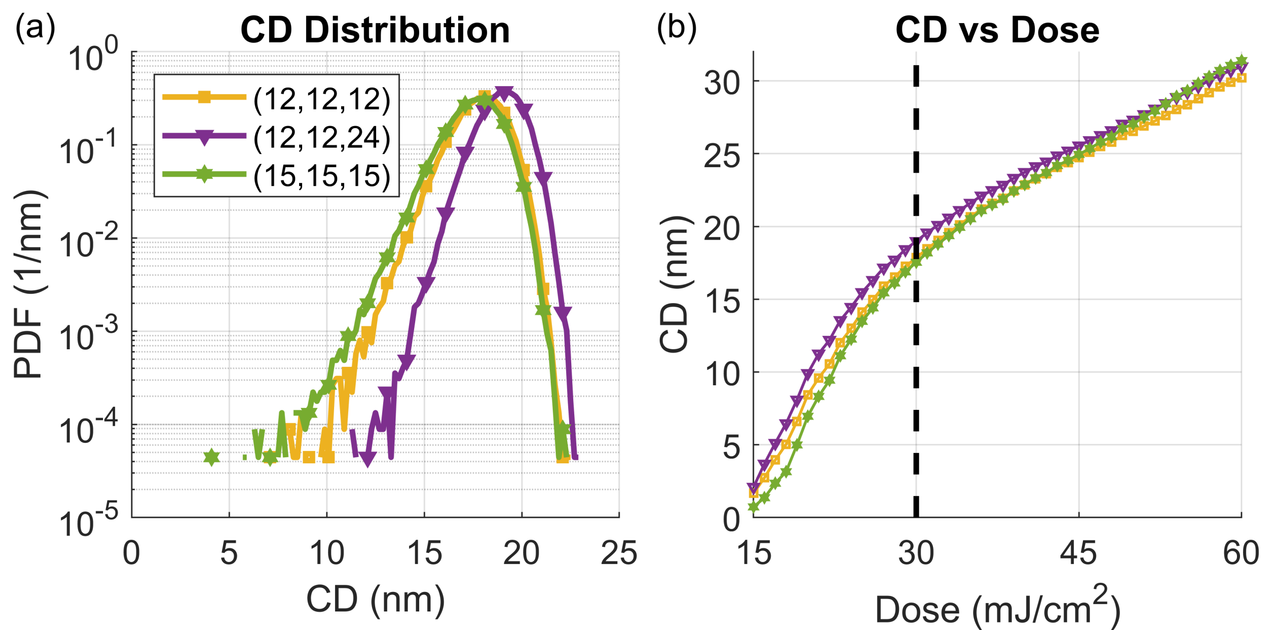

Figure 2.25: Comparison of (a) CD distribution and (b) dose response of the isotropic $(12, 12, 12)$nm, anisotropic $(12, 12, 24)$nm, and isotropic $(15, 15, 15)$nm blurs.

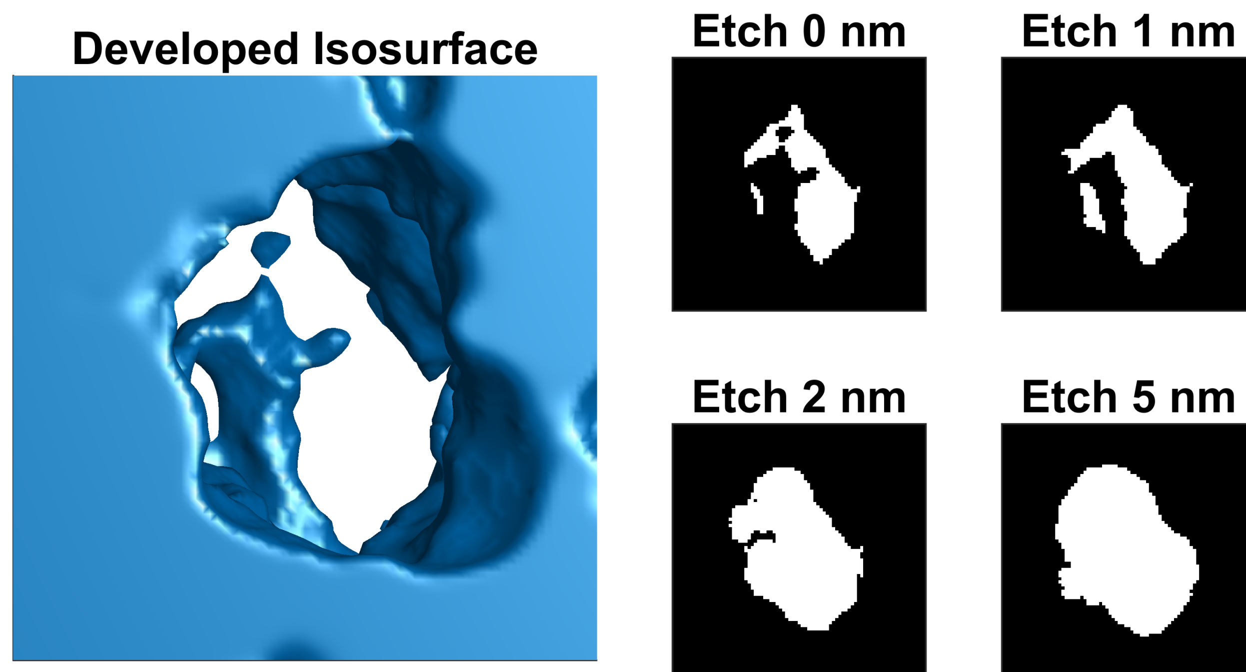

Figure 2.26: Example of the impact of different etch thresholds on the resulting contact shape. The more resist etched, the larger the contact.

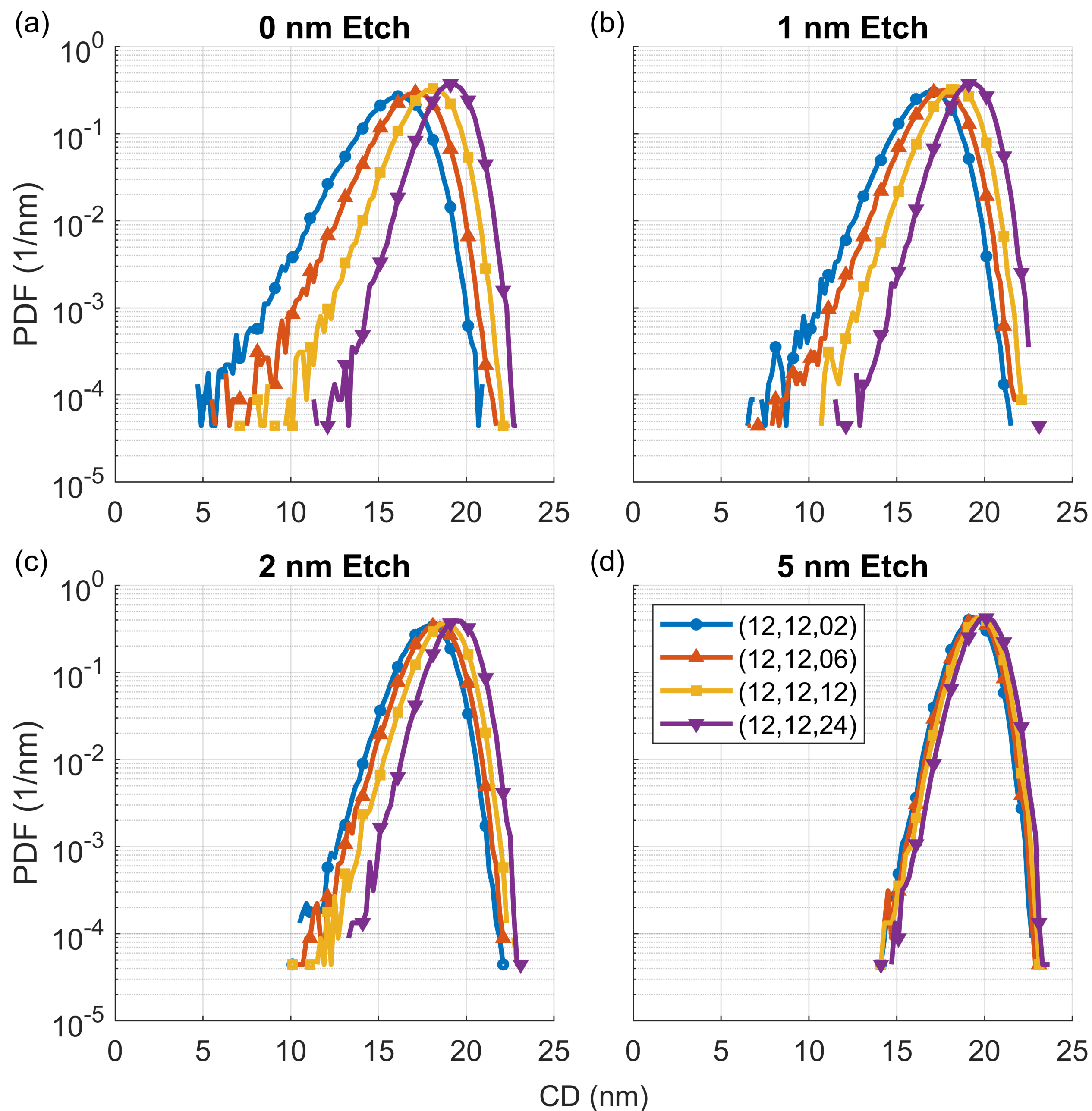

Figure 2.27: Histograms assuming different etch models. (a) Baseline, assuming perfect etch selectivity. (b) Etch 1 nm of resist. (c) Etch 2 nm of resist. (d) Etch 5 nm of resist.

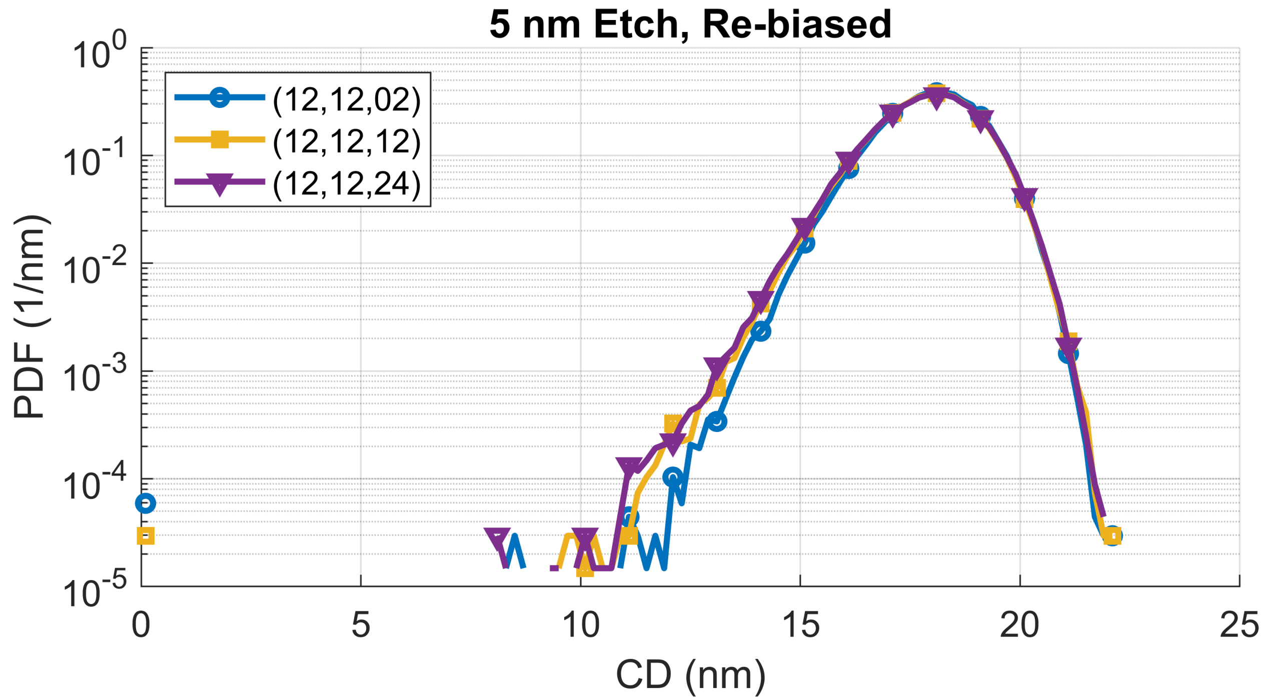

Figure 2.28: Re-biased CD histograms with 5 nm etch assumption. While the increased z blur resist has a wider CD distribution, it also displays 0 missing contacts, unlike the isotropic (2 missing) and 2 nm (4 missing) z blur simulations.

be found in Figure 2.28. Counter-intuitively, the increased z blur case (shown in purple), now displays the widest CD distribution. However, while this would suggest that this blur would result in a higher rate of missing contacts, the opposite is true for this set of simulation data. Despite having the narrowest distribution, the 2 nm z blur simulations yielded 4 missing contacts out of the 3×10^5 simulated, and the isotropic blur simulations yielded 2. The stretched z blur, in spite of its wider CD distribution, yielded 0. Acknowledging that it is difficult to draw firm conclusions based on such small numbers of failures, this result suggests that the CD distribution may not tell the whole story when it comes to predicting missing contacts; in spite of resulting in what appears to be a less favorable CD distribution, increased z blur may help to mitigate the occurrence of missing contacts.

A brief look at the initial acid distribution corresponding to a contact failure at 2 nm of z blur reveals why increased acid diffusion in z may help to avoid missing contacts. As shown in Figure 2.29(b), this particular contact failed to produce a cleared path from the top of the resist to the substrate, leaving about 8 nm of undeveloped material at the bottom that the simple etch model was unable to remedy. Figure 2.29(a) shows a cutline of the initial acid distribution that gave rise to this contact. In this particular failure, above and below the blockage, there was sufficient acid to clear the contact. Had the z blur been greater, it may have been possible to join these two regions, clearing a path for the developer to open

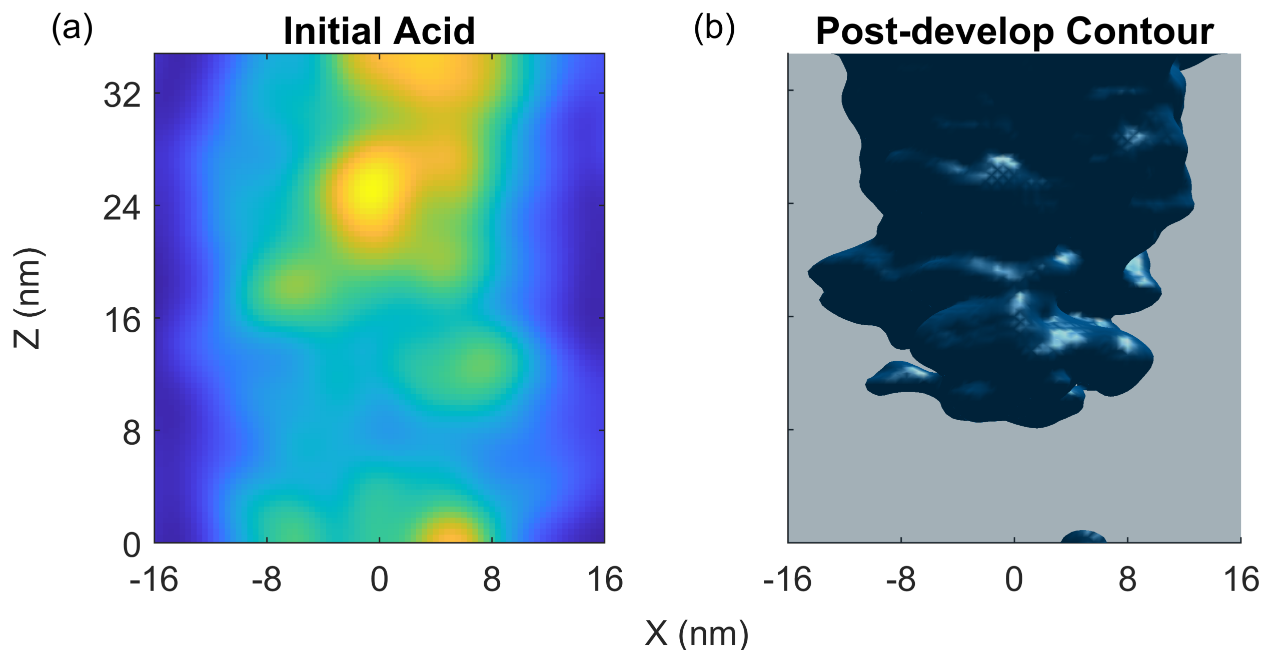

Figure 2.29: Profile of a failed contact. (a) Cutline of initial acid distribution. Two unconnected regions of high acid concentration are separated by the blockage-causing region. (b) Resulting post-develop profile. Bottom 8 nm of undeveloped resist is not clear-able by a 5 nm etch.

the contact.

2.5.3 Conclusion

In this study, the role that the z component of acid diffusion plays in the pattern formation process was examined. In general, it is shown that increased z blur allows for more uniform contacts to be printed at lower dose, a win-win in terms of the RLS tradeoff. It is also shown that these conclusions are highly dependent upon the develop and etch processes with which any resist must be integrated. The developer, having a non-zero minimum develop rate, is capable of removing small blockages within the contact, though at the price of increasing the contact size by eating slowly at the contact walls. Similarly, the etch can play a smoothing role by punching through small regions of undeveloped resist. This work suggests that it is the combination of all three, the resist, etch, and developer, that together must be optimized to achieve desired patterning performance. Furthermore, this required co-optimization highlights the need for improved understanding of the etch and dissolution processes in order to untangle and identify the failure-causing phenomena in the lithography process.

Chapter 3

AFM Metrology

This chapter focuses on the use of atomic force microscopy (AFM), one experimental technique capable of providing the nanometer scale measurements of EUV photoresist. It begins with a brief introduction to the specific AFM modality used to collect data for this thesis before proceeding to several experimental results.

3.1 AFM Basics

AFM is a scanning probe technique in which a micro/nano-fabricated probe and the sample under study are brought into close proximity. By measuring the influence of the tip-surface interaction on the motion of the probe, the technique provides information about the local nature of the sample near the point at which it interacts with the tip. Figure 3.1 shows the basic set up of an AFM experiment. The key feedback provided to the experimentor is provided by a deflection laser focused atop the probe that in turn reflects onto a detection diode. The diode records the position of the laser, which in turn provides a measurement of the position of the cantilever.

For the work presented in this thesis, the AFM was primarily operated in what is known as amplitude modulation (AM) tapping mode. In this mode, the cantilever is driven by a periodic external force which causes the beam to oscillate. As the cantilever forms a sort of spring, when the frequency of the external force nears that of the cantilever's resonant frequency, the result is a boost in the amplitude of the tip oscillation. This can be well understood by using a simple harmonic oscillator model, as shown in Equation 3.1.

$$\ddot{z} + \frac{\omega_0}{Q}\dot{z} + \omega_0^2 z = Ae^{i\omega_D t} \tag{3.1a}$$

$$\omega_0 = \sqrt{\frac{k}{m}} \tag{3.1b}$$

$$Q = \frac{m\omega_0}{\beta} \tag{3.1c}$$

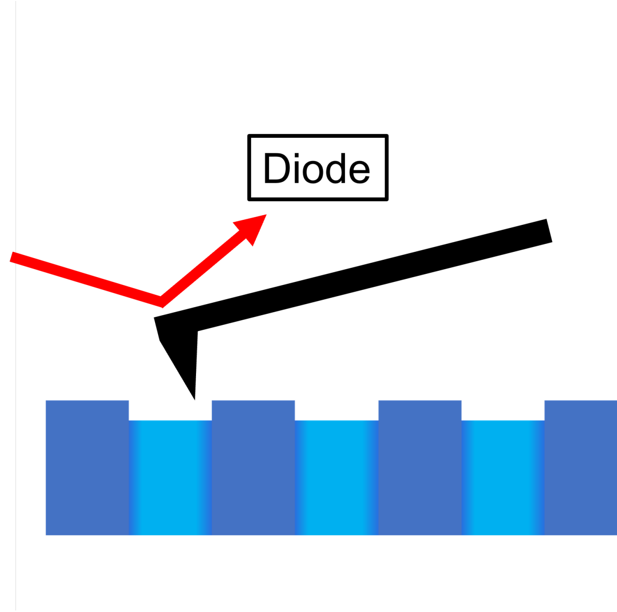

Figure 3.1: Schematic of AFM experiment

In these equations, z represents the position of the tip oscillation, ω_0 represents the resonant frequency of the cantilever, ω_D is the drive frequency, k the spring constant, m the effective mass, and Q the quality factor, ultimately determined by the amount of damping due to viscous drag, β. These equations can be solved using the method of undetermined coefficients, yielding:

$$z(t) = Ce^{i\omega_D t+\phi} \tag{3.2a}$$

$$C = \frac{A}{\omega_0^2}\sqrt{\frac{1}{(1-(\frac{\omega_D}{\omega_0})^2)^2+(\frac{\omega_D}{Q\omega_0})^2}} \tag{3.2b}$$

$$\phi = \arctan(\frac{\frac{\omega_D}{\omega_0}}{1-(\frac{\omega_D}{\omega_0})^2}) \tag{3.2c}$$

This equation assumes that any of the homogeneous transients have decayed due to damping of the oscillator. A plot of the amplitude and phase of the oscillator can be found in Figure 3.2.

The presence of an external force, such as that provided by proximity to a sample, alters the equation of motion shown above. In the limit that the external force is approximately linear around a small displacement in tip-sample distance, Equation 3.1 picks up an extra term that effectively results in a subtle shift in the resonance of the tip. Figure 3.3 shows the change in amplitude and phase coming from a repulsive force (such as that coming from Pauli repulsion at close distances). For a tip driven at the “free” resonant frequency of the

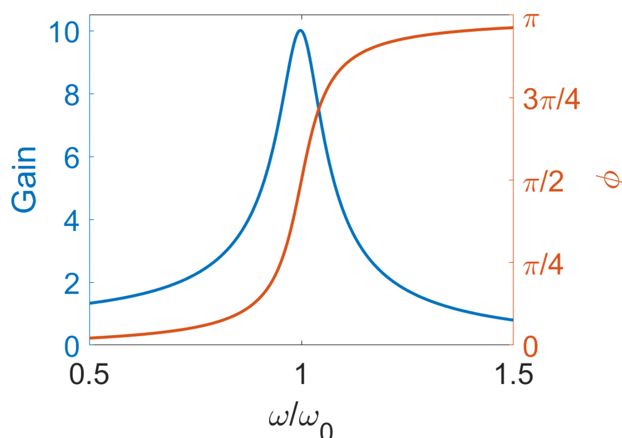

Figure 3.2: The amplitude (blue) and phase (red) of the forced-damped harmonic oscillator near resonance. This is a good model of the motion of the AFM cantilever tip.

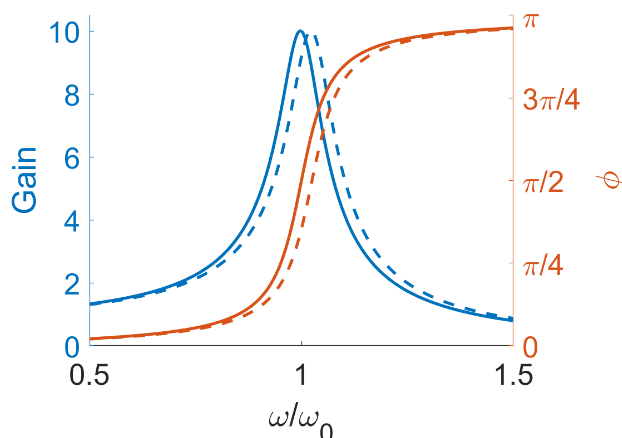

Figure 3.3: The amplitude (blue) and phase (red) of the forced-damped harmonic oscillator near resonance, both for the free cantilever (solid lines), and for the tip in the presence of a repulsive force (dashed).

cantilever, the sample causes a decrease in the tip amplitude, and an oscillation phase offset of less than $\pi/2$.

In AM mode, the frequency and amplitude driving the cantilever oscillation is kept constant throughout imaging. As the tip is scanned over a surface, the subtle changes in tip-sample interaction due to topography or sample composition manifest themselves as changes in oscillation amplitude and phase. However, the system is set to keep the tip amplitude constant. To achieve this, the z distance between the tip and sample is adjusted. By record-

ing the tip-sample distance, as well as the phase and amplitude of the tip oscillation across the sample, a map of the sample topography, tip-sample interaction, and a report on the quality of the image are thus generated. It is this feedback that is used in this thesis to study photoresist materials, measuring the latent image in resist, as well as measuring the dissolution of the photoresist in-situ using a high-speed modality of AM tapping mode.

3.2 Study - Influence of PEB time on latent image

In this study, AFM is used to measure the "latent image," the chemical image in the photoresist produced by exposure and subsequent processing but prior to dissolution.

Adding to the already difficult problem of engineering materials capable of meeting industrial requirements is a lack of metrology at various stages of the photoresist process. Many studies have been performed elucidating the nature of the various reaction-diffusion processes post-exposure, particularly in chemically amplified resist [43] [40] [41] [29]. In particular, these experiments have led to a number of observations regarding the diffusion characteristics of photo acid inside of resists, which, though developed for deep UV resist, provide valuable insight for the EUV regime. However, these experiments in general rely upon dissolution of the photoresist in order to measure the underlying reaction-diffusion processes. This has the effect of washing away the underlying chemistry responsible for production of the final resist structure, mixing the effects exposure and bake chemistry with that of the dissolution process. While the final structure is of course most relevant to subsequent manufacturing steps, understanding the intermediate steps that generate stochastic defects is key for manufacturing photoresist ready for use in future lithographic nodes.

To that end, this study explores the use of atomic force microscopy for measuring the latent image in photoresist, with an emphasis on measuring critical dimension (CD), line width roughness (LWR), and edge roughness correlation length (L_c) at the latent stage. A similar experiment was done more than ten years ago[44], though seemingly little has happened in the way of AFM latent image metrology since. Though this study focuses on CAR resist, it is applicable to other resist chemistry, as evidenced by a demonstration of its applicability to a metal oxide resist.

3.2.1 Methods

The general methodology of the experiment presented here is shown in Figure 3.4. The photoresist was spun onto a standard silicon wafer. The resist was then exposed using electron beam lithography, which was used to draw a line/space pattern. A post exposure bake was performed for variety of times ranging from 6 to 120 s, after which the samples were imaged using AFM. In this study, photoresist shrinkage due to radiation-induced chemistry was used as proxy for the underlying dissolution switch caused by exposure and bake. Once an image was collected the resist was developed and imaged using scanning electron microscopy

(SEM), for comparison with the AFM images. More detailed information can be found in the following subsections.

3.2.1.1 Resist Details

The photoresist used in this study was a commercially-available, high-resolution EUV chemically amplified resist (CAR). The resist was about 26 nm thick, with an EUV dose to clear of approximately 12 mJ/cm^2. The process of record bake for this resist is 60 s at 110 C. For this experiment, the resist was also baked at 6, 11, 16, 30, 45, and 120 s. The resist was developed via a standard 2.3 % TMAH puddle method, followed by a 30 s rinse in deionized water.

3.2.1.2 Exposure Conditions

Due to the flexibility in exposure pattern, electron beam lithography was used to expose resist samples. A line/space pattern was drawn at an exposed width of 24 nm and a 100 nm pitch, with the large bias introduced to allow for growth of the line due to electron beam tails, electron backscatter, and acid diffusion. The exposure dose at 100 keV was 500 µC cm^{-2}, which corresponds to an EUV exposure dose of approximately 40 mJ/cm^2

3.2.1.3 AFM Instrumentation

The AFM used for this experiment was the Cypher VRS from Asylum Research. The AFM is located at the Molecular Foundry at Lawrence Berkeley National Lab. Experiments were conducted in tapping mode. In this mode, the tip is driven by a sinusoidal force at the resonant frequency of the cantilever. As the tip is scanned, interactions with the sample will introduce a new force acting upon the tip, thereby changing the amplitude of tip oscillation. The feedback electronics of the AFM were set up such that the tip amplitude was maintained at a constant value, which is achieved by adjusting the tip-sample distance as a function of position on the sample. In this way, a topographic map of the sample is built, which can be used as a proxy for the underlying chemistry in the resist.

A key component of any AFM experiment is the tip. In this experiment, the Tap150AI-G soft tapping probe from Budget Sensors was used. While the tip radius can vary somewhat, the company guarantees a tip radius $\leq$ 10 nm, which determines the lateral resolution of the AFM measurement. In order to keep the tip geometry from changing during imaging, the tip was cleaned via oxygen plasma, thereby increasing the hydrophilicity of the tip. Furthermore, the tip-sample interaction was kept in the attractive regime, in which the tip hovers just above the sample at its closest approach. In this way, undesirable contamination from polymer sticking to the tip was minimized.

3.2.1.4 SEM

After development, the structures were imaged using SEM. The accelerating voltage was set to 2 keV. Pixel averaging was employed to reduce SEM noise and achieve quality images. However, as this thin polymer resist is susceptible to SEM damage, assessment of focus conditions was challenging, and may have impacted the final SEM analysis.

3.2.1.5 Image Analysis

Image analysis of both AFM and SEM images was conducted via SuMMIT [36]. For the AFM images, a global height scale was used to assess line metrics as a function of bake time, with the underlying assumption being that the photoresist shrinkage is an absolute measure of underlying chemistry.

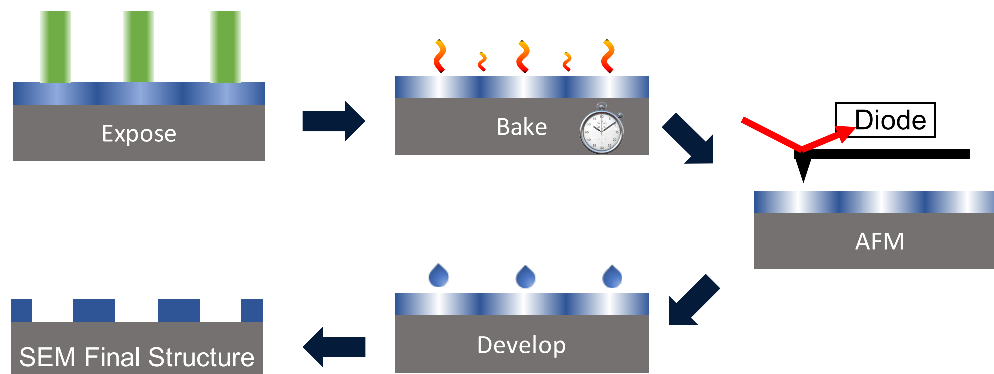

Figure 3.4: Schematic of the conducted experiment. Photoresist was exposed via electron beam lithography, baked for a variety of times, measured via AFM, developed, and then measured via SEM.

3.2.2 Results and Discussion

3.2.2.1 AFM Resolution

In atomic force microscopy, the achievable resolution is set by the radius of the scanning probe. Based on the specifications of the cantilevers used in this experiment, a resolution of less than 10 nm was expected. In order to assess what was actually achieved, an image of the unexposed photo resist was taken, shown in Figure 3.5. This image represents a random rough surface, with correlation induced by the intrinsic nature of the photoresist material and by the finite size of the tip. The resolution of the imaging technique can then be upper bounded by the correlation length of the image, calculated as the $1/e$ point of the autocovariance of the image. The radially-averaged autocovariance function of the

image is found in Figure 3.6 on a semi-log scale. From this plot, it can be concluded that the correlation length, and thus the resolution of the presented imaging technique is approximately 3.1 nm.

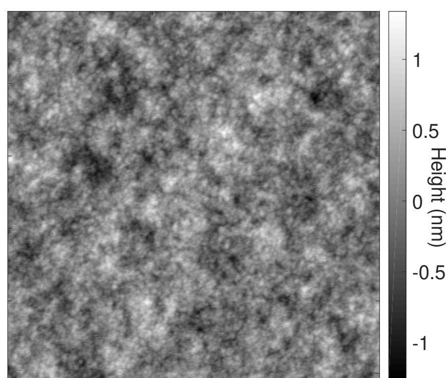

Figure 3.5: Image of unexposed region of photoresist. Each side of the image is 500 nm

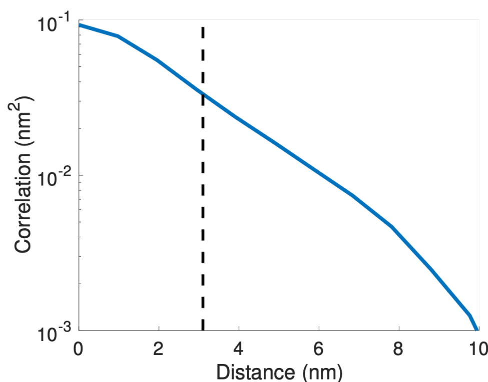

Figure 3.6: Autocovariance function of unexposed resist, on a semi-log y axis.

3.2.2.2 AFM Latent Images

A collection of the latent line-space patterns can be found in Figure 3.7. In order to set the color scale of these images, a global scale was used. To set this scale, a histogram was constructed from each of the images analyzed. This analysis reveals the presence of two distinct peaks, one corresponding to pixels imaged in the unexposed region, and one from the exposed region, with an in-between region representing partially-exposed pixels. Because

AFM only measures relative heights, the average of every line of the image is set to zero. Thus, to compare the images at different bake times, the center of the unexposed peak of each histogram was set to zero height. Following this shift, the color scale of each image was set such that the minimum of the scale was equal to the lowest thickness pixel across all the images, and the maximum to the largest pixel across all the images.

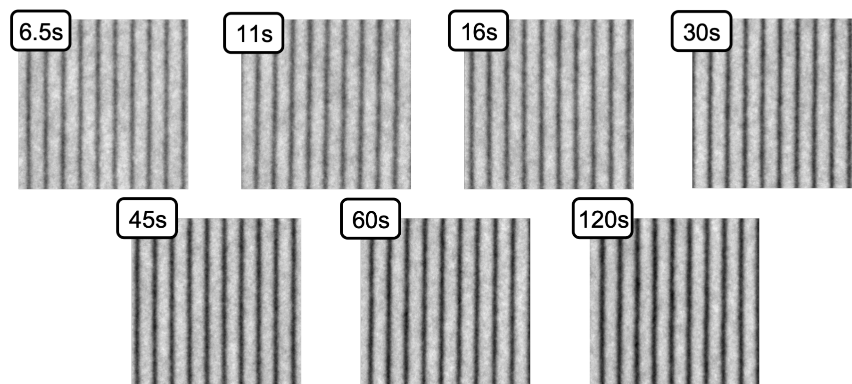

Figure 3.7: AFM line/space latent images for all measured bake times. Contrast improves as the resist is baked due to increased shrinkage.

The shifted and probability normalized histograms can be seen in Figure 3.8. As can be seen from the histograms, as the bake time increases, the thickness of the exposed regions of the resist is reduced, corresponding to increased deprotection in these regions. This manifests as an increase in contrast in the line/space patterns of Figure 3.7. Furthermore, due to the normalization, this implies that the number of unexposed pixels is decreasing as a function bake time. Figure 3.9 plots the critical dimension of the lines as a function of the bake time. This plot shows that the line widths decrease the longer the resist is baked, rapidly at first, and more slowly at longer bake times. This is consistent with the diffusive nature of the reaction/diffusion process, as observed for CAR in both the deep ultraviolet [48] and EUV regimes [26].

The latent line width roughness of the lines was also analyzed as a function of bake time, as shown in Figure 3.10. At the shortest bake time, the low-contrast image results in what is probably unreasonably large line width roughness. This data point aside, the line width roughness follows what is perhaps an expected trend: as the bake allows for the deprotection chemistry to set in, the discrete PAG activation events are able to connect via the catalytic acid deprotection reaction, effectively smoothing out the noisy exposure signal. As is seen in Figure 3.10, the result is a rapid decrease in roughness at short bake times, when the local concentration of photoactive components and protecting sites is high, that transitions to a gradually decreasing or even constant line width roughness of about 7.5 nm.

The reduction of roughness can be attributed to both an increase in noise filtering by acid diffusion and to an increase in deprotection gradient. Figure 3.11 shows an example edge

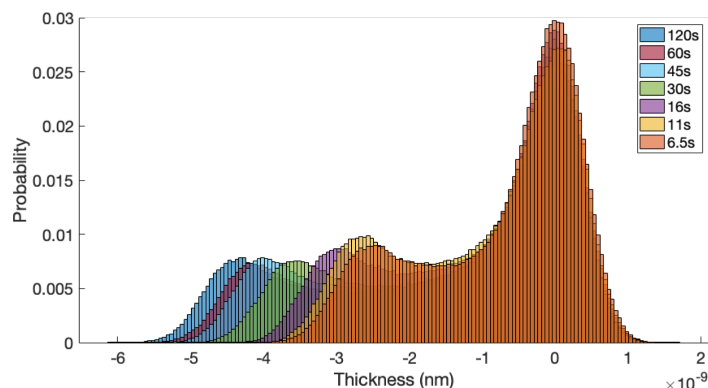

Figure 3.8: Histograms of the line-space images. Right peak corresponds to unexposed pixels, and is centered at zero. Left peak corresponds to exposed pixels. Exposed region shrinks as a function of bake time as deprotection chemistry occurs.

roughness power spectrum, while Figure 3.12 shows an example latent chemistry profile, both for the process of record bake time. From this analysis, the correlation length (Figure 3.13) and the chemical slope Figure 3.14 (here using the latent thickness slope as a proxy) can be measured. In Figure 3.13, it is shown that the correlation length of the lines follows a diffusive trend; as the bake time is increased, the correlation length increases as the square root of the bake time. It is again worth noting that the image obtained at the shortest bake time is low contrast, skewing the analysis of the correlation length of this image. This point aside, the data shows that it is possible to obtain a direct measure of the acid-driven deprotection blur at the latent stage by measuring deprotection-induced shrinkage. The filtering properties

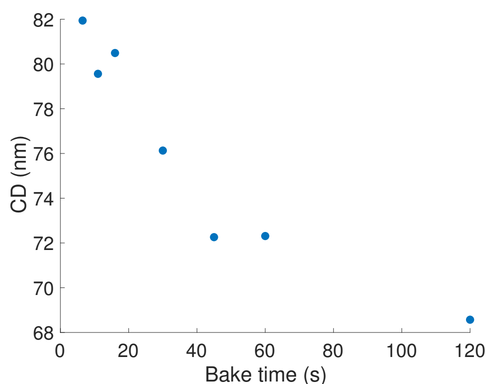

Figure 3.9: CD vs bake time plot. As the bake time increases, the CD decreases in a manner consistent with a diffusion-driven reaction.

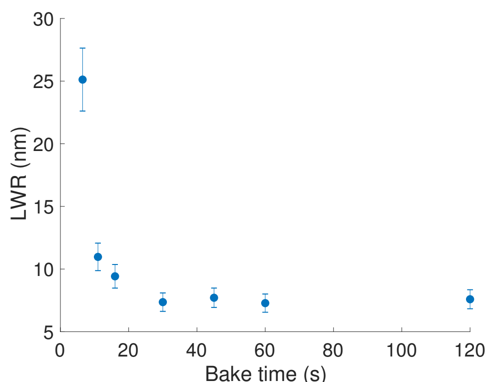

Figure 3.10: LWR vs bake time plot. Like the CD, the LWR rapidly decreases at short bake times, then plateaus.

of the acid diffusion process lead to a decrease in high-frequency contributions to the edge roughness. However, as the resist is a high contrast CAR, the overall acid blur and change in acid blur is relatively small as a function of bake time. It is thus not this process that is primarily responsible for improvements in line width roughness.

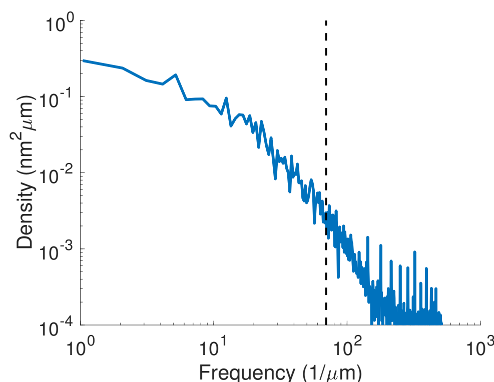

Figure 3.11: LWR power spectral density at 60s bake time. Dashed line indicates the correlation length of the roughness.

As has been well-documented in the literature, line edge-roughness is inversely proportional to the deprotection slope induced by the exposure process [29] [12] [5] [4] [15] . As shown in Figure 3.14, which plots the inverse slope as a function of bake time, a rapid improvement in deprotection slope is observed as the bake time is increased. More than the increase in the filtering due to acid diffusion, this increase in slope accounts for the improvement in line width roughness. Additionally, the fact that correlation length is increasing as

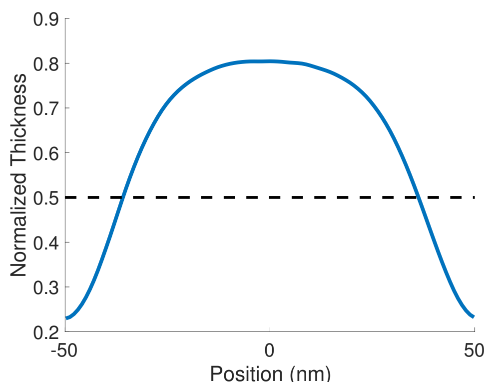

Figure 3.12: Example of average chemical profile at 60s bake time. Normalized thickness used as a proxy for the average chemistry inside of the resist.

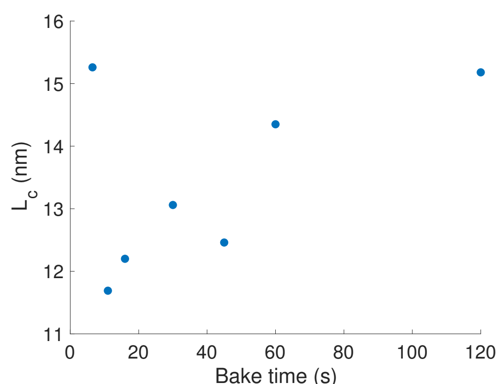

Figure 3.13: Correlation length vs bake time. As the bake time is increased, the correlation length increases as the square root of the bake time, consistent with a diffusion-driven process.

well as the deprotection slope runs contrary to a simple linear systems analysis of the bake, which would predict that acid diffusion would smooth both the chemical noise as well as the edge of the chemical image. However, the bake is not a linear process, especially in light of acid-quencher reactions and the finite number of protecting groups. Thus, the benefit of the bake is twofold, simultaneously improving chemical slope and filtering out exposure noise. The filtering effect has a limit; at small pitches, the acid blur from one exposed line would serve to smooth not only the local edges, but also the line edges of adjacent lines. This crosstalk between exposed features is what limits the resolution of a photoresist, as the deprotection contrast quickly evaporates as the half pitch moves past the correlation length of the resist.

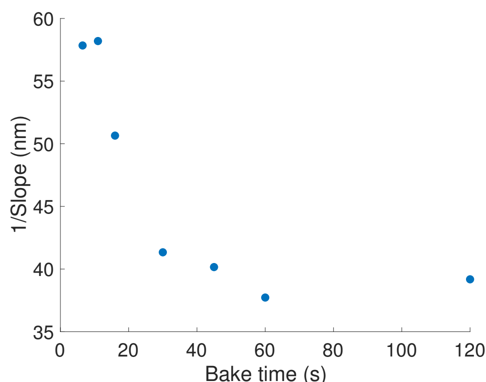

Figure 3.14: Chemical slope vs. bake time. The chemical slope increases with bake time. This is the primary cause of the reduction in LWR, and is evidence of the non-linear nature of the deprotection process.

3.2.2.3 SEM Results

Following measurement with AFM, the samples were developed and measured with SEM. Figures 3.15a, 3.15b, and 3.15c show the comparison of CD, LWR, and L_c at the latent and post-develop stage. It is shown that, other than an offset in the overall CD, the pre and post develop SEM measurements follow a similar CD trend. The SEM trends are consistent with previous work [26], and suggest that the AFM measurement is indeed measuring the latent chemistry inside of the resist. The overall offset could be due to the chosen edge-finding threshold in the AFM and SEM measurements, which could impact the extracted CD of the lines.

Similarly, the line width roughness measurements follow a similar trend: a rapid decrease in roughness at short bake times, followed by a plateau to about 7.5 nm Again, this is good evidence that the AFM measurement is a good representation of the underlying latent image. Furthermore, the fact that the overall roughness is about the same between the two measurement techniques suggests that the high-contrast development process is doing little to smooth or roughen the line edges, though further research is warranted to strengthen this claim.

Finally, the correlation length trends are a little less clear. Correlation length is a particularly sensitive measurement, and is greatly impacted by the focus condition of the SEM. As the resist studied here was very susceptible to SEM damage, it was challenging to establish the best focus condition as the photoresist was rapidly damaged during imaging. Thus, it is possible that some data points, in particular those at 6, 11, and 60 seconds, are the result of non-optimal imaging conditions in the SEM. Those points not withstanding, the overall trend between AFM and SEM lines appears to be consistent. It is interesting to note that at the shorter bake times, the correlation length as measured by SEM is larger than that

measured by AFM. Whether this is due to SEM damage or a filtering effect of the developer represents an interesting and as of yet unanswered question.

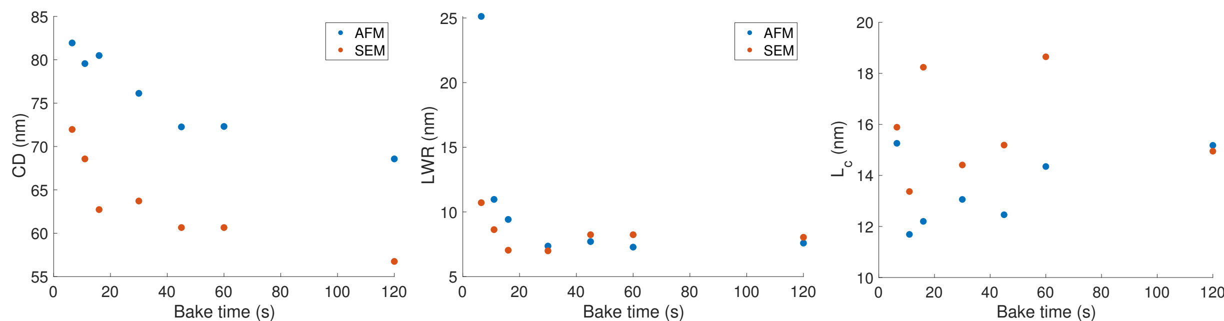

(a) Comparison of CD measurement at the latent stage via AFM to post-develop via SEM.

(b) Comparison of LWR measurement at the latent stage via AFM to post-develop via SEM.

(c) Comparison of L_c measurement at the latent stage via AFM to post-develop via SEM.

3.2.2.4 Latent Image of MOx Resist

A nice feature of the AFM technique is that it is applicable to any resist that exhibits a thickness loss as a function of exposure. Figure 3.16 shows some preliminary data plotted as a histogram on a non-CAR resist. In the figure, there are two doses measured at a short and a long bake time. What is evident from the data is that baking this resist does not result in a significant change in thickness in the exposed areas, suggesting that the chemical propagation mechanism is either extremely fast or not dependent upon temperature. Dose, however, clearly has a strong impact. Further research is needed to fully explore this system, but what is immediately evident (albeit not surprising) is that this system is controlled by a very different mechanism than the acid diffusion that controls the CAR system.

3.2.3 Conclusion

In this study, the effect of bake time on the latent image was measured via AFM and compared with the post-develop results measured via SEM. Good agreement was found in the trends of critical dimension and line width roughness between the two measurement techniques. Correlation length analysis also appears to follow a similar trend. However, the SEM imaging of these thin CAR materials proved challenging due to SEM damage. Further work, either with low-voltage SEM or otherwise optimized imaging conditions would strengthen the conclusions drawn here. Nevertheless, AFM represents a promising technique to study the imaging capability of photoresist independent of the development process, allowing for the creation of improved models of photoresist processes and independent optimization of photoresist and developer.

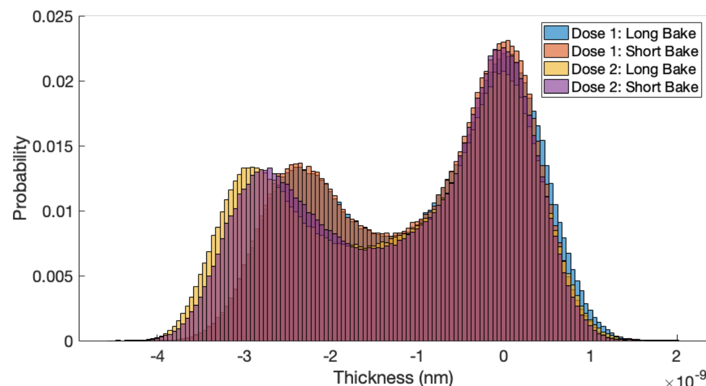

Figure 3.16: Histogram of heights for two exposure doses of a non-CAR at a short and long bake time. As opposed the CAR system, the bake appears to have little effect on the thickness change. Dose, however, clearly changes the thickness profile.

3.3 In-situ dissolution monitoring

Motivated by the ever tighter demands on lithographic performance, the semiconductor industry as a whole has made valiant efforts in improving all aspects of the lithography process, from novel resist materials[17] to underlayer materials[45][9], and even material processing and deposition[1]. Despite these efforts, the workhorse material system used in high volume manufacturing is still chemically amplified resist with $2.38wt\%$ TMAH as a developer.

Previous studies of dissolution using TMAH as a developer hint at the presence of swelling prior to removal of photoresist material. For example the quartz crystal microbalance (QCM) technique[18], has been used to measure the dissolution response of photoresist exposed to clear-field or unpatterned radiation, showing a brief swelling of the resist before its rapid removal[34]. Similarly, Itani et al. performed AFM experiments measuring the dissolution response of patterned resist materials, and also observed swelling prior to removal of the exposed material[20]. This swelling my be a significant contributor to LER, and has been cited as a motivating factor in the search for novel developers, including a tone-switch by using solvent developer[25][16]. However, previous AFM work has required significant dilution of the developer solution to enable observation of the dissolution process. Recent work by Ito et al. using QCM on polyhydroxystyrene-based materials suggests that swelling only occurs with dilute developer, while, at most, a very thin layer of swollen material exists during a full-strength develop process[21]. All told, it is unclear whether the dynamics of dilute dissolution are representative of those at full-strength developer.

In this work, a technique for spatially-resolved measurement of photoresist dissolution using full-strength developer is presented. The key enabling factor, a specially-designed flow cell that allows for precise control over the injection of the developer solution, is discussed

along with some of the practical difficulties encountered along the way. A series of early results are presented, showing the ability of the system to measure the dissolution of line-space patterns at the single-digit nanometer and sub-second temporal scale, as well as the ability to track key lithographic metrics such as line edge roughness as a function of dissolution time. The study concludes by showing images captured at nearly 10 Hz, achieved by scanning the AFM probe across the sample in a non-raster pattern.

3.3.1 Materials and Methods

3.3.1.1 Materials

For the purposes of technique development, a commercially-available CAR resist was used throughout the results presented in this paper. The resist is known to be a relatively high resolution material, with a correlation length of about 15 nm. The resist was patterned using 100 keV electron beam lithography, with dose to size of around 220 µC cm^{-2}. The dose to clear of the same material to EUV radiation is around 12 mJ/cm^2.

The developer used in this study was ma-D 525 from microresist technology, a 2.38% solution of TMAH without surfactant.

3.3.1.2 Atomic Force Microscope

The AFM used to perform these experiments is the Cypher VRS from Asylum Research. This instrument was used for the studies in Section 3.2, but using the standard imaging module at frame rates of about 1 frame every thirty minutes. For these experiments, the VRS module was used. The VRS module enables high-speed imaging through its stack of z-piezos: one for course, slow height modulation over relatively large length scales, and a second for fine, fast modulation. As a result, high-quality images can be captured in fractions of a second. The VRS perfusion cantilever holder assembly was used for this study, which offers the minimum distance between the liquid inlet/outlet of the commercially-available holders.

3.3.1.3 Flow cell

A major challenge with in-situ measurement of photoresist dissolution is that the experiment must be set up in a liquid environment, as the presence of fluid affects the mechanical characteristics of the cantilever oscillation as well as the optical properties of the imaging system responsible for measuring the cantilever motion. This starting liquid must not dissolve the resist, and must be replaced by the developer in order for dissolution to occur. A diagram showing the default liquid channel created by the sample and cantilever holder is shown in Figure 3.17. The issue with this setup is twofold. First, due to the relatively large distance between the liquid inlet/outlet in the cantilever holder, the concentration of developer that reaches the sample changes as a function of time; the displacement of the starting fluid (normally water) by developer is accompanied by a front in which the two fluids have mixed,

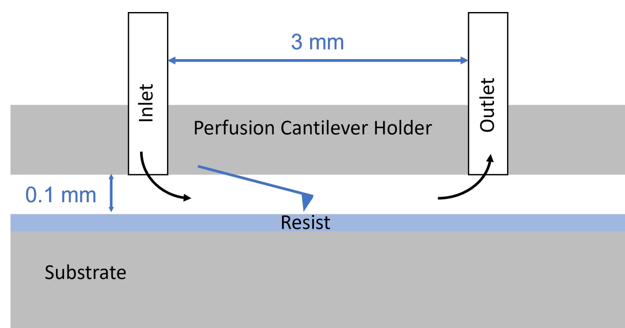

Figure 3.17: Schematic of the flow cell created by the perfusion cantilever holder and the substrate

creating a concentration gradient. This makes it difficult to assign the dissolution phenomena to any particular concentration of developer.

An even greater challenge is posed by the optical disturbance created by the mixing of the two fluids. Figure 3.18 shows the result of an early attempt at performing a full-strength dissolution experiment using AFM. Here, the dark shadow that passes over the optical image of the tip and sample comes from the incoming developer front. This shadow occludes the optical feedback that measures the cantilever motion, which in turn provides the information used to adjust the height of the sample relative to the tip, ultimately producing the topographic map of the sample. Once the water has been effectively displaced by the developer, the occlusion passes. However, during this brief time, the resist has more or less completely developed. Measurement of the key dissolution dynamics are thus missed during the fluid exchange process.

To overcome these issues, a special flow cell was designed. As shown schematically in Figure 3.19a, the flow cell is designed to have two separate channels separated by a small pore. The top channel is initially filled with the starting fluid (i.e. water), while the bottom channel is filled with developer (i.e. TMAH). The pore is created using a punctured silicon nitride membrane. The sample to be studied, in this case patterned photoresist, is placed right next to the window. The experiment is set up such that, initially, water is forced from the top channel through the pore to the bottom channel, sequestering the developer in the bottom channel (Figure 3.19b). Then, using microfluidic pumps, the pressure is changed at the desired time to force the developer from the bottom channel through the pore to the top channel (Figure 3.19c). Due to the proximity of the patterned resist and the pore, the developer that is introduced to the sample is nearly instantly at full concentration. Furthermore, as developer is coming from below the tip, the occlusion effect mentioned above is minimized (though not completely eliminated, as discussed in Section 3.3.1.6).

An early version of the flow cell is shown in Figure 3.20a. The cell is made of polyether ether keytone (PEEK), in which the developer-containing channel is milled. Figure 3.20b shows the fluid cell closed up, with the water inlet/outlet in the top of the cantilever holder.

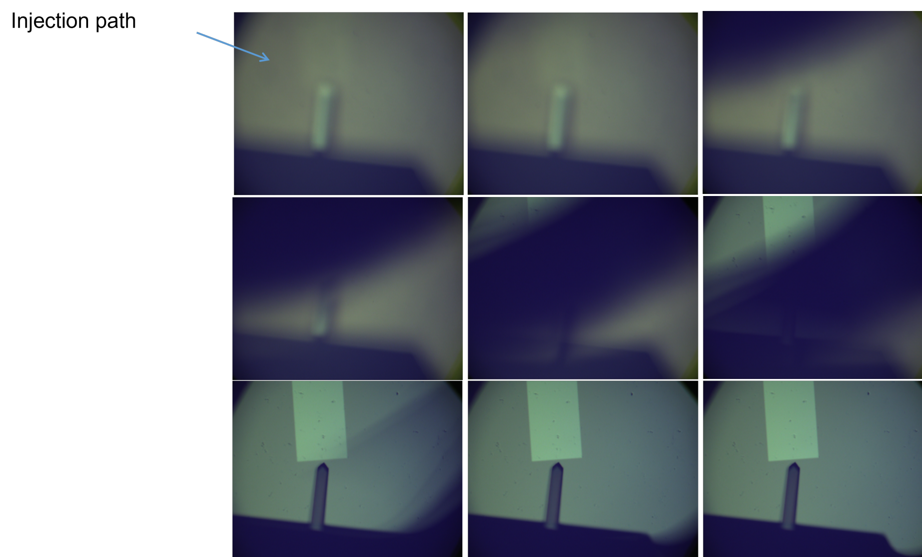

Figure 3.18: Optical images of the cantilever tip during an early attempt to flow TMAH while imaging using the default perfusion holder. The increase in optical contrast of the exposed rectangle after the occlusion passes over the cantilever is evidence that the sample has developed. Imaging is not possible while sight of the cantilever is occluded.

During an experiment, the flow cell is epoxied to the sapphire surface of the Cypher VRS stage for scanning.

3.3.1.4 Z-piezo Response

As previously mentioned, the imaging modality used for the in-situ AFM study is known as amplitude modulation tapping mode, where the amplitude of the cantilever oscillation is held constant by moving the sample closer to or further from the tip during the scan according to the topography of the sample. In the Cypher AFM, all of x, y, and z motions are handled by piezos that displace the sample relative to the tip. In the Cypher VRS, there are in fact two z piezos, a "slow" piezo, responsible for the bulk motion of the sample, and a "fast" piezo that makes the small adjustments at high speed that enable video-rate scanning. However, the frequency at which the z-piezo can respond to changes in cantilever oscillation amplitude is limited by inertial factors that create a sort of resonance in the piezo response. The resonant effect leads to a delay in the z-position of the stage relative to the amplitude signal, and furthermore, to an over-correction of the z-stage position, that together conspire to destabilize the imaging. Thus, amplitude signals that occur near or above the resonance must be filtered in order to avoid unwanted stage motion, at the expense of tracking the high-frequency features of the image. As the frequency at which the amplitude of the tip changes is directly related to the speed at which the sample is being scanned, the maximum

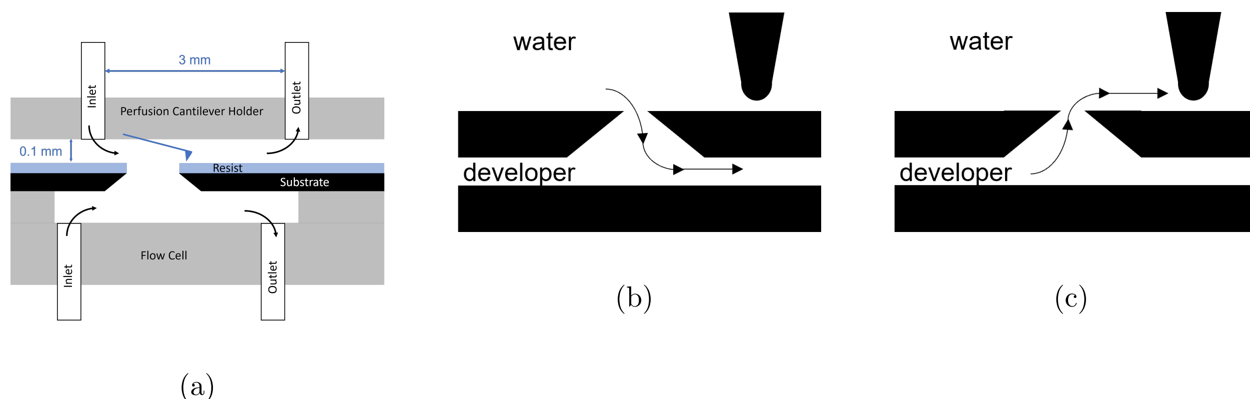

(a) (b) (c)

Figure 3.19: Schematic of the flow cell. a) Overview. Two channels allow two fluids to be located near the sample such that full strength developer can be delivered to the resist without complete displacement of the initial fluid. b) Initial flow conditions. Fluid inert to the resist flows from the top channel to the bottom, sequestering developer below the substrate. c) Final flow conditions. Developer from the bottom channel is forced from the bottom channel to the top channel, rapidly contacting the resist sample.

stable imaging rate is effectively set by a combination of the desired frame rate, and the fidelity with which the tip tracks over the sharp changes in sample topography (such as that at the edge of line/space pattern).

To test the frequency response of the z-piezo, a series of different masses in the form of stainless steel disks were adhered to the VRS stage. A tip was brought into contact with the disks. The z-piezo was then driven by an external waveform generator, and the frequency swept across the expected resonance. The deflection signal coming from the tip, being in contact with the sample, is thus a measure of the resulting motion of the piezo relative to the drive signal. Figure 3.21 shows the result of this experiment. In the absence of any additional mass, the stage shows a small resonance just above 100 kHz. However, as additional mass is added to the piezo, the frequency of the resonant behavior drops to around 65 kHz. This result, combined with observed instability during preliminary dissolution experiments, motivated trimming away extra PEEK material from the flow cell. The resulting flow cell is shown in Figure 3.22. Despite the improved frequency response of the trimmed-down liquid cell, in collecting the results found here, it was observed that it is necessary to filter all amplitude signals above about 45 kHz in order to maintain stable imaging.

3.3.1.5 AFM cantilever

For high-speed AFM measurements, it is desirable to have a cantilever with a high resonant frequency, such that the feedback has several oscillations worth of amplitude data per pixel. In these experiments, the earliest results were achieved using the Arrow-UHF probe shown as the large image in Figure 3.23. Tip parameters are shown in Table 3.1. This primary issue

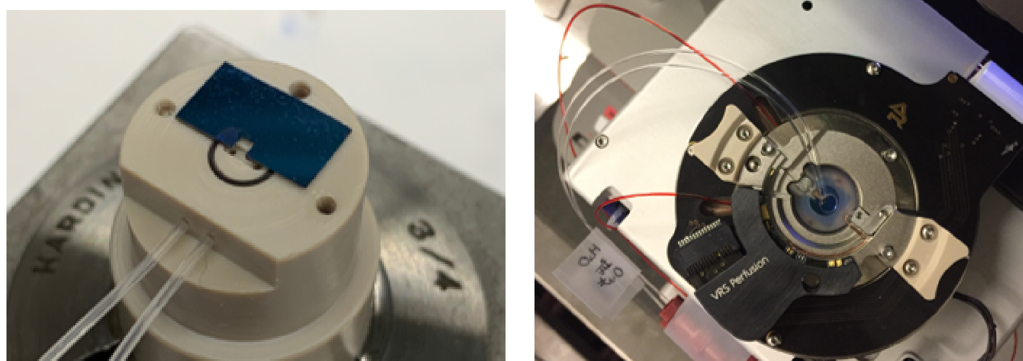

(a) Early version of the flow cell, still on the lathe. Adhered to the flow cell is a cross-sectioned SiNx membrane; a full frame with a punctured window forms the pore between channels.

(b) Closed flow cell. The Cypher VRS perfusion holder forms the top of the flow cell. Clear lines correspond to the inlet and outlet of the top channel, while the red lines correspond to the inlet and outlet of the bottom channel of the flow cell, dyed red here for diagnostic purposes.

Figure 3.20

with this tip is that it is relatively stiff; when imaging over the soft polymer surface created by the photoresist, the tip tended to cut into the sidewalls of the resist, particularly when imaging at high speeds. A more appropriate tip for soft resist materials is the USC F1.2 k0.15 probe shown in the inset of Figure 3.23, approximately to scale with the Arrow-UHF. This tip has a similar in-air resonant frequency, but with a much lower stiffness. However, to achieve both high frequency and low stiffness, the tip must be made much smaller than its Arrow-UHF counterpart. As discussed in Section 3.3.1.6, this had repercussions for the stability of imaging.

3.3.1.6 Fluid Mixing and Index Matching

As mentioned in Section 3.3.1.5, early results were achieved with the Arrow-UHF cantilevers, but the smaller USC cantilever is preferable. However, the early attempts at using these tips were foiled by loss of tracking during the injection of the developer. In fact, as highlighted in Section 3.3.2.1, even the most successful early attempts with the Arrow-UHF tips suffered from some instability as the developer was injected. After much troubleshooting and a number of failed experiments, the root cause of the problem was uncovered. It turns out that, just as the early attempts using the standard VRS perfusion cell setup failed due to mixing-induced occlusion of the AFM tip, the new flow cell design suffered from some minor

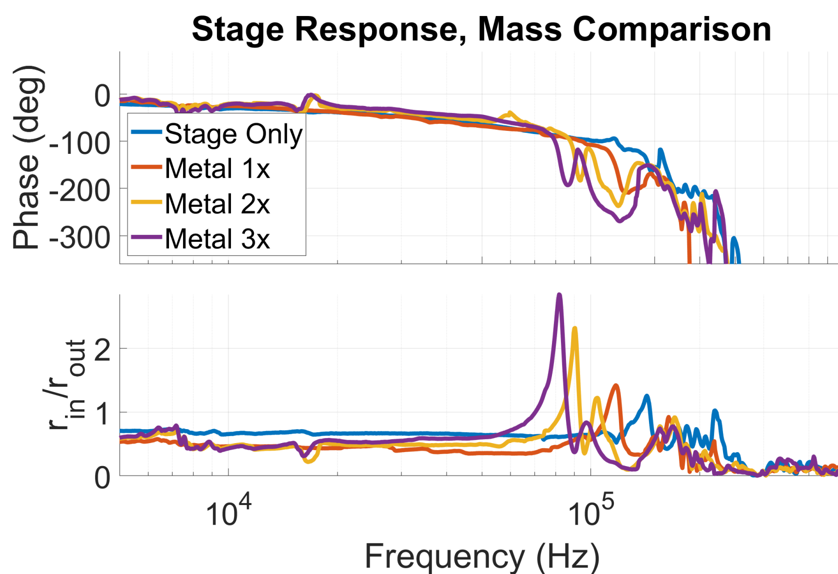

Figure 3.21: Frequency response of the z-piezo as a function of mass. As more mass is adhered to the stage, inertial effects lower the resonant frequency of the pizeo. As this resonance causes imaging to be unstable, amplitude signals at and above the resonant frequency must be filtered, which results in a filtering of the resulting image.

Figure 3.22: Current flow cell. Excess mass has been removed to push resonant frequency of the piezo-flow cell system as high as possible.

	UHF Arrow	**USC f1.2 k0.15**
f_0	1.5 MHz	1.2 MHz
k	8 N/m	0.15 N/m
L	35 µm	7 µm
$< W >$	42 µm	2 um

Table 3.1: Comparison of AFM probe parameters. f_0 is the frequency of the first harmonic in air, k is the probe stiffness, L is probe length and $< W >$ is the average probe width. Note the substantial drop in stiffness for the USC f1.2 k0.15 probe relative to the UHF Arrow, and the corresponding drop in probe dimensions.

Figure 3.23: SEM images of two different probes used for dissolution experiments. The large image is the Arrow UHF probe. The small probe in the inset, approximately to scale, is the USC f1.2 k0.15 probe, which is preferable to the Arrow UHF for studying soft polymers due to its lower stiffness, but presents challenges for the feedback laser due to its reduced size.

optical disturbances caused by differences in the index of refraction between the developer and water. As shown schematically in Figure 3.24, the developer solution, a mixture of TMAH salt and water, has a subtly larger refractive index than water. The interested reader can turn to a paper by An et al. for an interesting discussion of the role of water displacement and polarizability of ions and their connection to refractive index[2]. As a result when the developer is introduced to the top flow channel, the index mismatch forms a sort of lens that causes a small deflection of the feedback laser, particularly when the developer is first injected. While the effect is much less dramatic than the situation without the flow cell, the small deflection is still sufficient to cause the laser to miss the very small cantilever onto which the laser is focused.

To solve the problem, the initial fluid was swapped from water to one with an index of refraction near that of the developer - a $2.38wt\%$ solution of NaCl due to its availability and its neutral pH of 7. Several control experiments were conducted, which suggested that a pre-rinse with this solution prior to development had no discernible effect on dose to clear

Figure 3.24

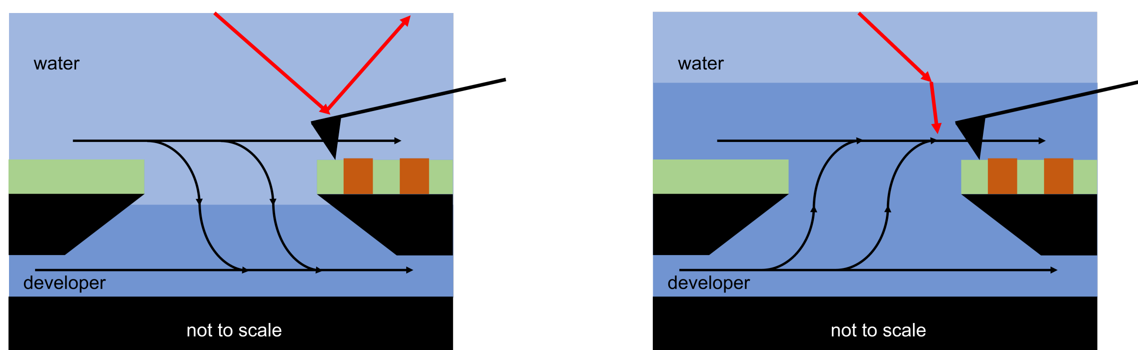

(a) Initial flow conditions. The subtly more dense developer solution is sequestered below the tip. Laser feedback and scan parameters are established.

(b) Flow conditions switched such that developer is introduced to the top channel. The subtle change in index of refraction causes the laser to miss the cantilever. Tracking is lost.

or dose to size of the commercial CAR used for technique development. The change from water to a weak NaCl solution as the beginning fluid proved to be the final change needed to really push the imaging speed limits of the technique, and enabled the high speed results presented in Sections 3.3.2.2 and 3.3.2.3.

3.3.1.7 Spiral Scanning

As a final improvement, the tip scan pattern was changed from the default raster scan to a spiral scan as described by Zeigler et al.[47]. As outlined in Section 3.3.1.4, due to the combination of additional mass from the flow cell as well as the intrinsic resonance of the z-piezo, high frequency amplitude signals must be filtered in order to maintain stable imaging. Unfortunately, this filtering limits the resolution of the imaging process at high x-y scan speeds, as faster x-y speeds directly translate to higher frequency amplitude signals. Thus, for a given filter on the amplitude signal coming from the cantilever, there is a maximum scan speed that can be used, above which the height map (built from the z-piezo motion) loses its high spatial frequency information.

In a traditional raster scan, the velocity of the probe relative to the sample surface becomes very slow at the x extremes of the image, while the velocity is maximized throughout the middle of the scan pattern. As a result, to achieve a given frame rate, the scan speed between turn-arounds must be greater in order to make up for lost time. In contrast, a spiral scan such as that described by Zieler et al.[47] enables scanning to be performed such that

the probe is constantly in motion, maximizing the rate of useful data collection. As a result, a spiral pattern can be used to scan an equivalent area as a raster pattern using lower average and maximum velocities. A plot showing a theoretical raster pattern and an experimentally measured spiral pattern at a 10 Hz frame rate is shown in Figure 3.25. As illustrated in the figure,the spiral scan enables lower scan speeds, which translates to improved image quality. This enables an increase in frame rate such that the sample dynamics can be probed at a greater temporal resolution for a given scan area and data density.

Figure 3.25

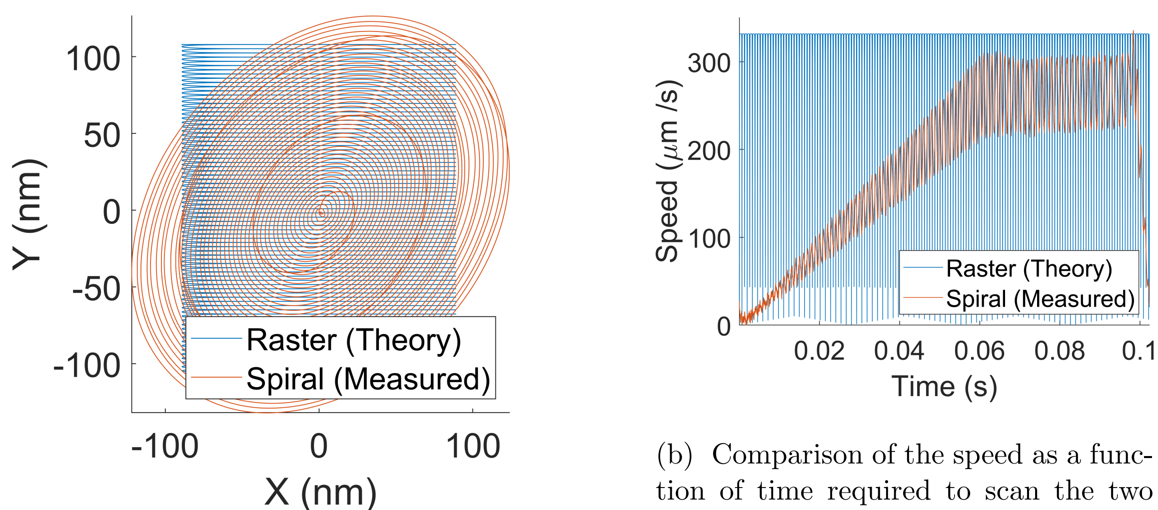

(a) Comparison of two scan patterns covering approximately equal area. In blue is the standard raster scan, while in red is the spiral scan pattern.

(b) Comparison of the speed as a function of time required to scan the two patterns. Due to stopping at the edge of each scan line, the raster pattern needs a higher average and maximum speed to achieve the same frame rate as a spiral scan, which is constantly in motion.

3.3.2 Imaging Results

3.3.2.1 Early Results

In the earliest results, collected with Arrow-UHF cantilevers and with pure water as the starting solution, the results of previous in-situ dissolution experiments using AFM were reproduced. These results are presented in Figure 3.26. In particular, by using flow conditions that correspond to a weak developer solution, a significant swelling of the resist material prior to removal is observed. However, by adjusting the flow conditions used to inject the developer, a more full strength develop condition was achieved. These results are shown in

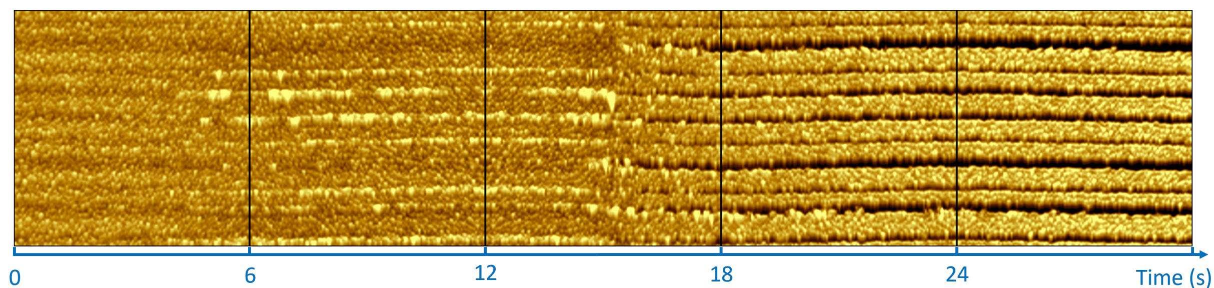

Figure 3.26: Early result captured at 6 s/frame using a flow condition that leads a low developer concentration. Low concentration leads to swelling of photoresist, consistent with prior findings.

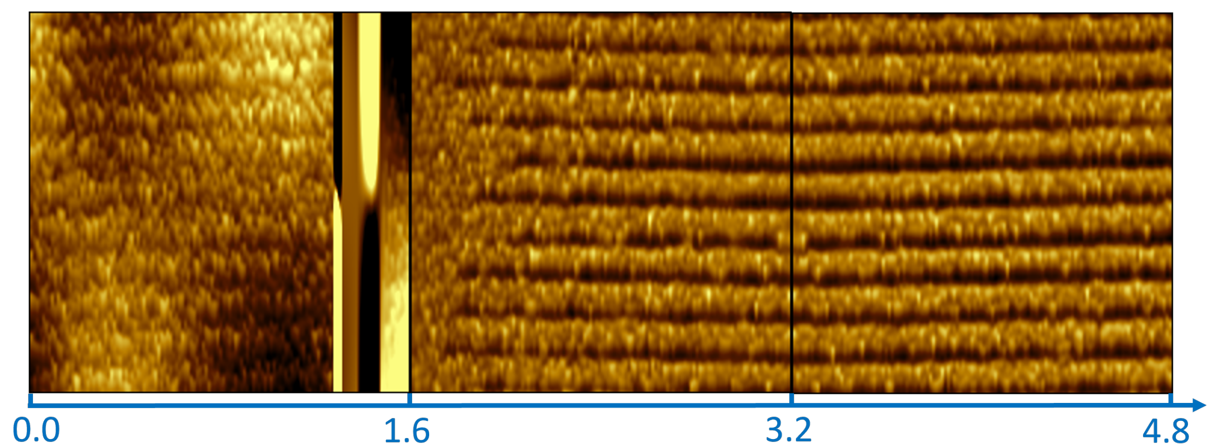

Figure 3.27: Early result captured at 1.6 s/frame using a flow condition that leads to nearly full strength developer. No swelling was observed, but tip tracking was lost for a few scan lines as the developer was injected.

Figure 3.27. In this data, no swelling of the photoresist material was observed. However, as hinted at in Section 3.3.1.6, the experiment suffered from a few scan lines where the probe was not tracking the surface. The dynamics clouded by these few scan lines, coupled with the confidence that the scan rate was not near the imaging speed limits of the instrument, motivated the improvements to the experimental technique that culminated in the data presented in the next section.

3.3.2.2 Index-matching Results: Raster Scan

By index matching and using a more appropriate tip, as outlined in Sections 3.3.1.5 and 3.3.1.6, the system was able to stably image throughout the dissolution process. To test

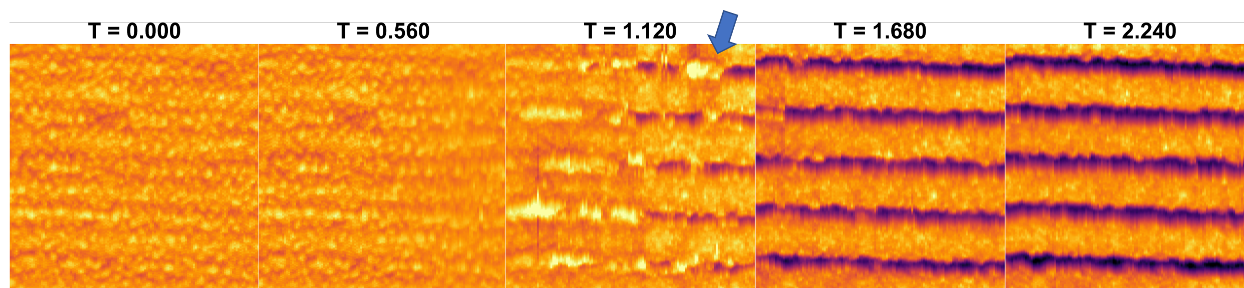

Figure 3.28: First high speed imaging result using index matching and soft cantilever probe. Frame rate was 1.9 Hz. Stable tracking throughout the development revealed that swelling does indeed occur at full strength developer. Furthermore, swollen regions along the line edge appear to correlate with lateral protrusions from the line edge, indicating the formation of LER.

out the improved system, 100 nm pitch lines exposed via electron beam lithography at a 1:1 duty cycle were studied. The first result is shown in Figure 3.28, which was taken at a 1.9 Hz frame rate. In this data set, each image is approximately 500 nm $\times$ 500 nm, with 128 total lines scanned sequentially from left to right in an image, yielding approximately 4 nm pixels in the horizontal direction. Each line was scanned from bottom to top of the image, with the pixel size along this direction about 1 nm. The developer was injected in approximately the middle of the second frame ($T = 0.560$). With the improved tracking and imaging speed, swelling was observed during dissolution that the previous full strength developer data did not reveal. Furthermore, it was observed that, even in areas of the line that were nominally exposed to the same dose, the swelling and dissolution appeared to occur at different times. For example, take the uppermost trench as it develops in Figure 3.28 in the frame T=1.12. Here, one can see a blob of swelling, indicated by the blue arrow, that was measured later chronologically than the developed part of the line just to its left. This suggests that the system is measuring inhomogenity in the dissolution process, though at this stage it is not possible to identify whether this comes from the electron beam exposure, material inhomogeneity, the developer, or a combination of all three. Interestingly, the swollen bump appears to leave behind a nodule on the line edge once the bulk of the material is removed, which is perhaps expected of an under-deprotected region of resist.

Intent on improving upon these results, imaging was performed at a faster frame rate. However, due to the z-piezo limits highlighted in Section 3.3.1.4, this necessitated reducing the overall area being imaged. The resulting data is illustrated in Figure 3.29. In this data set, the frame rate was 3.9 Hz, with each image having area 250 nm $\times$ 250 nm, 64 lines per frame, and an equivalent pixel size and scan direction as the previous data set. Just as in the last data set, one can see the presence of swelling before rapid removal of the material. With the improved frame rate, it becomes increasingly apparent how the middle of the exposed region is removed first, followed by a gradual removal of the lesser-exposed

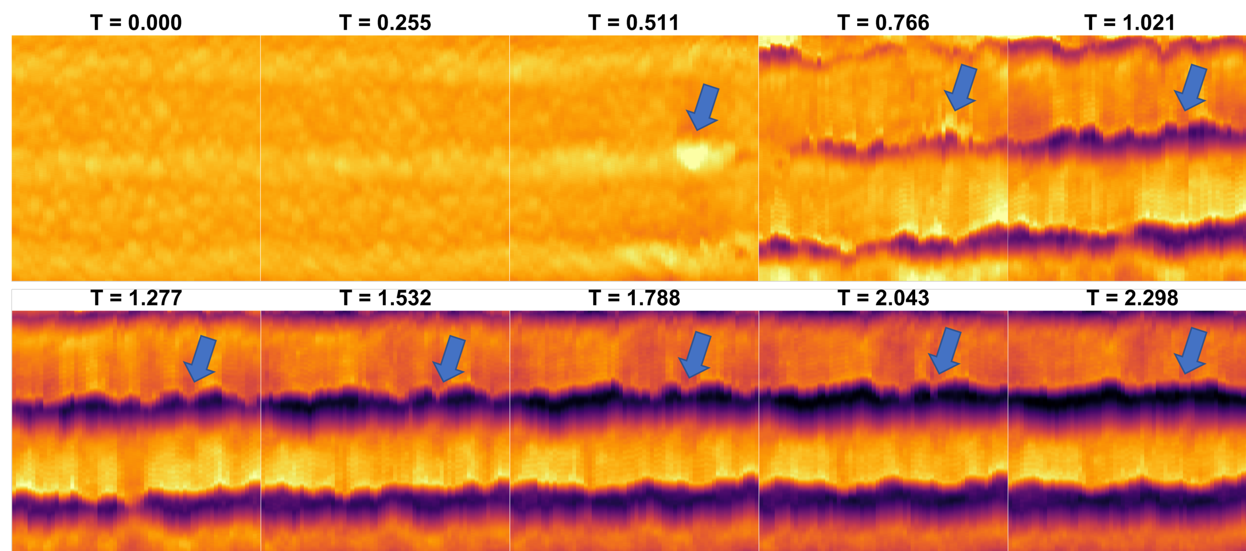

Figure 3.29: Dissolution data set collected at 3.9 Hz. Scan area was reduced due to the imaging speed constraints set by the z-piezo. Finer temporal resolution reveals the gradual opening of the trench during development. As with the 1.9 Hz data set, swelling preceeds removal of resist, with most swollen regions corresponding to bumps on the line edge. As development progresses, small bumps are smoothed out, suggesting that the developer serves to filter LER after the inital removal of material.

resist surrounding the trench. In particular, one can track the material in the vicinity of the swollen bump indicated by the blue arrow. Just as in the previous data set, the removal of this swollen region leaves behind a nodule on the line edge. However, tracking that nodule throughout the development process reveals that the developer slowly removes the bump, leaving behind a smoother line edge. This is likely due to the fact that, once the bulk of the material is removed, the developer is able to interact with the resist not only from the top down, as is initially the case, but also from inside the developed parts of the trench, effectively increasing the dissolution rate of protrusions. To put some numbers to this effect, the line edge corresponding to this protrusion was fit using SuMMIT[36], and LER data extracted as a function of dissolution time. The results is shown in Figure 3.30. Matching the obvious visual effect, the LER of the line edge decreases rather rapidly near the beginning of the develop before saturating at a minimum value near 30 s. It is worth noting that 30 s is the develop process of record for this photoresist material.

Naturally, it was desirable to make yet another improvement in our scan speed in an attempt to fully resolve the swelling and removal of the resist material. However, even at the current frame rate, there were some artifacts introduced by the speed of the scan when transitioning from the top of the line to the trench, a phenomena known in the AFM community as "parachuting". Furthermore, increasing the frame rate would require another reduction in image area, representing a challenge at the 100 nm pitch being measured here.

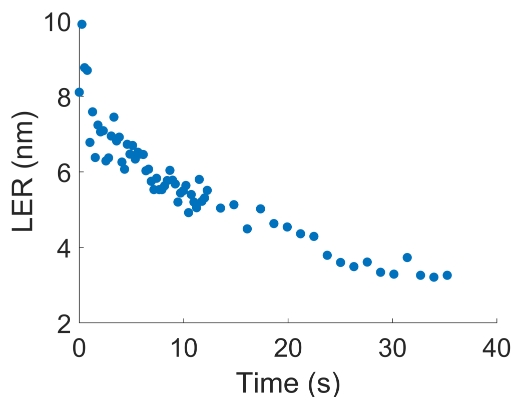

Figure 3.30: LER of the line edge indicated by the blue arrow in Figure 3.29. The line is roughest just after its formation, and smooths as the developer works away at the partially exposed material at the edge. LER plateaus at around 30 s, the process of record develop time for this resist.

To take the next step in frame rate, the scan was changed to the spiral scan discussed in Section 3.3.1.7.

3.3.2.3 Index-matching Results: Spiral Scan

In conjunction with changing scan pattern, the pitch of the pattern features was reduced from 100 nm to 60 nm. The desired radius of the spiral was set to 400 nm, with the realized scan, illustrated in Figure 3.25, being elliptical and having an average radius of about 275 nm. With these conditions, the system was able to scan stably at 9.7 Hz, a nearly 2.5× improvement over the result shown in Figure 3.29. A few of the resulting frames are shown in Figure 3.31, showing the improved temporal resolution with which it is now possible to observe the dissolution process. At this frame rate, the system can measure entire frames where the exposed regions of resist swell before their removal. This combination of scan pattern, index matching, and cantilever choice generates data of sufficient quality to begin using our technique to study the effect of process parameters and resist formulation on the resulting dissolution dynamics of the material.

3.3.3 Conclusion

A technique that is capable of measuring the dissolution dynamics of photoresist material with sub-10 nm spatial resolution at 10 Hz has been developed. This technique enables a detailed study of the resist dissolution properties, which can be used to focus on the impact of dissolution on the formation of stochastic defects such as LER, and even more catastrophic effects such as line bridges and breaks or missing contact holes. The early results attained using the novel flow cell have already uncovered that resist swelling is indeed present during

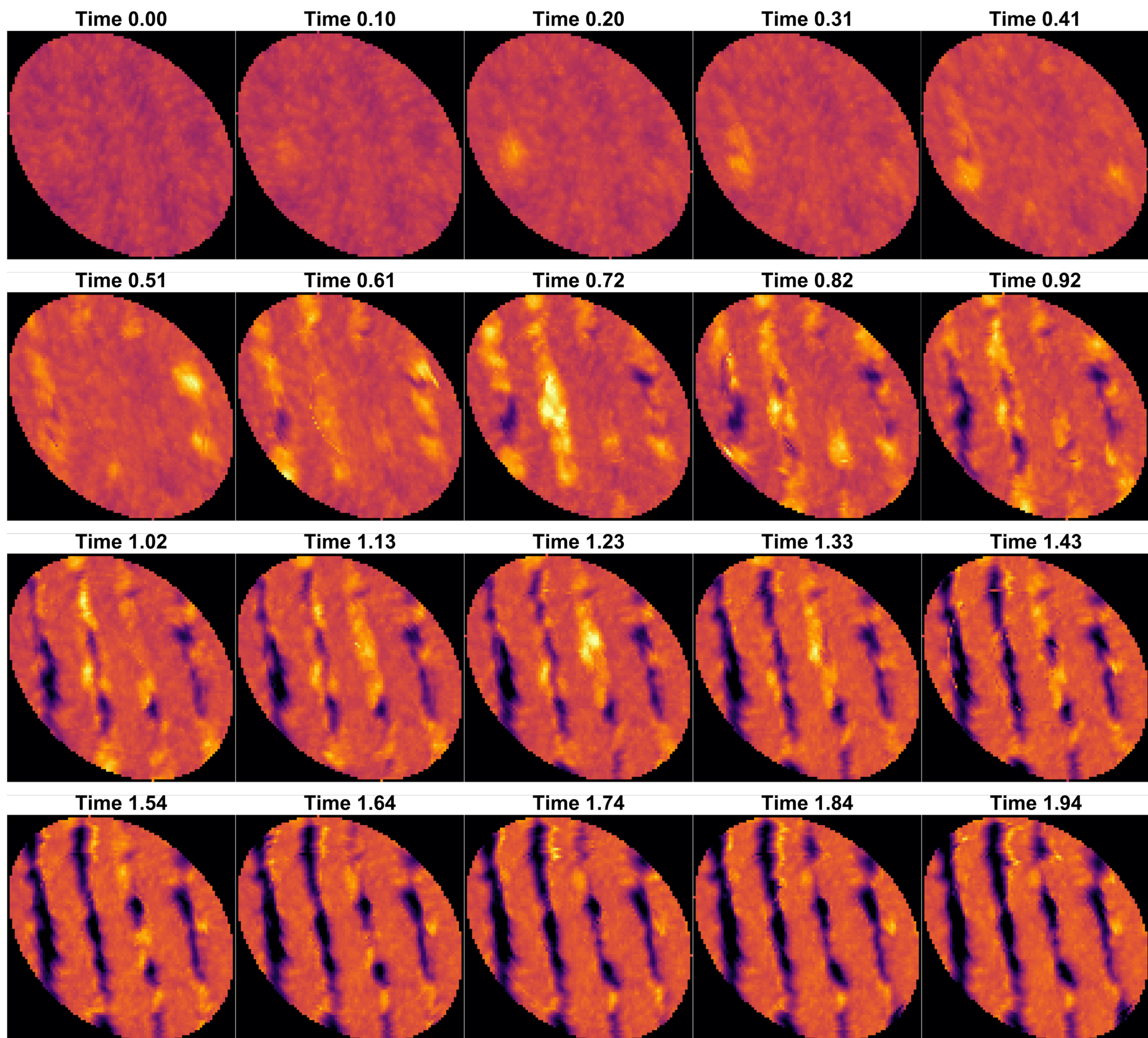

Figure 3.31: Data captured using spiral scan pattern at 9.7 Hz. With this level of temporal detail, it can be seen that the middle of the exposed feature swells and is removed most rapidly, leaving behind lesser-exposed swollen resist on the sides of the trench that is also removed as the develop process proceeds.

dissolution of a commercial EUV CAR at full developer strength, a result that was in doubt prior to these experiments. Furthermore, the results suggest that the dissolution process appears to act as a filter on LER following bulk removal of highly exposed material. This has implications for the connection between resist dissolution and the resolution and roughness of the patterning process, and suggests further research into optimizing the development process is warranted. Moving forward, the system will be used to study the impact of resist formulation as well as process parameters such as dose and developer strength or composition on the resist dissolution process. Ultimately, this will lead to better understanding of the interplay between all these parameters and the resulting quality of the printed features. To that end, the technique has just scratched the surface.

Chapter 4

RSoXS Metrology

This chapter focuses on the use of resonant soft X-ray scattering (RSoXS) for measuring the spatial distribution of material components within photoresist. After a brief introduction to the technique, the chapter is divided into two applications of RSoXS: RSoXS for understanding the homogeneity of either unexposed materials or those exposed to a uniform field of radiation, called a “clear field exposure”, and for the measurement of the latent image profile. In both types of study, the aim is to understand the distribution of material components, such as the photoacid generator additive or the polymer protecting group, by using X-rays tuned to an energy that will diffract off the desired chemistry under study. In the unpatterned samples, the resulting diffraction measures the homogeneity of the desired chemistry, while measurement of patterned samples produces discrete diffraction orders related to the underlying pattern.

4.1 RSoXS Basics

4.1.1 Theory

RSoXS is the combination of near edge X-ray absorption fine structure (NEXAFS), Figure 4.1a, with traditional X-ray scattering, Figure 4.1b. From NEXAFS comes the elemental and even chemical specificity that makes RSoXS a promising technique for exploring photoresist chemistry. When the incident photon energy is near that of the ionization energy for an electron bound by an atom in the sample, a boost in absorption cross section occurs. Fermi's Golden Rule and the dipole approximation yield an absorption cross section[7]

$$\sigma_x = \frac{4\pi^2 h^2}{m^2}\frac{e^2}{hc}\frac{1}{h\omega}\xi(E)| < \phi_f|\vec{e}\cdot\vec{p}|\phi_i > |^2\delta(h\omega + E_i - E_f). \tag{4.1}$$

Where h is Plank's constant, e is the electron charge, m is the electron mass, c is the speed of light, ω is the X-ray frequency, $\xi(E)$ is the density of states, $| < \phi_f|\vec{e}\cdot\vec{p}|\phi_i > |^2$ is the square of the dipole matrix element, and $\delta(h\omega + E_i - E_f)$ enforces the conservation of energy. Of particular relevance to the work discussed here are the dipole matrix element, which selects

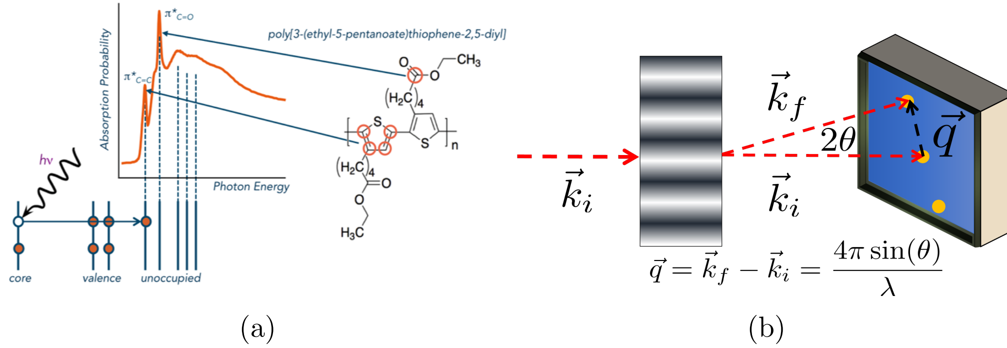

(a) (b)

Figure 4.1: Schematic of the RSoXS technique, which combines (a) NEXAFS with (b) X-ray scattering. Scattering is measured as a function of $\vec{q}$, the momentum transfer of the scattered photons, itself related to the total momentum of the X-ray, $2\pi/\lambda$, where λ is the wavelength, and the sine of the scattering angle, θ.

transitions with $\Delta l = \pm 1$, and $\xi(E)$. It is the density of states that describes the underlying electronic structure of the material being studied, and is both atomically and, particularly for small Z elements such as carbon and oxygen, chemically sensitive. This is because the Rydberg-like states near the continuum are strongly affected by the local environment of the radiation-absorbing electron, and in particular, by any bonds in which the parent atom of the electron is participating. This change in density of states, coming first from being near the ionization energy of the atom, and modified by the local environment of that atom, leads to absorption spectra that are sharply energy dependent. The absorption spectra are thus fingerprints of the underlying atomic and molecular makeup of the sample being probed.

When the absorption properties of the sample are not only energy dependent, but spatially varying as well, then an appropriately tuned beam of X-rays can be used to perform scattering experiments, in which the far-field diffraction pattern of X-rays is used to understand the distribution of scatterers within the sample. To understand how this comes about, one can turn to Maxwell's equations, combined here to form the wave equation for the electric field,

$$(\frac{1}{\mu\epsilon}\nabla^2 - \frac{\partial^2}{\partial t^2})\vec{E} = 0. \tag{4.2}$$

This equation can be put into a more convenient form by making a series of substitutions. First, one can observe that solutions to this equation take the form $e^{i(\vec{k}\cdot\vec{x}-\omega t)}$, where ω is the frequency of light. Second, the index of refraction, $n = \sqrt{\frac{\mu\epsilon}{\mu_0\epsilon_0}}$, can be introduced, along with the vacuum speed of light, $c = 1/\sqrt{\mu_0\epsilon_0}$. Finally, one can introduce the magnitude of the free space wave vector, $k_0 = \omega/c$. All together, these substitutions yield a Helmholtz equation for the spatial distribution of the electric field

$$(\nabla^2 + n^2 k_0^2)\vec{\tilde{E}} = 0 \tag{4.3}$$

where $\vec{\tilde{E}}$ is the electric field with the temporal component removed. From here out, both the vectorial nature of the electric field, as well as the tilde notation will be dropped. Ignoring the vectorial nature is justified when the length scale of the sample under study is large relative to the wavelength, and when the diffraction pattern is observed many wavelengths from the sample[14]. In general, these conditions will be met in the experiments conducted here.

It is important to note that the index of refraction is in general a complex number. In the X-ray literature, the index of refraction is usually denoted by $n = 1 - \delta + i\beta$, where δ describes the refractive component, and β describes the absorptive component.

When the index of refraction is not spatially dependent, solutions to this equation are of the form $e^{in\vec{k_0}\cdot\vec{x}}$, i.e. plane waves of wavenumber $n\vec{k_0}$. However, the index of refraction is rarely homogeneous throughout all of space. Perhaps most simply, in practical X-ray experiments, the sample is of finite thickness, surrounded by a vacuum environment on either side. At a minimum, this leads to an index that changes from 1 to n and back to 1 as the beam impinges upon, interacts, and then leaves the sample for the detector. Of particular interest for scattering experiments is the case where the index is inhomogeneous within the sample. In this case, if the spatial variation in index of refraction is weak, the index can be divided into a term describing the mean value within the sample, and a second perturbation term

$$n^2 = n_0^2 + \delta n(\vec{x})^2 \tag{4.4}$$

with the Helmholtz equation becoming

$$(\nabla^2 + n_0^2 k_0^2)E = -\delta n(\vec{x})^2 E. \tag{4.5}$$

An exact solution to this equation is given by

$$E = E_0 - \int dV G(\vec{x}, \vec{x'}) \delta n(\vec{x})^2 E, \tag{4.6}$$

where E_0 is the homogeneous solution to the Helmholtz equation, and $G(\vec{x}, \vec{x'})$ is the outgoing Green's function of the Helmholtz equation,

$$G(\vec{x}, \vec{x'}) = \frac{-1}{4\pi} \frac{e^{-ik_0|\vec{x}-\vec{x'}|}}{|\vec{x}-\vec{x'}|}, \tag{4.7}$$

which describes a spherical wave emanating from source point $\vec{x}$ to observation point $\vec{x'}$. Because E still exists on both sides of the equals sign, it is in general non-trivial to solve this equation. However, a common approach in the X-ray literature is to apply the Born approximation, in which the homogeneous solution E_0 is used in place of the E in the Green's integral

$$E = E_0 - \int dV G(\vec{x}, \vec{x'}) \delta n(\vec{x})^2 E_0. \tag{4.8}$$

As mentioned above, of interest in scattering experiments is the radiation far from the sample. Thus, the Green's function can be expanded in the so called far-field manner. Following Jackson[22],

$$G(\vec{x}, \vec{x'}) \approx \frac{-1}{4\pi} \frac{e^{ik_0 r}}{r} e^{-i\vec{k'} \cdot \vec{x}}. \tag{4.9}$$

Putting it all together, and substituting a unit plane wave in for E_0,

$$E \approx e^{i\vec{k} \cdot \vec{x}} + \frac{1}{4\pi} \frac{e^{-ik_0 r}}{r} \int dV e^{-i\vec{k'} \cdot \vec{x}} \delta n(\vec{x})^2 e^{i\vec{k} \cdot \vec{x}}. \tag{4.10}$$

The second term describes the scattering, and is often written

$$F(\vec{q}) = \int dV e^{-i\vec{q} \cdot \vec{x}} \delta n(\vec{x})^2 \tag{4.11}$$

where $\vec{q} = \vec{k'} - \vec{k}$, or the vector describing the change in momentum of the beam. In other words, the scattering distribution is equal to the Fourier transform of the refractive index of the sample, evaluated at the change in momentum vector.

Experimentally, it is not possible to measure the electric field of the diffracted beams, but rather their intensities, $|F(\vec{q})|^2$. The resulting loss of phase information represents a major challenge to the interpretation of scattering data, especially when the desire is to reconstruct the real space structure of the scatterer. This issue of reconstruction is discussed later in this chapter. However, if one simply desires to understand the underlying statistics of the sample, the scattering data provides some ready information. In particular, under the Born approximation, the scattering signal represents the Fourier transform of the autocorrelation function of the scatterers. In other words, the scattering signal is a sort of power spectrum of the underlying spatial distribution of sample composition. It can thus provide information on any characteristic length scales in which the scatterers may aggregate. As discussed in Chapter 2 of this thesis, the power spectrum of the chemistry induced by exposure and subsequent bake is of the utmost importance to the shot noise-averaging properties of the resist. Furthermore, aggregation of additives, such as PAG, would negatively affect resist performance - the ability to directly measure aggregation within the film would be useful for screening photoresist. And finally, patterning itself can be thought of as introducing a sort of aggregation, in this case, the aggregation of resist into exposed and unexposed chemical domains.

The ability to measure different scattering signals corresponding to different molecules in the sample by making minor changes in incident X-ray energy is what distinguishes RSoXS from hard X-ray scattering techniques. In the subsequent sections of this chapter, my efforts to use RSoXS to characterize resist materials are presented and discussed, both for homogeneously exposed films and patterned samples.

4.1.2 Experimental Geometry

RSoXS experiments are conducted in two different geometries, transmission and reflection. The reflection geometry is sometimes called GiSAXS for grazing incidence small X-ray scattering. The two geometries are illustrated in Figure 4.2. In the transmission geometry, samples must be made on thin SiNx windows that allow for transmission of the X-ray beam, as soft X-rays, unlike hard X-rays, cannot penetrate a full-thickness silicon wafer. This presents some fundamental challenges for sample preparation, namely that spin coating of the photoresist, exposure, bake, and any other desired processes must be conducted on a fragile substrate with different thermal, mechanical, and even chemical properties than the standard silicon used in semiconductor manufacturing. However, the upfront effort in sample preparation is rewarded at the data analysis step, as the transmission configuration in principle enables the use of the Born approximation. In contrast, the grazing incidence configuration allows for the use of hearty silicon substrates more akin to those used in actual photolithography. However, the data analysis must account for multiple "scattering" interactions with the substrate, as, unlike the thin film samples being measured, the silicon wafer is decidedly not a weak, perturbation term that allows for standard application of the Born approximation. Instead a modified version of the Born approximation must be used, which accounts for scattering from the substrate. This modified approximation is known as the distorted wave born approximation (DWBA), and is more computationally expensive than the Born approximation due to the additional reflection terms that must be considered. These considerations are of particular significance when measuring patterned photoresist samples, as discussed in a later section.

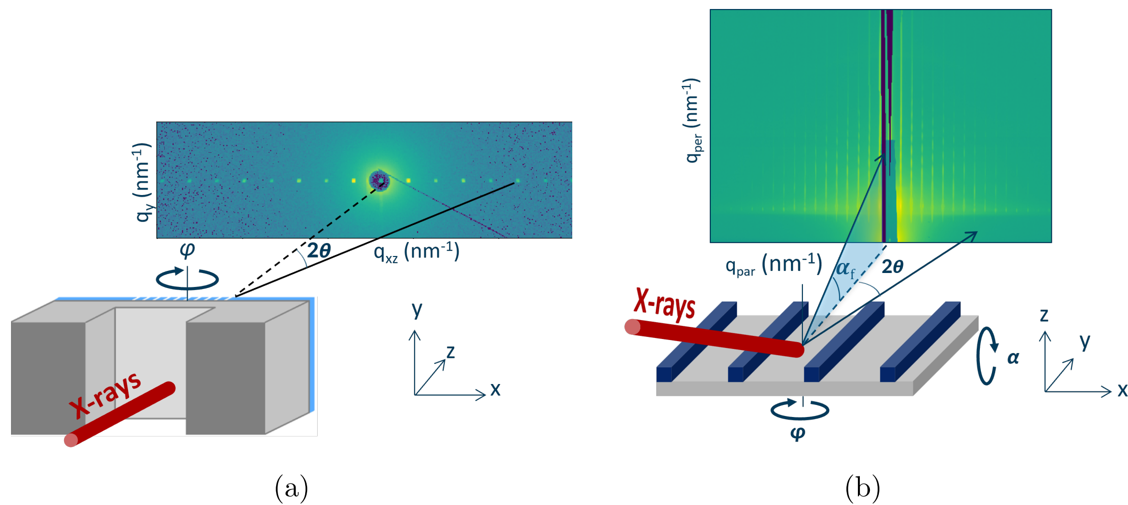

Figure 4.2: Schematic of RSoXS experimental configurations

NEXAFS spectrometry can also be carried out in either of the two configurations. In transmission, the flux of the direct beam is measured both with and without transmission

through the sample. The absorption is then calculated as $abs = -\log(I/I_0)$, where I_0 is the direct beam intensity and I is the intensity after passing through the sample. It is also possible to use the fluorescence caused by the relaxation of excited electrons to measure the NEXAFS spectra by using signal from regions of the detector where scattering is expected to be minimal. In the reflection configuration, NEXAFS can be measured in either of the discussed modalities (though comparison of the now reflected direct beam requires a more sophisticated understanding of the reflection process). In addition, if the substrate is a doped silicon wafer, then measurement of the current generated by photoionized electrons can also be used to provide NEXAFS spectra.

4.2 Clear Field Samples

In this section, the application of RSoXS to clear-field exposed samples is discussed. As mentioned above, the goal of these experiments is the measurement of material homogeneity in the thin film resist samples, with a focus on the uniformity of the deprotection chemistry and of the chemical additives in the polymer host. The technique was applied to CAR resist at the Advanced Light Source (ALS), where the primary focus was carbon edge chemistry. Similar experiments were conducted in parallel by Tanaka et al. at the NewSubaru light facility in Japan[19], where distinct scattering curves were measured for different types of polymer-based resist materials. In addition, this thesis discusses the application of resonant scattering to metal oxide resist materials, where the metal L edge was the primary focus. These experiments were carried out at Brookhaven National Lab.

4.2.1 CAR Resist

4.2.1.1 Initial Modeling

To look for the kinds of phenomena that may be observed via an RSoXS experiment, simulations were first carried out using previously published experimental NEXAFS data[10]. The data are shown in Figure 4.3. In this data, the total electron yield (TEY) was measured as a function of the incident X-ray energy, and used to quantify the absorption of X-rays by a commercial CAR, both exposed and unexposed. This absorption data was then combined with known absorption data of the constituent elements far from the carbon edge, and the refractive component, δ, solved for using the Kramer's-Kronig relationship. As implied in the previous section, the scattering strength of the system is related to quadratic sum of the difference in refractive index. The wavelength-dependent relative contrast is plotted in Figure 4.3c.

As a baseline modeling test, the experimental data was combined with simulation results from the MPPM to produce an anticipated scattering pattern in accordance with the theory described in the previous section. As a test case, the scattering at 285 eV, where contrast should be maximized due to resonant X-ray absorption by carbon, vs bake time was simulated. The results are shown in Figure 4.4. With the zero order masked out (the

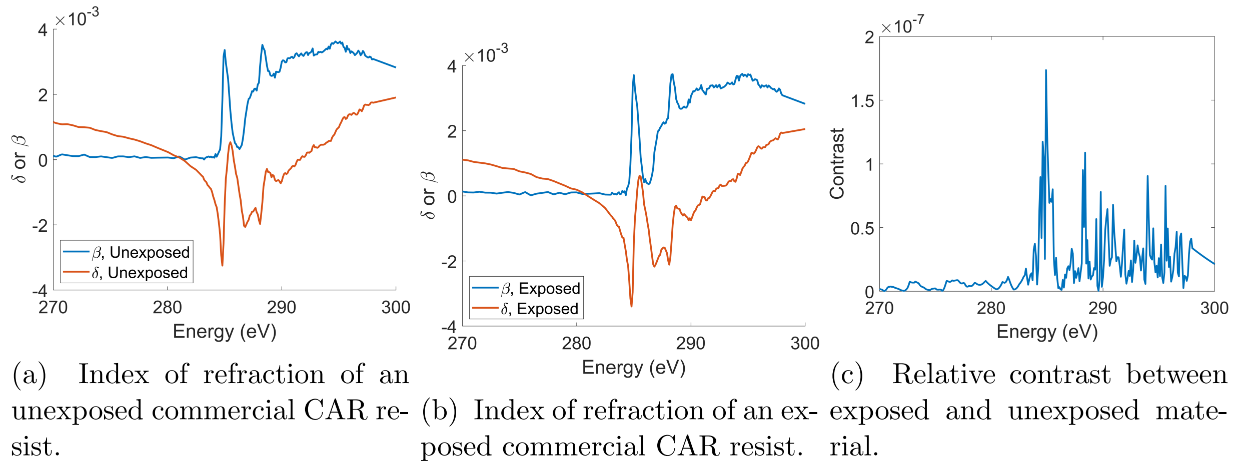

(a) Index of refraction of an unexposed commercial CAR resist.

(b) Index of refraction of an exposed commercial CAR resist.

(c) Relative contrast between exposed and unexposed material.

Figure 4.3: NEXAFS of a commercial resist.

vast majority of light passes through the sample unperturbed), one can see a diffuse haze around the direct beam that changes as the sample is baked. In particular, at short bake times, the scattering is weak and diffuse, as the vast majority of the sample is un-reacted polymer material with the rare occurrence of deprotected resist. As the acid diffusion process has had little time to propagate, the deprotection characteristics mimic that due to white noise, which show up as roughly equal power at all frequencies, or scattering angles. As the bake progresses, the exposure chemistry propagates, and the film becomes more uniformly deprotected. As a result, the scattering signal becomes more concentrated around the direct beam, consistent with the low-pass filtering effect of acid diffusion during PEB. In the limit of perfectly homogeneous deprotection, the X-ray beam would pass through unscattered (though somewhat less intense due to absorption). In this simulation, that situation never occurs: the combination of photon and material noise conspires such that, even at the full baketime, there remains some variation in the amount of deprotection chemistry in the film. These early modeling results motivated the experimental results shown in the next sections.

4.2.1.2 Experimental Results

The modeling results in the previous section were based upon a propriety resist material whose chemical makeup remains a secret. For technique development purposes, the experiments presented here were conducted with an open source material, a co-polymer blend of polyhydroxystyrene and a tertbutyl ester protecting group. The base polymer is shown in Figure 4.5a. The deprotection mechanism of this resist is the conversion of the tertbutyl ester into carboxylic acid by the photoacid, yielding a material that is soluble in 2.38 weight percent TMAH. Into this material was added a triphenylsulfonium nonaflate (TPS-Nf) PAG, shown in Figure 4.5b, at zero weight percent (no PAG), 20 weight percent, and 40 weight percent. One goal of the experiment was to see if, at very high PAG loadings, PAG-rich

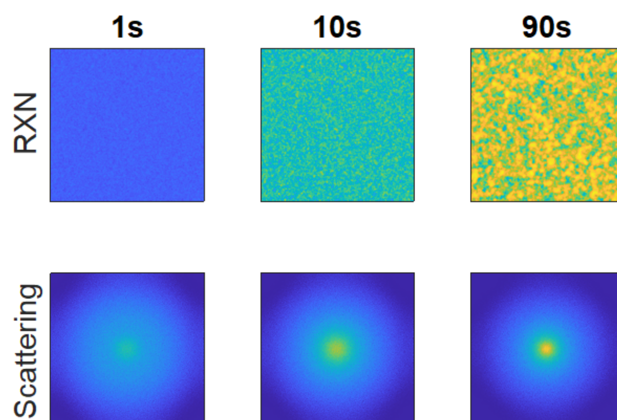

Figure 4.4: Modeled scattering vs bake time using experimental index of refraction shown in Figure 4.3.

domains form within the sample. The samples were spun on SiNx membrane "windows" to enable experiments to be performed in a transmission configuration.

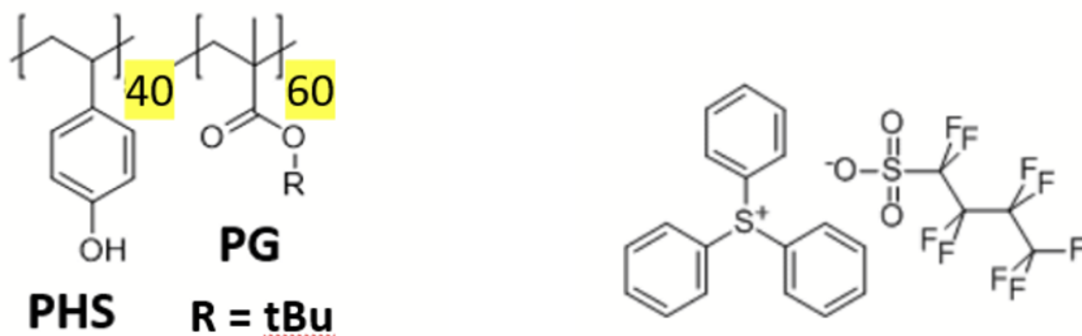

(a) Structure of the model resist used for RSoXS studies. The blend is 40 percent PHS, and 60 percent tert butyl ester protecting group.

(b) Structure of triphenylsulfonium nonaflate used as the PAG in the model CAR material.

Figure 4.5

TPS-Nf PAG is not only sensitive to EUV photons via electron-driven chemistry, but

248 nm DUV photons by way of resonant absorption. Because EUV photons are difficult to come by, the resist was exposed using UV radiation. For the simple study used here, a UV-ozone cleaner was used as the source of photons. As ozone will strip the resist from the substrate, the samples were placed as far from the UV lamp as possible to limit the amount of ozone contact.

The X-ray absorption of the each of the samples, both exposed an unexposed, was measured using a photodiode by comparing the flux of the direct beam to the beam that passed through the sample. As the direct beam and the through-sample measurements must be taken at different times, the intensity on the photodiode is normalized by the photoelectron current coming from a gold mesh upstream in the beamline. This normalization accounts for any changes in the beam flux between measurements. The resulting NEXAFS spectra at the carbon edge are shown in Figure 4.6. The addition of more PAG in the resist seems to increase the overall absorption of the film, consistent with the presence of additional carbon atoms from the PAG. The exposure process has the opposite effect, lowering the overall absorption. This is consistent with the known deprotection chemistry, which leads to the tert butyl group outgassing from the polymer material upon deprotection. However, the change in NEXAFS spectrum of the zero weight percent PAG sample suggests that the UV-ozone cleaner may have had a mild stripping effect on the film despite the distance between the samples and the bulb. Ideally, a more controlled light source will be used for future experiments.

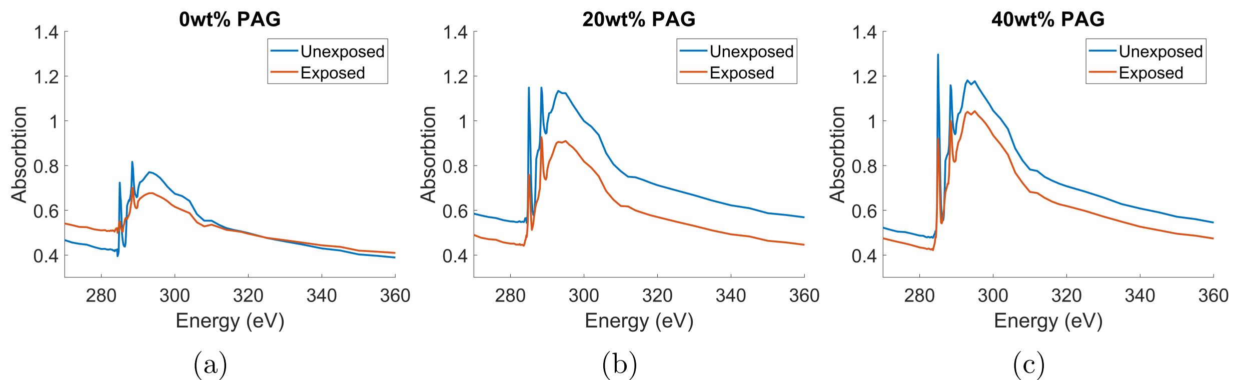

(a) (b) (c)

Figure 4.6: NEXAFS spectra of model material with varying PAG loading.

The diffraction pattern emanating from the sample was measured using a CCD contained in the X-ray chamber at a few of the interesting wavelengths suggested by the NEXAFS spectra. To minimize beam damage, each of the scattering measurements were taken at a new location across the SiNx window. The resulting intensity vs the scattering vector $\vec{q}$ are shown in Figure 4.7. Far below the carbon edge, the scattering signals for all the samples appeared more or less the same, as would be expected in the absence of the resonant absorption effect. However, at energies near the carbon edge, the scattering behavior of each of the samples diverged. The samples with PAG appeared to have, overall, the same

characteristic scattering shape, suggesting that even at very high loading, no large PAG aggregates form. Nonetheless, the shape of the PAG containing samples diverge from that of the non-PAG containing samples, suggesting that the PAG itself is contributing to the scattering signal in a non-trivial way. The effect of exposure on the scattering signal was more dramatic. At energies 284.5, 285, and 287 eV, the scattering signal appears to decay more quickly in the exposed samples than in their unexposed counterparts. As discussed in conjunction with Figure 4.4, this suggests that the overall chemistry of the film is somewhat more homogeneous as a function of exposure, though the fact that the film without PAG loading is also changing again points to some role of the UV-ozone exposure beyond the expected deprotection chemistry.

The same set of experiments were repeated near the fluorine edge, with the goal of looking specifically at the PAG-induced absorption and scattering in the film. The NEXAFS spectra, collected in the same transmission configuration as at the carbon edge, are shown in Figure 4.8, while the scattering measurements are shown in Figure 4.9. The NEXAFS scans were clearly very noisy; indeed, the absorption at the fluorine edge is expected to be lower than that at the carbon edge, both due to the lower number of fluorine atoms per unit volume in the sample, and the intrinsically lower cross section at higher X-ray energy. Nevertheless, the increased absorption in the PAG containing samples does seem to indicate that the technique is indeed measuring the influence of the TPS-Nf. Interestingly, the scattering data appears more sensitive to the presence of fluorine than the NEXAFS spectra. While the scattering well below the fluorine edge is more or less the same for all the samples, for energies near the edge, the scattering intensity is boosted for the PAG-containing samples consistent with the amount of PAG loading. Despite the apparent sensitivity to the PAG additive, the scattering diagrams show no obvious change in shape at high PAG loadings or due to exposure, suggesting that the technique is not picking up on any aggregation of the additive in the film, and that the fluorine environment is unchanged by exposure.

4.2.2 MOx Resist

A similar study to that presented above was conducted on a metal oxide based resist. In this resist, the basic chemistry is related to a crosslinking reaction by ligands attached to a metal oxide core. For the study presented here, a proprietary material was used, so the precise chemistry involved remains unknown. However, the primary metal was known to be tin. To that end, these experiments were conducted near the tin L edge at Brookhaven National Lab's NSLSII facility. At around 3900 eV, the X-rays used for these experiments are sometimes considered to be "tender" rather than "soft;" nevertheless, the principles involved are the same as for RSoXS.

The samples used in this experiment were coated on bare silicon wafers and exposed in an admittedly inefficient manner using electron beam lithography. The experiments were performed in a grazing incidence configuration. The increased X-ray beam energy of the "tender" X-rays used here enables a increase in the range of $\vec{q}$s that can be measured; this translates to the ability to measure smaller domains than what is possible at the carbon and

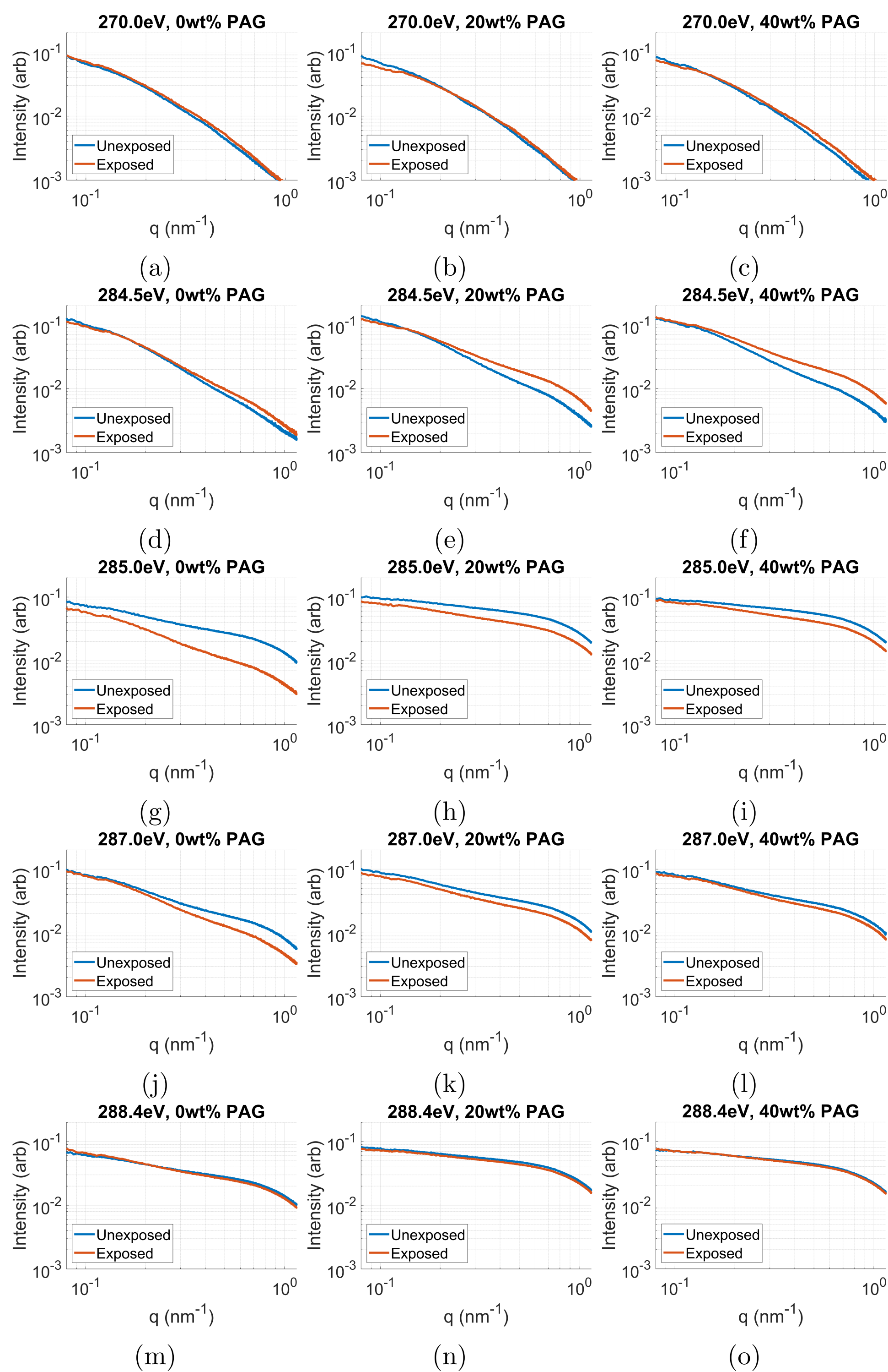

Figure 4.7: Experimental resonant scattering data from a model resist material with varying PAG loading at X-ray energies near the carbon K edge.

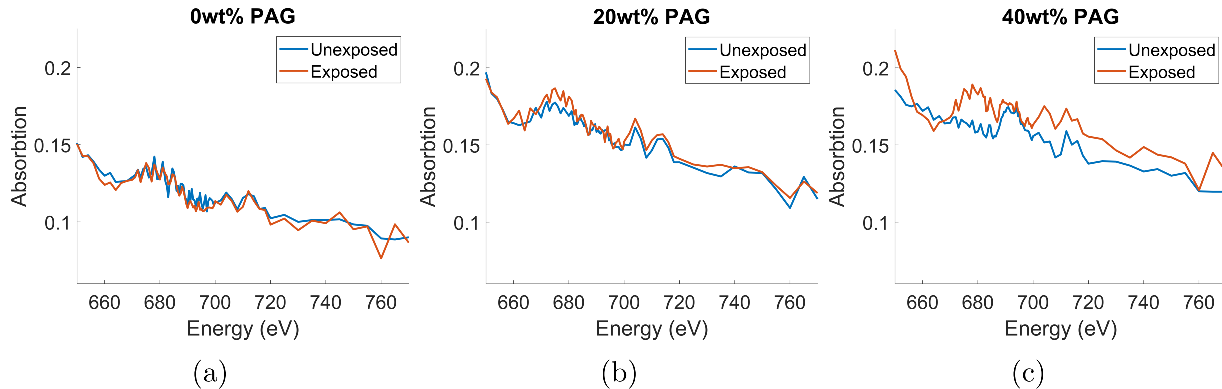

(a) (b) (c)

Figure 4.8: Fluorine edge NEXAFS spectra of model material with varying PAG loading.

fluorine edges. In this experiment, the NEXAFS data was collected by measuring the X-ray fluorescence of the sample, which is captured on the detector at high angle regions where scattering is minimal.

The results of the experiment are shown in Figure 4.10. Figure 4.10a shows the spectra for the exposed and unexposed material. While the two traces look relatively similar, there is divergence at several energies, notably around 3930 eV. Again guided by the NEXAFS spectrum, the scattering from the sample was measured below the edge (3900 eV) as well as at 3930 eV. The results are shown in Figure 4.10b. The unexposed sample scattering curves looked nearly identical aside from a change in intensity at the peak. The length scale of the peak can be estimated as $2\pi/q \approx 1$ nm. Upon exposure, the peak position and shape becomes energy-dependent. Below the edge, the peak shifts to lower $\vec{q}$, suggesting that the average "cluster" has become somewhat larger, and broadens, indicating a broader distribution of cluster size. Near the edge, where the metal oxide core of the resist clusters is highlighted, the peak position is closer in $\vec{q}$ to the unexposed sample, though still somewhat lower. However, the broadening of the peak persists. Taken together, these results suggest that the core of the structure remains approximately the same size; the distance between cores becomes somewhat more random, leading the off-resonant curve, with contributions from all accessible electrons in the material, to broaden and shift, while the on-resonant peak, which is mostly sensitive to the modestly changing core of the nanostructure, remains unchanged aside from broadening due to inter-cluster spacing.

4.2.2.1 Clear field RSoXS Conclusions

RSoXS appears to be a technique capable of measuring chemical inhomogeneity in thin films. In one set of CAR materials, RSoXS showed some sensitivity to PAG loading as well as to exposure, though future exposures will ideally be performed in a more controlled manner. At the fluorine edge, NEXAFS spectroscopy suffered from low signal to noise in the transmission configuration, suggesting that perhaps measuring escaped electrons in a grazing incidence

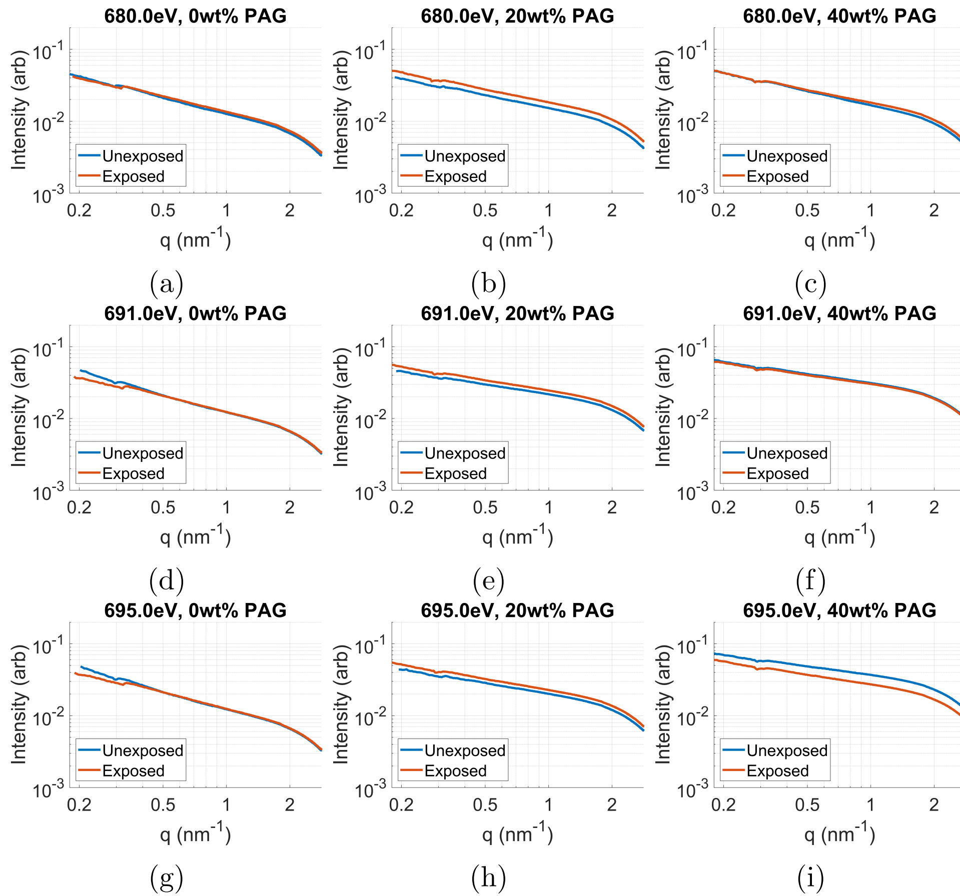

Figure 4.9: Experimental resonant scattering data from a model resist material with varying PAG loading near the fluorine K edge.

configuration is a more appropriate spectroscopic method. Nevertheless, an increase in scattering intensity with PAG loading was observed. Evidence of PAG aggregation was not measured at either the carbon or fluorine edge, suggesting that any aggregation that occurs does so on a length scale smaller than what is accessible at these elemental edges.

Experiments were performed on metal oxide materials at Brookhaven National Lab. These results showed distributional differences, indicated by the scattered X-ray profiles, as a function of exposure and energy near the tin L edge, suggesting the technique is sensitive to changes in cluster spacing with exposure. Taken together, these early results highlight the possibilities of using RSoXS for the measurement of chemical homogeneity and its relation to exposure chemistry and subsequent processing. Future work needs to be dedicated to sample preparation, including finding high-throughput, controlled exposure tools, and to choosing the appropriate spectroscopic and scattering techniques to maximize signal to noise.

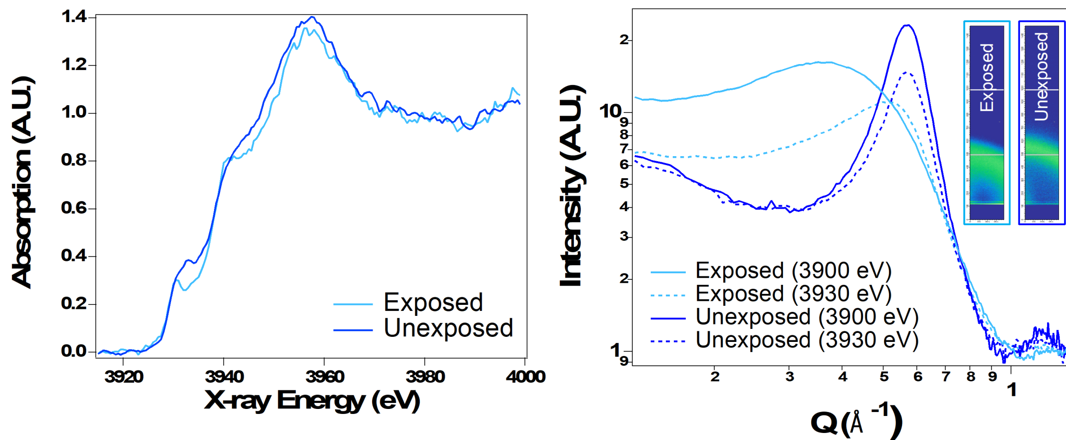

(a) Sn edge absorption of exposed and unexposed MOx resist.

(b) Scattering of MOx resist below and at the Sn edge.

Figure 4.10

4.3 RSoXS for latent image profilometry

In addition to understanding the scattering from unexposed or “clear field” exposed samples, RSoXS also has the potential to be used for measuring the profile of patterned samples, either in the latent or developed state. In this section, efforts to measure the 3D latent profile of patterned photoresist are discussed.

The measurement of patterned samples derives from the equivalent hard X-ray experiment for measuring developed and etched profiles, a technique known as CD-SAXS[37]. In this technique, a beam of hard X-rays impinges upon a nanostructure. The sample is then rotated relative to the incident beam. For a grating, the momentum transfer perpendicular to the grating lines is constrained by symmetry to be $2\pi m/p$, where m is an integer and p is the pitch. However, by rotating the sample relative the beam, the initial momentum of the incoming photons in the frame of the sample changes. The result is that in the outgoing diffraction pattern, each diffraction order, often called a “Bragg spot,” corresponds to a different location $\vec{q}$ in reciprocal space. Thus, by collecting the diffraction pattern at a variety of sample rotations, one builds the reciprocal space PSD of the grating structure. As hinted at earlier in this section, the loss of phase information during this process prohibits direct inversion of the PSD to the physical structure. Instead a forward model is carried out, where a physical structure is assumed, a model is used to simulate the diffraction pattern, the resulting diffraction is compared to that obtained experimentally, and then the model is adjusted until the simulated diffraction is within some tolerance of the measured pattern. Because the forward model needs to be carried out for every guess of the underlying structure, the model needs to be computationally fast. As previously mentioned, the Born

approximation, which can be carried out using simple FFTs, is usually the method of choice in transmission experiments, while the DWBA must be used for data collected in reflection experiments.

In RSoXS, the same technique can be carried out. However, the grating now need not just be a physical one, as the diffraction can be atomically and chemically sensitive as well. Some of the pioneering work in this space was conducted on directed self assembly block co-polymers by Sunday et al. Using a transmission geometry, the authors used res-CD SAXS (as the authors called the technique) to measure the buried morphology of the block co-polymer structure[38]. Similarly, Freychet et al. used CD-RSoXS (same technique, but the name I will continue using here) to measure the latent image formed by electron beam exposed EUV photoresist[10]. It was this work that inspired the subsequent investigation into using CD-RSoXS as means to measure the latent image in resist. In particular, the goal of these efforts was to ascertain whether the technique was capable of measuring, in addition to the latent resist 3D profile, the chemical slope of the latent grating as discussed in Section 2.2, as well as to use the scattering as a means to measuring chemical LER/LWR.

Before moving on, it is worth considering what to expect in experimental CD-SAXS data. According to the Born approximation, scattering experiments measure the PSD of the sample under study. In sticking with the coordinate system in Figure 4.2, a line-space grating that is periodic in the x direction leads to a Dirac delta comb in the q_x direction of reciprocal space. The amplitude of each of these Dirac spikes is modulated by the duty cycle of the line space pattern, the sharpness of the transition between unexposed and unexposed material, and the element q_z that is being probed. Analogously the q_z direction measures the Fourier transform of the z profile of the line space pattern. To get a feel for what this might look like, consider a pattern with vertical sidewalls. In this simplified case, the z shape is a square wave with width equal to the thickness of the resist. The scattering in reciprocal space will thus correspond to a sinc function. Thus, as different q_z values are probed, achieved experimentally by rotating the sample, the Bragg spots will blink on and off with peaks and nulls predicted by the thickness of the resist. Of course, if the actual profile is tapered, the scattering will deviate from this description and instead correspond to the Fourier transform of the true underlying structure.

4.3.1 Initial Modeling

Before conducting any experiments, a few simple simulations were carried out by combining the experimental results shown in Figures 4.3b and 4.3a and the modeling results from Section 2.2. Of primary interest here was to use RSoXS to measure the chemical slope that modeling results suggest is of the utmost importance. To that end, the scattering profiles from the study in Section 2.2 were simulated assuming the experimentally-measured index of refraction. Results are shown in Figure 4.11. In this figure, the traces represent the modeled chemical profile coming from resist formulations with increasing photodecomposable quencher. To the right of each trace is shown the resulting scattering pattern coming from these gratings at 285 eV. The simulated lines and spaces were held to be at a 1:1 duty

cycle. Thus as the resist profiles become sharper, the chemical grating approaches a square-wave. This manifests itself in the scattering simulation as a structure with very little even order scattered light - a perfect square wave has a Fourier transform comprised of only odd multiples of $2\pi/p$. Additionally, one can see a diffuse haze around the diffraction peaks in Figure 4.11. This is coming from the roughness of the pattern being simulated. Indeed, the low-slope simulation has the most roughness in addition to the most even-order scattering. Figure 4.12 shows the PSD as measured by taking a line cut through the first order diffraction peak along the vertical (q_y) direction in comparison to the PSD of the LWR. On the whole, the two appear to take on similar shapes. As the Born approximation indicates that scattering is measuring the Fourier transform of the underlying resist structure, the roll off in the scattering can be attributed to the roughness correlation length introduced by the acid diffusion process. This suggests that RSoXS may be useful in measuring LER independent of the development process.

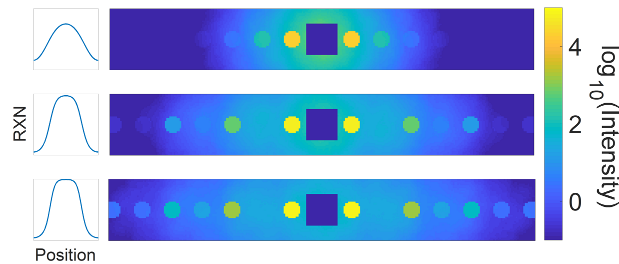

Figure 4.11: Simulated RSoXS experiment using modeled resist chemistry and experimental optical constants. As the chemical profile becomes sharper, the scattering profile corresponds to that of a square wave.

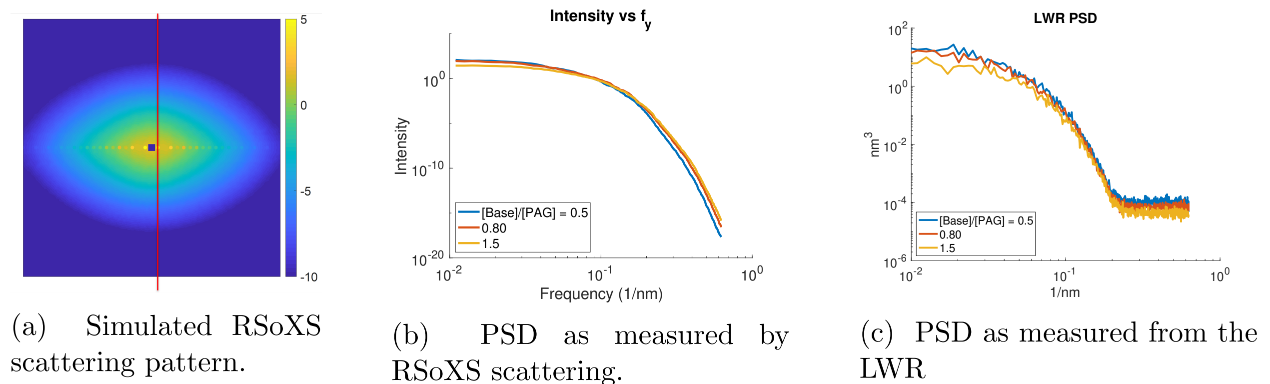

(a) Simulated RSoXS scattering pattern.

(b) PSD as measured by RSoXS scattering.

(c) PSD as measured from the LWR

Figure 4.12

4.3.2 Grazing incidence CD-RSoXS experiment

To test the viability of RSoXS for measuring the chemical slope, several samples were prepared with varying loadings of PDB. The host polymer was the same proprietary material used in Freychet et al, but with different levels of PDB added by the resist vendor. These samples were patterned with electron beam lithography, and the dose was calibrated so that the line:space ratio was approximately 1:1. In essence, the goal was to reproduce the results of Freychet et al., but to additionally include the chemical slope in the reconstruction of the profile. For this experiment, the shutter was opened, and the sample rotated in the α direction of Figure 4.2b while the CCD integrated the moving Bragg spot, creating a “Bragg rod” as the sample angle is changed. The experimental geometry corresponds to that illustrated in Figure 4.2b. The sample was rocked from 34 degrees down to 4 degrees. An example of the resulting data is shown in Figure 4.13, which looks similar to the data in Freychet et al. The direct beam is aimed off the detector so as not to saturate the CCD. As reported in the literature, the presence of oscillations in the Bragg rod are purportedly evidence that 3D chemistry is being probed. Just as in Freychet et al., the strongest oscillations were observed at 285.3 eV. The Bragg peak intensity at this energy vs q_z, corresponding to the thickness of the sample, for each of the three samples is shown in Figure 4.14.

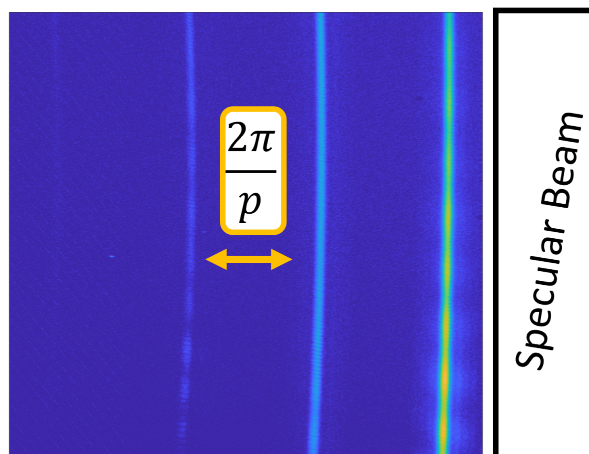

Figure 4.13: Example of experimental grazing incidence CD-RSoXS data, as it appears on the CCD.

However, as shown in Figure 4.15, the experimental data also seemed to show some oscillatory behavior at 250 eV, well below the edge where the resonant effect should be minimal. Additionally, it seemed odd that there would be no Bragg rod oscillations at 285 eV, where the experimentally measured optical constants suggest that the maximum contrast should occur. This highlighted that another factor may be contributing to the scattering signal, namely the shrinkage of the resist discussed in Section 3.2. The realization

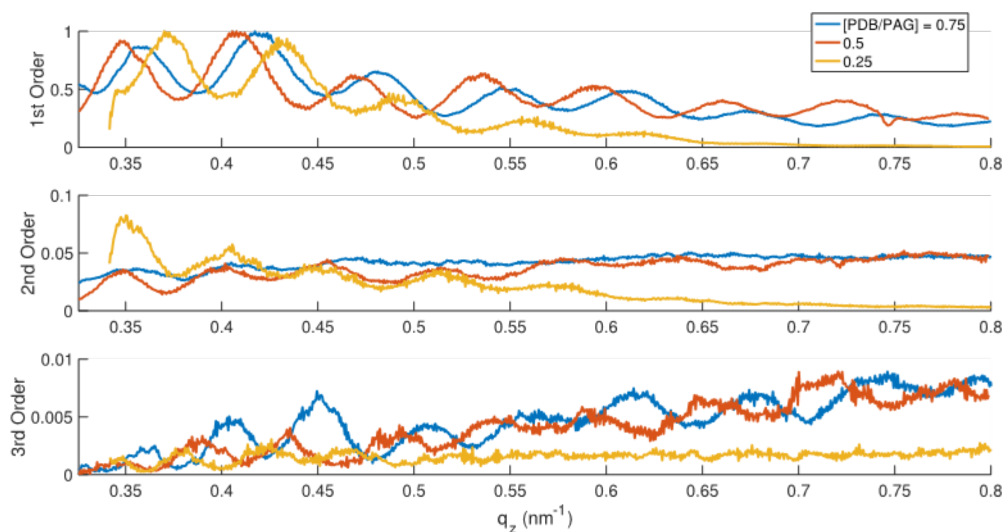

Figure 4.14: Scattered intensity at 283.5 eV vs q_z for the different PDB loadings studied.

that perhaps these subtle effects had yet to be fully understood motivated a detour from the scattering experiments to look at more sophisticated electromagnetic models.

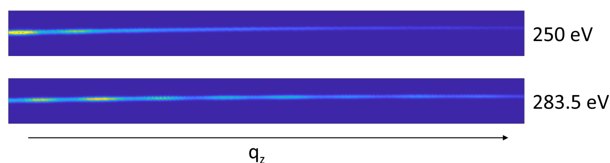

Figure 4.15: Comparison of Brag rod oscillations at 250 eV and 283.5 eV.

4.3.3 RCWA RSoXS Modeling - Reflection

To tease out the role of shrinkage in the scattering process, rigorous coupled wave analysis (RCWA) was used. In Freychet et al., the resist profiles had been fit using the distorted wave Born approximation (DWBA). The DWBA is like the Born approximation, but it takes account of multiple scattering from the silicon substrate, a necessity due to the strong scattering nature of the silicon, particularly at grazing angles. However, it was concluded that the small amount of shrinkage, estimated at a few nanometers, was too small to impact the measured scattering in the q range measured in the experiment, since a small amount of shrinkage should imply Bragg rod oscillations at large q.

As opposed to the DWBA, RCWA simulations yield a full, rigorous solution Maxwell's equations. The implementation used here is from Panoramic Technologies' EM Suite. To look at the impact of chemistry, shrinkage, and its relation to incident beam energy, the

experimental index of refraction in Figures 4.3b and 4.3a was again used. The diffraction from a structure with shrinkage-only, chemistry-only, and both combined were simulated at several relevant energies. Table 4.1 contains the δ and β values used for the RCWA simulations. The thickness of the resist was set to 45 nm, with a shrinkage value set to 4 nm in accordance with values measured for similar resist samples using AFM. The results are shown in Figure 4.16, where blue, red, and yellow traces correspond the 1st, 3rd, and 5th diffraction orders, respectively. The even orders are very nearly extinguished by the 1:1 duty cycle of the pattern. The results clearly indicate that something more complicated is going on in terms of the contrast mechanism for this scattering process.

Energy (eV)	Unexposed δ	Unexposed β	Exposed δ	Exposed β
250.0	$1.969 * 10^{-3}$	$1.439 * 10^{-4}$	$1.954 * 10^{-3}$	$1.439 * 10^{-4}$
283.0	$-4.977 * 10^{-4}$	$3.956 * 10^{-5}$	$-6.084 * 10^{-4}$	$3.587 * 10^{-5}$
285.0	$-1.374 * 10^{-3}$	$3.365 * 10^{-3}$	$-1.414 * 10^{-3}$	$3.700 * 10^{-3}$
287.0	$-1.898 * 10^{-3}$	$1.709 * 10^{-3}$	$-2.031 * 10^{-3}$	$1.743 * 10^{-3}$

Table 4.1: δ and β values for exposed and unexposed photoresist at energies used for rigorous electromagnetic modeling.

First, the shrinkage-only data presented in the first column of Figure 4.16 shows that structures with only topographical differences produce Bragg rod oscillations. These oscillations are most pronounced at energies where the absorption component is low (i.e. below the edge), and are least pronounced right on an absorption resonance peaks (285 and 287 eV). The shape of these curves looks rather like those that the specular beam might undergo as the sample is rotated. Together, this suggests that the diffraction orders themselves show reflectivity curve-like behavior, independent of any 3D chemical profiling. That the Bragg oscillations are minimized at 285 eV, consistent with the results presented by Freychet et al.[10], suggests that the film is simply absorptive enough at that energy that light reflected from the substrate is too strongly attenuated to interfere with light reflected from the top of the structure. Thus, reflectivity oscillations are muted. Also shown in the shrinkage-only scattering simulations is the strong dip just above $q_z = 1.5$ nm^{-1}, characteristic of the 4 nm shrinkage.

Second, looking at the chemistry-only structure (second column of Figure 4.16), the oscillations take on the characteristic sinc function style described earlier in this chapter, with sharp nulls spaced by $\Delta q_z = 1.39$ nm^{-1}, consistent with a 45 nm thick resist. In comparison with the shrinkage-only model, the scattering from the chemistry only model is much weaker, especially at 250 nm. A boost in the intensity of the scattered orders is certainly seen near the edge, though the log scale on the y axis obfuscates that the intensity is at least an order of magnitude weaker at nearly all q_z values.

Finally, putting the chemistry and shrinkage together (third column of Figure 4.16), the overall scattering signal is dominated by the signal coming from the shrinkage, as would be

expected based upon the shrinkage and chemistry-only model results. Nevertheless, the results for the combined model certainly show differences relative to the shrinkage-only model, suggesting that the chemistry does indeed play a role in the scattering signal, especially close to the edge. While not the chemistry-dominated scattering that would be ideal for this technique, the results suggest that a sufficiently sophisticated model might be able to tease out the full 3D chemical-physical structure of the latent photoresist pattern.

4.3.4 RCWA RSoXS Modeling - Transmission

As highlighted in the previous section, reflection from the substrate results in a complicated scattering signal. A transmission geometry should simplify matters. To put this idea to the test, the same RCWA simulation package was used to simulate the same structures as in Section 4.3.3, but in the transmission geometry. The rotation angle ϕ corresponds to that in Figure 4.2a. The results of the simulation are shown in Figure 4.17. Starting with the structure-only column, the shape of the scattering profiles is more or less consistent at all X-ray energies, with a small increase in scattered intensity as the energy approaches the absorption edge. Also present is an asymmetry between the $\pm q_z$ intensities. This asymmetry is not explained by the Born approximation. Moving on to the chemistry-only simulations, scattering intensity is, like in the reflection simulations, lower than the structure-only intensity, especially below the edge. The overall shape of the profiles mimics that of a sinc function as predicted by the Born approximation, with the exception that, like the structure-only simulations, there is an asymmetry about $q_z = 0$. Finally, the combination of chemistry and shrinkage shows that, near the carbon edge, the chemical contribution to the scattering signal is significant enough to modify the scattering profiles. Below the edge, the chemistry and shrinkage signal is dominated by the structural contribution. This suggests a method for separating the two components by taking a measurement well below the edge and one near the edge, and ensuring that the resulting fit works well for both incident energies.

The asymmetry about $q_z = 0$ shows up in all the simulations. The most obvious effect shows up at the negative q_z values, where there is a prominent boost in the scattering signal, especially near the negative extreme of each trace. At this extreme, the diffracted order is nearly parallel with the sample surface; if the angle of the beam is changed much more, the diffracted order becomes evanescent. While the exact origin of this phenomena is unclear, it is perhaps due to a coupling of other evanescent scattered orders (every higher order is evanescent at the same incident angle) when the diffracted order propagates near the surface.

4.3.5 Transmission CD-RSoXS Experiment

Transmission CD-RSoXS was carried out on the same set of materials that were used for the modeling input. Line-space patterns were exposed at a pitch of 100 nm on 1.5 mm × 1.5 mm SiNx windows. A range of doses were exposed across an array of 8 windows. The doses were picked by scaling up a range of doses around the dose that gave 50 nm CD lines on a Si wafer. A scaling is required because there is far less backscatter from a thin SiNx

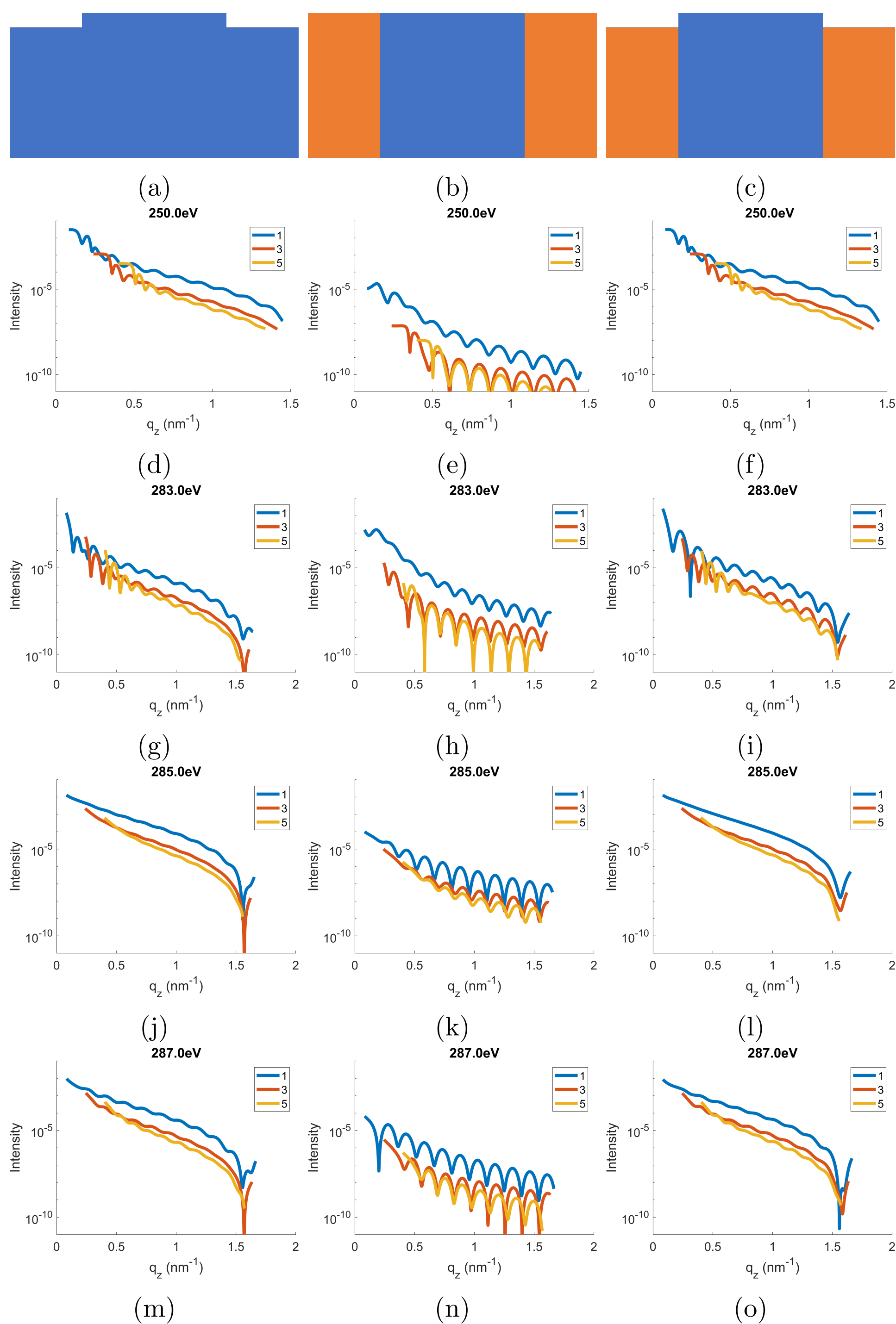

Figure 4.16: RCWA simulations of reflection CD-RSoXS experiment.

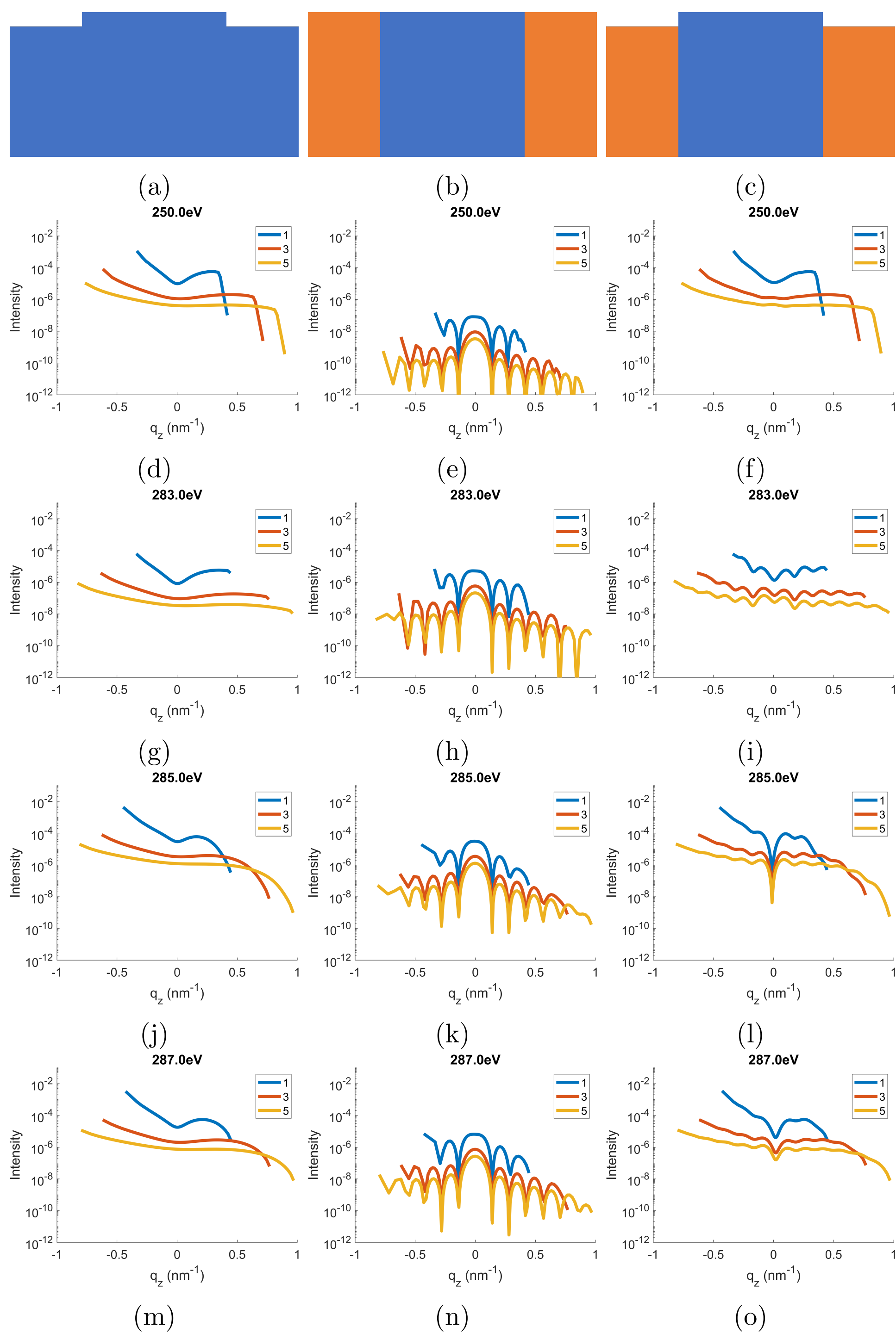

Figure 4.17: RCWA simulations of transmission CD-RSoXS experiment.

membrane than from a silicon wafer. Unfortunately, only 3 of the delicate windows survived exposure and processing. Data from the remaining windows is shown in Figure 4.18.

The results qualitatively show similar trends to those observed in Figure 4.17 - the relative intensities of the orders, the modulated sinc oscillations in the intensity, and the asymmetry in q_z all appear in the experimental data. Furthermore, ripples indicative of thickness appear stronger at resonant energies compared to those below the edge. Unlike the modeling data, which shows orders 1, 3, and 5, as these are the strong orders for the perfectly square structure with defined boundaries that was simulated, the experimental data shows strong second order diffraction (red data points). This suggests that the structure is not a perfect 1:1 square wave, but that there is either some non-vertical profile, the transition from exposed to unexposed material is non-binary, or, most realistically, both. Additionally, it can be seen that the signal from the third diffraction order is relatively noisy. This is due to the dynamic range of the detection, which saturates at around 65,000 counts, and has dark counts in the 100 s, leaving about three orders of magnitude of dynamic range. Future experiments may need to use different CCD positions and integration times to effectively capture higher order diffraction signals. Long integration times must be weighed against the effect of beam damage. The smaller range of q_z measured experimentally as compared to what was modeled is due to the geometry of the SiNx windows. At large angles, the incoming X-ray beam is clipped by the Si frame surrounding the window, causing strong scattering not from the sample but the support that holds it. Thus, the size of the window and the thickness of the window frame limit the angle range that can be measured, and, in turn, the range of q_z.

Unfortunately the patterns were never developed as the remaining windows broke when trying to remove them from the X-ray sample plate. However, that the scattering profiles change as a function of X-ray energy and as a function of exposure dose experimentally shows that CD-RSoXS has the potential to perform latent image profilometry.

4.3.5.1 RSoXS Profilometry Conclusions

The results presented here suggest that RSoXS may indeed be a useful tool for latent image profilometry, though careful modeling is needed for a full interpretation of results. As shown by rigorous electromagnetic modeling both in reflection and transmission, the chemical contribution to scattering near the edge is weak when compared to the topographical change caused by exposure. Nevertheless, it is strong enough to imprint itself on the scattered intensity. In both the grazing incidence and transmission geometry, rigorous modeling reveals the need for sophisticated models to predict measured scattering - the Born approximation appears to be insufficient. In the grazing configuration, this is due to thin film reflections that lead to reflectivity oscillations of the diffraction orders that are distinct from those caused by the 3D PSD of the sample structure. In transmission, rigorous modeling reveals an asymmetry of the diffracted orders that is inconsistent with the Born approximation. In both cases, preliminary experimental evidence shows features consistent with the rigorous modeling. As a scattering model is ultimately used to fit the latent profile, it is critical that it captures the key physical phenomena that appear in experiment in order for proper

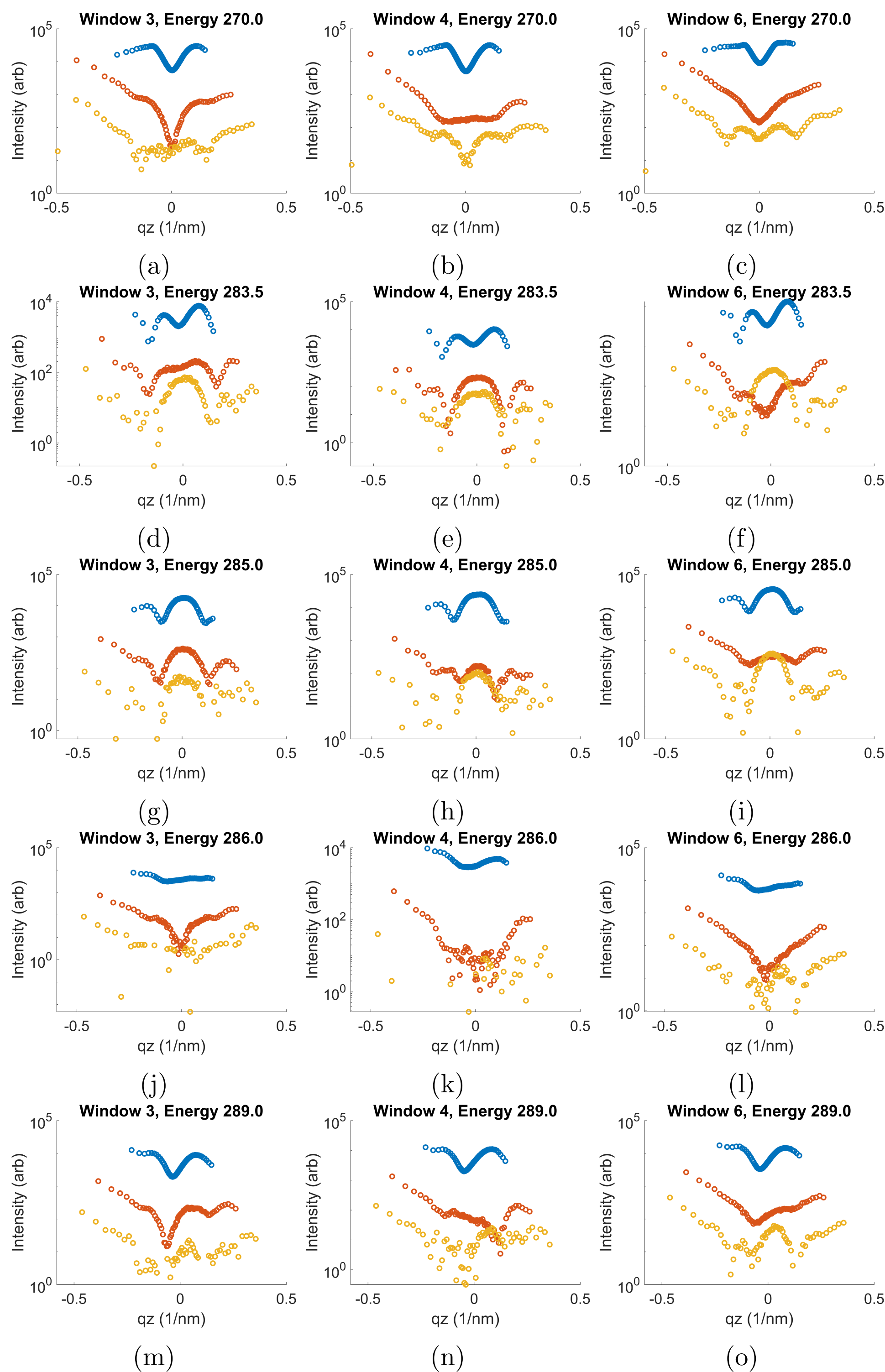

Figure 4.18: Experimental resonant CD-SAXS data, showing the first (blue), second (red), and third (yellow) order scattering intensity vs q_z.

shape extraction. Future efforts will need to dedicate work to deciphering acceptable approximations or optimization and parallelization of the rigorous solver to fit experimental data.

4.4 Beam Damage

A final consideration that needs to be made for any RSoXS experiment is beam damage. Photoresists are radiation sensitive by design, so it only follows that X-ray exposure may itself induce chemistry in the materials. Fortunately, in CAR, the exposure itself does relatively little chemistry without a post exposure bake. Nevertheless, absorption of X-ray photons may itself result in local heating of the sample and/or substrate. For RSoXS to reach its full potential, beam damage needs to be characterized, and where applicable, mitigated.

As an example, the model material shown in Figure 4.5 was studied in a transmission configuration. First, multiple NEXAFS scans were taken consecutively. The results are shown in Figure 4.19. The results clearly indicate a chemical shift as a result of the X-ray beam exposure, as the overall absorption intensity drops with each consecutive scan. Moreover, the shape of the spectrum changes, with the 288.4 eV absorption peak dropping faster than the sharp peak at 285 eV. However, current settings at the beamline dictate that, for these measurements, the shutter is opened at the beginning of the scan and remains open throughout the experiment, including while the beam energy is being changed. This leads to an increase in total photons hitting the sample. Thus, while this measurement shows that the X-ray beam has some impact on the sample, it is perhaps overly pessimistic due to this excess dose.

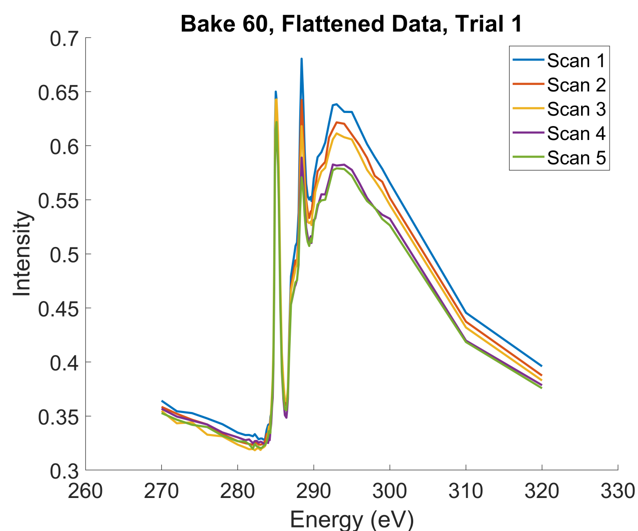

Figure 4.19: Comparison of NEXAFS spectra collected in succession in the same sample location.

A more careful experiment was done by focusing on the peak 288.4 eV. In this experiment, the energy was held fixed at 288.4 eV, and the absorption peak measured every two seconds. The results are shown in Figure 4.20. The results indicate that the material responds to the incident radiation such that the peak decays and eventually saturates to a steady state value, suggesting complete damage to the chemical species being probed. The red line in Figure 4.20 indicates a fit corresponding to an exponential decay of the absorption peak plus an offset. Table 4.2 contains the fit parameters. Of particular interest is the parameter b, which corresponds to the time (and thus X-ray dose) of the $1/e$ decay of the absorption peak. The fit value for b suggests that, when fixed at this energy, the peak decay doesn't hit the $1/e$ point until just over 1000 s of exposure time. The specific threshold for acceptable damage will depend on the application, but given that most CD-SAXS integration times are less than a second, and that the clear field experiments use 30-60 s of integration time, this suggests that beam damage shouldn't be a major inhibitor to the experiment, at least at an incident energy 288.4 eV. Nevertheless, the full NEXAFS damage scans shown in Figure 4.19 highlight that beam damage does need to considered. It is likely that incident energies corresponding to the high-energy, broad peak around 295 eV are more damaging than their lower energy counterparts due to the increased number of accessible transitions and the increased photoelectron energy that results from absorption of these X-rays. Future work must dedicate time to studying the impact of beam damage at any energy used to study latent photoresist chemistry such that the effect of the designed EUV/ electron beam/ DUV exposure can be separated from metrology-induced alteration of the film.

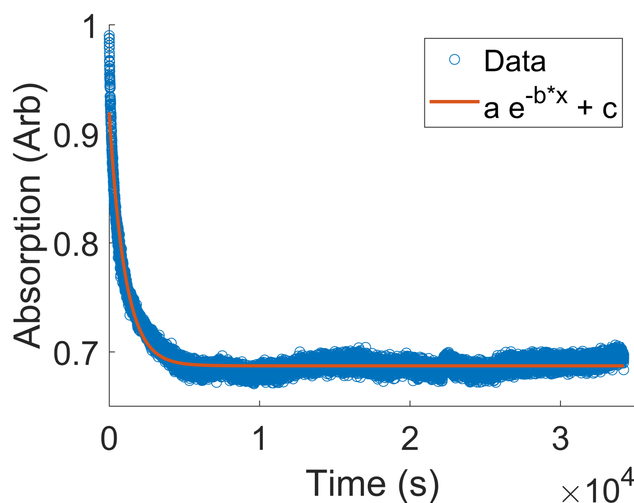

Figure 4.20: Measurement of resist absorption at 288.4 eV as a function of X-ray exposure time.

Parameter	Value
a	0.232
b	$9.58 \times 10^{-4}\,\mathrm{s}^{-1}$
c	0.6872

Table 4.2: Fit parameters for X-ray beam damage study.

Chapter 5

Conclusion

5.1 Summary of Results

In this thesis, a combination of modeling and experimental techniques was used to investigate photoresist materials, and to provide understanding and tools that will be critical to the development of future lithographic materials. The first chapter focused on photoresist modeling. Here, it was shown that a fundamental trade off exists between chemical slope and chemical noise that ultimately determines the roughness of patterned lines in the resist. By using the right chemical additives, namely photodecomposable quencher, one is able to improve the chemical slope produced in CAR materials at the cost of increased noise. Overall, this trade off is favorable, leading to lower LWR when using photodecomposable quencher as opposed the conventional variety. The noise-slope tradeoff underpins next generation photoresist material development, which seeks to lower chemical noise by using single-component resist materials, to improve slope by increasing the dose-response non-linearity of the material, or some combination thereof.

The model was then expanded to include the depth dimension perpendicular to the wafer. The large increase in computation workload was compensated by optimizing and adapting the model to run on GPUs. The resulting simulator was then used to simulate over a million contacts, focusing on the impact of z-dimensional blur on resist performance. The simulations suggest that increasing the z blur of the resist reduced contact failure rate. Furthermore, full 3D simulations highlight the impact of the development and post-processing steps on the ultimate failure rate of the imaging process, suggesting several possible vectors to improve patterning performance in addition to new resist materials.

In addition to the modeling results, several experimental techniques were explored for measuring fundamental resist properties key to both the model and material performance. The first technique explored the use of AFM for latent image metrology. It was found that the exposure-induced shrinkage of the resist can serve as a proxy for the underlying chemical change the exposure induced. In particular, the latent image CD and LWR as measured in the latent, topographical structure was strongly correlated with the CD and LWR of the

fully developed photoresist patterns. Furthermore, the latent image results suggest that the chemical slope in the material improves during the post-exposure bake, highlighting the non-linear transfer from dose to solubility-changed material in the film.

AFM was also used to conduct in-situ measurements of the dissolution process in the resist. By combining a specially designed flow cell with a high-speed AFM, the dissolution process was monitored at a rate of 10 Hz. These results showed that full-strength developer induces a swelling of exposed CAR material prior to its removal, a process known to occur with diluted developer but thought to not be a major factor with 2.38wt% TMAH. The technique now stands ready for use to study the effect of material and process parameters on the dissolution process ultimately responsible for producing the photoresist etch mask.

Finally, RSoXS was explored for the measurement of material homogeneity and for latent image metrology of patterned structures. The material homogeneity studies yielded some promising results for measuring exposure homogeneity in CAR materials, where differences in scattered light distribution were seen between exposed and unexposed materials. This was also true for metal-oxide based materials measured at the tin L edge, where a change in size distribution of the constituent core-ligand structure was seen as a result of exposure.

The results were less clear for metrology of patterned structures, where follow up modeling studies suggest that the contrast mechanism responsible for the measured scattering requires more sophisticated modeling to fully understand. This is especially true for applications in a reflection geometry, where interactions between top-surface and substrate reflections yield data similar to, but ultimately different in physical origin from, the 3D PSD of the scattering structure that the technique seeks to measure. Nevertheless, there does seem to be sensitivity to the underlying latent chemistry in the materials, but careful measurement and analysis will be required to separate the different contrast-inducing structures in the films.

5.2 Future Directions

The results presented in this thesis represent an effort to build tools for understanding photoresist materials. It is my hope that future researchers will continue to build upon and to employ these techniques as new materials are screened for next generation lithographic purposes. These material improvements are necessary to continue the exponential march of semiconductor capability. Such has been recognized by the US Federal Government, as evidenced by passage of the CHIPS Act for bolstering domestic semiconductor manufacturing, and by the recently awarded Department of Energy EFRC, "Center for High Precision Patterning Science," or CHiPPS. The CHiPPS award includes RSoXS as part of its research thrusts, with the work presented in this thesis serving as a baseline for the applicability of the technique. I look forward to seeing the progress made by the future researchers that will carry the torch moving forward.

Bibliography

[1] Mohammed Alvi et al. “Achieving zero EUV patterning defect with dry photoresist system”. In: *Advances in Patterning Materials and Processes XXXIX*. Ed. by Daniel P Sanders and Douglas Guerrero. Vol. PC12055. International Society for Optics and Photonics. SPIE, 2022, PC120550B. DOI: 10.1117/12.2623499. URL: https://doi.org/10.1117/12.2623499.

[2] Ni An et al. “Combined Theoretical and Experimental Study of Refractive Indices of Water - Acetonitrile - Salt Systems”. In: *The Journal of Physical Chemistry B* 119.33 (2015), pp. 10701–10709. DOI: 10.1021/acs.jpcb.5b05433.

[3] Suchit Bhattarai. “Study of Line Edge Roughness and Interactions of Secondary Electrons in Photoresists for EUV Lithography”. PhD thesis. 2017.

[4] Suchit Bhattarai, Andrew R. Neureuther, and Patrick P. Naulleau. “Simulation analysis of LER and dose tradeoffs for EUV resists with photo-decomposable quenchers”. In: *Proceedings of SPIE* 8679.April 2013 (2013), p. 867925. DOI: 10.1117/12.2012669.

[5] John J. Biafore and Mark D. Smith. “Application of stochastic modeling to resist optimization problems”. In: *Advances in Resist Materials and Processing Technology XXIX* 8325.March 2012 (2012), 83250H. DOI: 10.1117/12.916518.

[6] Robert Brainard et al. “Film Quantum Yields of Ultrahigh PAG EUV Photoresists”. In: *Journal of Photopolymer Science and Technology* 21.3 (2008), pp. 457–464. ISSN: 0914-9244. DOI: 10.2494/photopolymer.21.457. URL: http://joi.jlc.jst.go.jp/JST.JSTAGE/photopolymer/21.457?from=CrossRef.

[7] Jingguang G Chen. “NEXAFS investigations of transition metal oxides , nitrides , carbides , sulfides and other interstitial compounds”. In: *Surface Science Reports* 30.1-3 (1997), pp. 1–152.

[8] Mosong Cheng et al. “Improving resist resolution and sensitivity via electric-field enhanced postexposure baking”. In: *Journal of Vacuum Science and Technology B: Microelectronics and Nanometer Structures* 20.2 (2002), p. 734. ISSN: 0734211X. DOI: 10.1116/1.1464835.

[9] Anuja De Silva et al. “Inorganic hardmask development for extreme ultraviolet patterning”. In: *Journal of Micro/Nanolithography, MEMS, and MOEMS* 18.01 (2018), p. 1. ISSN: 1932-5150. DOI: 10.1117/1.jmm.18.1.011004.

[10] Guillaume Freychet et al. “Reconstructing the three-dimensional latent image of extreme ultraviolet resists with resonant soft x-ray scattering”. In: *Journal of Micro/Nanolithography, MEMS, and MOEMS* 18.02 (2019), p. 1. DOI: 10.1117/1.jmm.18.2.024003.

[11] S Funato et al. “Photodecomposable a Novel Chemically Concept To Amplified Bases : Stabilize”. In: *Journal Of Photopolymer Science And Technology* 8.4 (1995).

[12] Gregg M. Gallatin. “Resist blur and line edge roughness”. In: *Proceedings of SPIE* 5754.April (2005), p. 38. ISSN: 0277786X. DOI: Doi10.1117/12.607233. URL: http://proceedings.spiedigitallibrary.org/proceeding.aspx?doi=10.1117/12.607233.

[13] Gregg M. Gallatin, Patrick Naulleau, and Robert Brainard. “Fundamental limits to EUV photoresist”. In: *Advances in Resist Materials and Processing Technology XXIV* 6519.March 2007 (2007), p. 651911. ISSN: 0277786X. DOI: 10.1117/12.712346.

[14] Joseph W. Goodman. *Introduction to Fourier Optics*. 1968.

[15] Steven G. Hansen. “Photoresist and stochastic modeling”. In: *Journal of Micro/Nanolithography, MEMS, and MOEMS* 17.01 (2018), p. 1. ISSN: 1932-5150. DOI: 10.1117/1.JMM.17.1.013506. URL: https://www.spiedigitallibrary.org/journals/journal-of-micro-nanolithography-mems-and-moems/volume-17/issue-01/013506/Photoresist-and-stochastic-modeling/10.1117/1.JMM.17.1.013506.full.

[16] Masahiko Harumoto et al. “Dependence of photoresist dissolution dynamics in alkaline developers on alkyl chain length of tetraalkylammonium hydroxide”. In: *Japanese Journal of Applied Physics* 61.5 (2022). ISSN: 13474065. DOI: 10.35848/1347-4065/ac61f2.

[17] W. D. Hinsberg and S. Meyers. “A numeric model for the imaging mechanism of metal oxide EUV resists”. In: *Advances in Patterning Materials and Processes XXXIV* 10146.March 2017 (2017), p. 1014604. DOI: 10.1117/12.2260265.

[18] William D. Hinsberg and Kay K. Kanazawa. “Quartz crystal microbalance thin-film dissolution rate monitor”. In: *Review of Scientific Instruments* 60.3 (1989), pp. 489–492. ISSN: 00346748. DOI: 10.1063/1.1140405.

[19] Takuma Ishiguro et al. “Resonant soft x-ray reflectivity for the chemical analysis in thickness direction of euv resist”. In: *Journal of Photopolymer Science and Technology* 32.2 (2019), pp. 333–337. ISSN: 13496336. DOI: 10.2494/photopolymer.32.333.

[20] Toshiro Itani and Julius Joseph Santillan. “In situ characterization of photoresist dissolution”. In: *Applied Physics Express* 3.6 (2010), pp. 3–6. ISSN: 18820778. DOI: 10.1143/APEX.3.061601.

[21] Yuko Tsutsui Ito et al. “Swelling and dissolution kinetics of poly (4- hydroxystyrene) in tetrabutylammonium hydroxide (TBAH) aqueous solutions studied by quartz crystal microbalance (QCM) method — in comparison with tetramethylammonium hydroxide (TMAH) aqueous solutions”. In: *Japanese Journal of Applied Physics* 61 (2022).

[22] John David Jackson. *Classical Electrodynamics*. 3rd. John Wiley & Sons, Inc., 1999. ISBN: 978-0-471-30932-1.

[23] Oleg Kostko et al. "Experimental characterization of model resist materials". In: 1185407.October 2021 (2021), p. 13. ISSN: 1996756X. DOI: 10.1117/12.2600890.

[24] Takahiro Kozawa and Seiichi Tagawa. "Radiation Chemistry in Chemically Amplified Resists". In: *Japanese Journal of Applied Physics* 49 (2010). DOI: 10.1143/JJAP.49.030001.

[25] Guillaume Landie et al. "Fundamental investigation of negative tone development (NTD) for the 22nm node (and beyond)". In: *Advances in Resist Materials and Processing Technology XXVIII* 7972.April 2011 (2011), p. 797206. ISSN: 0277786X. DOI: 10.1117/12.882843.

[26] Luke Long, Andrew Neureuther, and Patrick Naulleau. "Measurement and modeling of diffusion characteristics in EUV resist". In: *Proceedings of SPIE* 108090B.October 2018 (2018), p. 10. ISSN: 1996756X. DOI: 10.1117/12.2502226.

[27] Chris A. Mack. "Development of Positive Photoresists". In: *Journal of The Electrochemical Society* 134.1 (1987), pp. 148–152. ISSN: 0013-4651. DOI: 10.1149/1.2100396.

[28] Mark John Maslow et al. "Impact of local variability on defect-aware process windows". In: *Proceedings of SPIE* March 2019 (2019), p. 13. ISSN: 1996756X. DOI: 10.1117/12.2514719.

[29] Timothy B. Michaelson et al. "The Effects of Chemical Gradients and Photoresist Composition on Lithographically Generated Line Edge Roughness". In: *Proceedings of SPIE* 5753.May 2005 (2005), pp. 368–379. ISSN: 16057422. DOI: 10.1117/12.599848. URL: http://proceedings.spiedigitallibrary.org/proceeding.aspx?doi=10.1117/12.599848.

[30] Seiji Nagahara et al. "Photosensitized Chemically Amplified Resist (PSCAR) 2.0 for high-throughput and high-resolution EUV lithography: dual photosensitization of acid generation and quencher decomposition by flood exposure". In: *Proceedings of SPIE* 10146.March 2017 (2017), 101460G. ISSN: 1996756X. DOI: 10.1117/12.2258217. URL: http://proceedings.spiedigitallibrary.org/proceeding.aspx?doi=10.1117/12.2258217.

[31] Patrick Naulleau, Suchit Bhattarai, and Andrew Neureuther. "Understanding extreme stochastic events in euv resists". In: *Journal of Photopolymer Science and Technology* 30.6 (2017), pp. 695–701. ISSN: 13496336. DOI: 10.2494/photopolymer.30.695.

[32] Patrick Naulleau and Gregg Gallatin. "Relative importance of various stochastic terms and EUV patterning". In: *Journal of Micro/Nanolithography, MEMS, and MOEMS* 17.04 (2018), p. 1. ISSN: 1932-5150. DOI: 10.1117/1.JMM.17.4.041015. URL: https://www.spiedigitallibrary.org/journals/journal-of-micro-nanolithography-mems-and-moems/volume-17/issue-04/041015/Relative-importance-of-

various-stochastic-terms-and-EUV-patterning/10.1117/1.JMM.17.4.041015.full.

[33] Patrick Naulleau et al. “Stochastics and EUV Patterning in the 1x-nm Regime”. In: *Journal of Photopolymer Science and Technology* 29.6 (2016), pp. 797–802. ISSN: 13496336. DOI: 10.2494/photopolymer.29.797.

[34] Atsushi Sekiguchi, Hiroko Konishi, and Mariko Isono. “Observation of swelling behavior of ArF resist during development by using QCM method (2)”. In: *Journal of Photopolymer Science and Technology* 25.4 (2012), pp. 467–472. ISSN: 09149244. DOI: 10.2494/photopolymer.25.467.

[35] J. A. Sethian. “A fast marching level set method for monotonically advancing fronts”. In: *Proceedings of the National Academy of Sciences of the United States of America* 93.4 (1996), pp. 1591–1595. ISSN: 00278424. DOI: 10.1073/pnas.93.4.1591.

[36] *SuMMIT LER Analysis, www.lithometrix.com.*

[37] Daniel F Sunday et al. “Determining the shape and periodicity of nanostructures using small-angle X-ray scattering”. In: *Journal of Applied Crystallography* 48.5 (2015), pp. 1355–1363. DOI: 10.1107/s1600576715013369.

[38] Daniel F. Sunday et al. “Determination of the internal morphology of nanostructures patterned by directed self assembly”. In: *ACS Nano* 8.8 (2014), pp. 8426–8437. ISSN: 1936086X. DOI: 10.1021/nn5029289.

[39] TSMC. *TSMC’s N7+ Technology Is First EUV Process Delivering Customer Products to Market in High Volume.* 2019. URL: https://pr.tsmc.com/english/news/2010.

[40] David Van Steenwinckel et al. “Lithographic importance of acid diffusion in chemically amplified resists”. In: *Advances in Resist Technology and Processing XXII* 5753.May 2005 (2005), p. 269. DOI: 10.1117/12.598677.

[41] David Van Steenwinckel et al. “Resist effects at small pitches”. In: *Journal of Vacuum Science & Technology B: Microelectronics and Nanometer Structures* 24.1 (2006), p. 316. ISSN: 10711023. DOI: 10.1116/1.2151912.

[42] Yannick Vesters, Danilo De Simone, and Stefan De Gendt. “Dissolution rate monitor tool to measure EUV photoresist dissolution”. In: *Journal of Photopolymer Science and Technology* 30.6 (2017), pp. 675–681. ISSN: 13496336. DOI: 10.2494/photopolymer.30.675.

[43] G M Wallraff et al. “Experimental method for quantifying acid diffusion in chemically amplified resists”. In: *Proc. of SPIE* 3678.June 1999 (1999), p. 138. DOI: 10.1117/12.350196.

[44] John T. Woodward et al. “Characterization of the latent image to developed image in model EUV photoresists”. In: *Advances in Resist Materials and Processing Technology XXV* 6923.April 2008 (2008), 69232B. ISSN: 0277786X. DOI: 10.1117/12.773036.

[45] Hao Xu et al. “Underlayer designs to enhance the performance of EUV resists”. In: *Advances in Resist Materials and Processing Technology XXVI* 7273.April 2009 (2009), 72731J. ISSN: 0277786X. DOI: 10.1117/12.814223.

[46] Lei Yuan. “Modeling and Calibration of Resist Processes in Photolithography”. PhD thesis. University of California, Berkeley, 2005. ISBN: 0315880678.

[47] Dominik Ziegler et al. “Ideal Scan Path for High-Speed Atomic Force Microscopy”. In: *IEEE/ASME Transactions on Mechatronics* 22.1 (2017), pp. 381–391. ISSN: 10834435. DOI: 10.1109/TMECH.2016.2615327.

[48] M Zuniga, E Tomacruz, and A Neureuther. “Diffusion Effects in Chemically Amplified Deep-UV Resists”. In: *Proceedings of SPIE* 2195.May 1994 (1994), pp. 320–328. ISSN: 1996756X. DOI: 10.1117/12.175349.